

Light Emission from Multi-Electron Processes in the Scanning Tunneling Microscope

Dissertation

zur Erlangung des Doktorgrades
der Mathematisch-Naturwissenschaftlichen Fakultät
der Christian-Albrechts-Universität zu Kiel

vorgelegt von
Peter-Jan Peters

Kiel, 2018

Erster Gutachter: Prof. Dr. Richard Berndt
Zweiter Gutachter: Prof. Dr. Kai Roßnagel

Tag der mündlichen Prüfung: 2. Februar 2018

Erklärung

Hiermit erkläre ich, dass diese Abhandlung - abgesehen von der Beratung durch meinen Betreuer - nach Inhalt und Form meine eigene Arbeit ist. Sie wurde bisher, weder ganz noch zum Teil, an keiner anderen Stelle im Rahmen eines Prüfungsverfahrens vorgelegt, veröffentlicht oder zur Veröffentlichung eingereicht. Diese Arbeit ist unter Einhaltung der Regeln guter wissenschaftlicher Praxis der Deutschen Forschungsgemeinschaft entstanden.

Kurzfassung

Diese Arbeit behandelt Lichtemission von Edelmetallkontakten im Rastertunnelmikroskop (STM). Wesentliche Unterthemen sind die lokale Elektronentemperatur und Lichtemission aufgrund von Mehrelektronenprozessen.

Obwohl Lichtemission aus dem STM bereits seit fast 30 Jahren untersucht wird, wird die quantitative Analyse von STM-Lichtspektren, sowie der Vergleich mit theoretischen Modellen, immer noch durch den starken Einfluss der Plasmon-Moden des Spitze-Probe-Systems erschwert. Diese Moden führen zu ausgeprägten spektralen Strukturen, welche sich von Spitze zu Spitze unterscheiden. Um diese Schwierigkeiten zu überwinden, wurde in dieser Arbeit ein Normierungsverfahren entwickelt, ausgehend vom bereits bekannten theoretischen Modell der Einzelelektronen-Lichtemission im STM, sowie von experimentellen Beobachtungen. Es wurde gezeigt, dass das Verfahren selbstkonsistent ist bezüglich der Annahmen unter denen es abgeleitet wurde.

Die Normierung wurde dann angewendet um Temperaturinformationen aus STM-Lichtspektren zu gewinnen. Eine solche Temperaturmessung ist extrem lokal, da sie die hohe laterale Auflösung des STM teilt. Hervorragende Übereinstimmung zwischen normierten Spektren und Modellvorhersagen zeigen, dass dies ein gutes Temperaturbestimmungsverfahren ist. In Abhängigkeit von Spannung und Strom wurden Temperaturen in der Größenordnung von einigen 10 Kelvin gefunden. Dies steht im Kontrast zu Temperaturen von vielen 1000 Kelvin, welche in anderen Veröffentlichungen, die die STM-Lichtemission als eine Art Schwarzkörperstrahlung eines heißen Elektronengases interpretieren, gefunden wurden. Unter Anwendung des Normierungsverfahrens zur Analyse von Lichtspektren bei hohen Photonenenergien wurde gezeigt, dass STM-Lichtspektren nicht einfach durch thermische Emission eines heißen Elektronengases erklärt werden kann. Zum ersten Mal werden in dieser Arbeit Lichtspektren aus dem Rastertunnelmikroskop bei Photonenenergien von mehr als der zweifachen höchsten Energie von Einzelelektronenprozessen

gezeigt. Dabei werden Messartefakte, die aufgrund der niedrigen Lichtintensität eine wichtige Rolle spielen, identifiziert und, sofern möglich, korrigiert. Es wurden spektral aufgelöste Lichtmessungen, sowie abstandsabhängige Intensitätsmessungen durchgeführt. Die abstandsabhängigen Messungen stellen einen entscheidenden Fortschritt für den aktuellen Wissensstand dar, da sie ein qualitativ unterschiedliches Verhalten bei verschiedenen Photonenenergien aufzeigen. Normierte Lichtspektren bei verschiedenen Spannungen zeigen eine Änderung der Steigung bei bestimmten spannungsabhängigen Energien. Dies tritt reproduzierbar über viele Messungen hinweg auf und zeigt eindeutig, dass in verschiedenen Photonenenergiebereichen verschiedene Prozesse ausschlaggebend sind. Es wurde dann ein quantitatives Modell entwickelt, welches die Lichtemission aufgrund von Mehrelektronenprozessen beschreibt. Es handelt sich dabei um eine halbempirische Verallgemeinerung des Einzelelektronenmodells. Über einen weiten Photonenenergiebereich zeigt das Modell hervorragende Übereinstimmung mit gemessenen Spektren. Es existieren jedoch einige Abweichungen, welche aber als Messartefakte erklärt werden. Die Abhängigkeit der Lichtintensität vom Leitwert des Kontaktes wird im Rahmen von Landauer-Büttiker-Leitungskanälen erklärt. Schließlich wird die Vereinbarkeit des hier entworfenen Modells mit zwei alternativen theoretischen Ansätzen gezeigt.

Abstract

Light emission from noble metal junctions in a scanning tunneling microscope (STM) was investigated. The main subtopics are the determination of the local electronic temperature at the STM junction and light emission from multi-electron processes.

While the light emission from a STM has been studied for almost 30 years now, the quantitative analysis of STM light spectra and comparison to theoretical models was hindered by the strong influence of the plasmon modes of the tip-sample system, which are strongly structured spectrally and vary between different tips. To overcome these difficulties, a normalization scheme was derived in this thesis, based on the established model of single-electron STM light emission and experimental observations. It was shown that the normalization is self-consistent concerning the assumptions used in its derivation.

The normalization was then applied to extract temperature information from STM light spectra. This temperature measurement is extremely local, as it shares the high spatial resolution of the STM in general. Excellent agreement between normalized measured spectra and model predictions suggest that this is a good temperature probe. Temperatures in the order of 10s of Kelvins, depending on the applied bias and current, were found, in contrast to the results of many 1000s of Kelvins found in the literature, which are based on the interpretation of the light emission as the result of black-body emission from a heated electron gas. Using the normalization scheme for the analysis of STM light spectra at elevated photon energies, it was shown that the light intensity at these photon energies cannot simply be attributed to the thermal emission of an electron gas at elevated temperature and is instead to be interpreted as the result of electron-electron interaction. Measurements of light emission from a STM junction at photon energies more than two times the cutoff-energy of single-electron processes are shown for the first time. In these data detection artifacts due to the low intensity in this energy range are identified and,

if possible, corrected. Spectrally resolved light measurements, as well as tip-sample distance dependent intensity measurements, were done. The distance dependent measurements are an important improvement for the current state of knowledge, as they prove a qualitatively different behavior of light emission at different photon energies ranges. The analysis of bias dependent measurements using the new normalization scheme, reveal a change of the slope of the spectra at the distinct bias dependent thresholds, consistently over many measurements. This clearly indicates that a different process dominates in each energy range. A quantitative model for light emission from multi-electron processes is developed. This semi-empirical extension of the one-electron case is in excellent agreement with spectra in most of the measured photon energy range. Nevertheless, some deviations occur which can be attributed to detection artifacts due to the low intensity of the light emission at high photon energy. The conductance dependence of the light intensity in each photon energy range is explained by the model in terms of Landauer-Büttiker conduction channels, in agreement with shot-noise measurements. Finally compatibility of the model with two alternative approaches found in the literature is shown.

If you fall flat on your face, at least you're moving forward.
(Richard Branson)

Contents

Erklärung	i
Kurzfassung	iii
Abstract	v
Contents	ix
1 Introduction	1
2 History	5
2.1 Experiments Related to STM Light Emission	5
2.2 Theory: Tip-Induced Plasmons or Coupled Plasmons	7
2.3 Overbias light emission	8
3 Methods	11
3.1 Overall Setup	11
3.2 STM and Optics	12
3.3 Tip and Sample Preparation	13
3.4 Visible light Spectrometer, CCD	14
A Dark Signal	15
B Cosmic Rays	16
C Residual Images / Ghosting	18
D Energy resolution	19
3.5 Alternative Detectors	20
4 Light: Single Electron Processes	23
4.1 Model	23
4.2 Shape of Spectrum - Plasmon Resonance	26
4.3 Normalization	34

4.4	Conduction Channels, Fano Factor	39
4.5	Effect of finite temperature - Spectral Thermometry	42
4.6	Energy dependent transmission probability	49
5	Light: Multi-Electron Processes	59
5.1	Experimental results	59
5.2	Available theoretical approaches	63
5.3	An empirical model	64
5.4	Discussion	71
6	Conclusion and Outlook	75
A	General Noise Power of Current Fluctuations	77
B	Non-Equilibrium Hot Carriers	79
C	Comparison with Xu et al.	83
D	Energy Dependent Transmission	87
E	Acknowledgements	91
F	Data Used	93
	Bibliography	99

Chapter 1

Introduction

The coupling of light to structures of nanometer scale plays an important role in many fields of recent interest, like efficiency enhancement in light emitting diodes (LEDs) [1–4], improvement in photovoltaic cells [5–9] or sub-wavelength sized lasers [10–13]. The tip-sample junction of a scanning tunneling microscope (STM) in particular is a light emitting nano-structure, which has been proven to be a useful research tool. Light emitted from such a junction offers information that is complimentary to the current and topographic height measurements of the STM itself. Light emission experiments share the exceptionally high spatial resolution of the STM [14], rendering the study of optical properties with sub-wavelength resolution possible. Furthermore, electromagnetic fields in the vicinity of a metallic STM junction are enhanced by localized plasmon modes [15–20], leading to significantly increased light emission. However, these plasmon modes also pose a challenge in the quantitative analysis of light spectra, as they vary profoundly between different tips [21].

STM light emission is closely related to current shot noise [22–24], but differs in important details, most notably the accessible frequency range. While noise measurements usually probe the range of MHz [25–27] or tens of GHz [28], light emission in the visible range corresponds to frequencies of hundreds of THz. At the same time spectral measurements can be highly energy selective, when using appropriate spectrometers and filters. This allows the observation of processes with energies exceeding the energy of individual electrons [29–31]. While it is still highly debated, there is evidence that this so-called overbias light emission is due to electron-electron interaction, offering a unique opportunity to advance the understanding of multi-electron processes in situations of high current density. One of the major challenges with this is the low light in-

tensity resulting from these processes, necessitating careful experimental setup and calibration.

The organization of this thesis is the following: Chapter 2 will provide an overview of the development of the field of research. Some of the most important publications and results in respect to the topic of this thesis will be outlined.

In chapter 3 the experimental setup and the analysis techniques used to acquire the data that are the foundation of this thesis are explained. Beyond the STM apparatus itself and the optical setup, it is detailed how the detection and correction of measurement artifacts in spectral light measurements, which are important for the low intensity measurements covered later, work. The resolution and detection limits of the setup is also discussed.

Chapter 4 is about light emission from single-electron processes. First, a basic model of STM light emission, which is derived from first-order perturbation theory is described. A new normalization procedure is derived based on this model, allowing the quantitative analysis of light spectra. This analysis was hindered before by the strong influence of the plasmon modes of the tip-sample system, which are different for every STM tip. From the normalized spectra it is possible to extract temperature information. This is done for contacts at different tunneling conditions, analyzing the relation between local temperature and dissipated power. Finally, the normalization procedure, being derived under the assumption of an energy independent probability for electrons to undergo inelastic processes, is tested for robustness and the effects of a possible energy dependence of the transmission probability are studied.

Chapter 5 covers light emission from multi-electron processes. For the first time spectrally resolved intensity measurements, as well as conductance dependent measurements of the overall light intensity, at photon energies more than two times the cutoff-energy of single-electron processes, are shown. Based on these observations shortcomings in existing theoretical descriptions of multi-electron light emission are identified. A quantitative model is then developed, which is a semi-empirical extension of the single-electron model.

The appendices contain supplemental material, which is considered helpful to the understanding of the main text.

Some results presented in this thesis, especially those of chapter 5, were already published in a peer-reviewed journal: [32]

Quantum Coherent Multielectron Processes in an Atomic Scale Contact

P.-J. Peters, F. Xu, K. Kaasbjerg, G. Rastelli, W. Belzig, and R. Berndt

Phys. Rev. Lett. 119, 066803

Published 10 August 2017

All experimental work was conducted by the author. The theory presented in chapter 5 was derived in collaboration between the authors of the mentioned article.

Chapter 2

History

This section provides an overview of the most relevant publications in the field of STM light emission. Its main purpose is to outline the development of the field to provide a context for the following sections. Details that are directly related to the results of this work are discussed later on.

2.1 Experiments Related to STM Light Emission

Even before the STM was invented [33, 34], light emission from similar systems was observed. In 1971 Young [35] reported on photon emission in the topografiner, a predecessor of the STM.

In 1976 Lambe and McCarthy [15] observed light emission from biased metal-insulator-metal structures and were the first to describe this as the result of “inelastic tunneling excitation of optically coupled surface plasmon modes present in the tunneling junction”. They described the number of photons emitted with frequency ν within an interval $d\nu$ at low temperatures as $L(\nu) = P(\nu, U)(|U| - h\nu/e)\theta(|U| - h\nu/e)$, where U is the applied bias, h is Planck’s constant, e is the electron charge and “ $P(\nu, U)$ is a slowly varying function of frequency and voltage involving the density of surface modes and the inelastic excitation and radiation probabilities”. $\theta(|U| - h\nu/e)$ is the Heaviside step function. So the number of emitted photons cuts off linearly towards the threshold $h\nu = eU$. No light emission is observed at higher photon energies. As we will see later (section 4), this is already a very good description of light emission due to one-electron processes from a STM junction.

In 1978 Hansma and Broida [36] reported on light emission from metal-

insulator-metal system where one electrode was distinct metal particles instead of a continuous strip, as it was used by Lambe and McCarthy. While they confirmed the general behavior of the linear cutoff for small voltages, they observed a voltage independent maximum for bias values exceeding 2 V. While not understood at that time¹, this was the first description of localized, particle induced plasmons², as they are later described by Rendell et al. [37, 38] and others (see below). Hansma and Broida also noted a different dependency on the emission angle for light polarized in the plane defined by the sample normal and the line joining the junction and the detector, and the light polarized parallel to the sample. The light polarized in the described plane was found to be most intense at an angle near 60° with respect to the sample normal, the light polarized parallel to the surface to have an intensity decreasing monotonically with the angle relative to the sample normal.

In 1988 Gimzewski et al. [39] recorded light from Ir-Ta³ and Ir-Si(111)7x7 STM junctions. They highlight that this kind of measurement, while correlating strongly with conventional inverse photoemission spectroscopy, is strongly localized and allows the identification of surface features with the high lateral resolution of the STM.

Also in 1988 Gimzewski et al. [40] reported on light emission from Ir-Ag STM junctions showing characteristic maxima in the photon spectrum which “are attributed to resonant excitation and radiative decay of localized surface plasmon polariton mode”.

In 1995 Berndt et al. [14] provided experimental proof of atomic resolution in photon emission in a STM. They could clearly identify the (1x2) reconstruction of the Au(110) surface in a photon map and match it to the constant-current topograph recorded simultaneously.

In 2001 Hoffmann et al. [21] experimentally proved the influence of the tip geometry on STM light emission. Exploiting a double tip, i.e. a situation where two micro-tips are present and close enough together to image the same sample area, they could record light from exactly the same sample site with two different tips without any further change to the experimental setup.

¹In the article the authors explicitly state that they don’t understand the behavior.

²In a STM context these are often called tip induced plasmons.

³This notation for describing STM junctions is used throughout the whole thesis: X-Y is a junction with a tip made of material X and a sample made of material Y without further specifying its crystal orientation, usually these are polycrystalline samples. So, Ir-Ta is an Iridium tip in front of a polycrystalline Tantalum sample. X/Z-Y(111) would be an X tip covered with material Z probing the (111) surface of a Y single crystal.

The observed light spectra were found to clearly deviate. Hoffmann et al. also demonstrated that the photon emission may change drastically after tip modifications occurring in tip-surface contacts.

2.2 Theory: Tip-Induced Plasmons or Coupled Plasmons

A plasmon is "the quantum of electron (or hole) density oscillation". It appears in all materials where charge carriers behave like a free electron gas, most notably metals, but also semiconductors or doped semi-metals. The resonance frequency ω_P of these oscillations depends on the electron density and the effective electron mass, typical values for metals being $\hbar\omega_p = 10$ eV. The broken symmetry at the material surface gives rise to plasmons that are bound to the surface [41]. These surface plasmons can be seen as "light waves that are trapped on the surface because of their interaction with the free electrons of the conductor". "The free electrons respond collectively by oscillating in resonance with the light wave" [42]. The electric field of surface plasmons perpendicular to the surface decays exponentially with distance from the surface. The decay length in the dielectric material above the surface is typically of the order of half the wavelength of light involved. The decay length in the metal is between one and two orders of magnitude smaller [42].

As a result of the interaction between the surface charge and the electromagnetic field the momentum of a surface plasmon mode $\hbar k_{SP}$ is greater than that of a free space photon of same wavelength [42]. This momentum mismatch forbids direct coupling between surface plasmon on smooth surfaces and free-space photons. It may, however, be overcome by surface roughness [42] or a prism near the surface [43].

The geometry of a STM junction is more complex than just a single sample surface. It consists of two electrodes separated by a gap only few Ångströms wide. In this geometry the electrons in either electrode couple to each other and form plasmons that are bound to the junction, so called tip-induced plasmons or coupled plasmons. There is in principle a continuous transition of the properties of two independent electrodes very far away from each other to the properties of the two electrode system with the electrodes in close proximity. While the introduction of tip-induced plasmon as modified surface plasmons is not uncommon (e.g. [44]), this picture might be misleading. Especially

with one pointed electrode, as it is the case in a STM junction, the properties of the coupled plasmon differ substantially from the surface plasmons of the uninfluenced flat sample. These properties will be studied in more detail in section 4.

The following is a rough outline of important steps in understanding the properties of tip-induced plasmons in STM junctions.

In 1978 Rendell et al. [37] theoretically analyzed the dipole moment of a spherical metal particle located over a flat metal film. Their key result is the presence of an infinite, discrete set of levels between a lowest energy (defined by the particle-film-distance, the particle curvature, the average plasma frequency of the involved metals, and the dielectric constant of the oxide separating film and particle) and a maximum energy (defined by the average plasma frequency and the oxide's dielectric constant).

In 1981 Rendell and Scalapino [38] presented a refined and extended version of the aforementioned analysis. Concerning spherical particles the main results are reproduced. This is sometimes referred to as the RS-model.

In 1990 Johansson et al. [45] applied the RS-model in an STM context to describe the resonance function of an Ir-Ag junction, while considering the coupling between current and plasmons in a more detailed manner than it was done before. Their results agreed qualitatively with the experimental results of [40].

In 2000 Aizpurua et al. [46] introduced a model considering the tip as hyperboloid instead of a sphere “and a more accurate description of the tunneling current based on an extension of Tersoff and Hamann's theory”. The hyperboloid shape offers an additional degree of freedom and the model explains the independent variation between the position of the spectral maximum and its height when comparing different tips, even at equal bias and tunneling current.

2.3 Overbias light emission

One of the results of Lambe and McCarthy [15] was that the energy of the emitted photon is limited by the energy of the electrons that generate them. The intensity drops linearly towards a threshold $h\nu_{cutoff} = eU$, with the bias U . However, upon close inspection, this rule does not hold.

In 1998 Pechou et al. [29] observed light from Au-Au and PtIr-Au junctions that does not obey the cutoff condition $h\nu_{cutoff} = eU$. As explanation for

this they suggested either locally increased temperature or surface-enhanced Raman scattering. The biggest deviation between detected photon energy and injected electron energy was 123 meV, corresponding to an equivalent temperature of 1430 K.

In 2002 Downes et al. [30] also presented measurements of light emission from W/Au-Au junctions at photon energies exceeding the cutoff condition defined by the bias $h\nu_{cutoff} = eU$. This was interpreted as blackbody emission from the locally heated electron gas near the junction. Temperatures of up to 9000 K were extracted, far above the melting point of gold. This was explained to be possible by the electron temperature rising far above the lattice temperature due to the high current density in the junction.

In 2003 Hoffmann et al. [31] reported on unusual light emission from a quantum well system, Na monolayers on Cu(111). They found light at photon energies significantly exceeding the energy of a tunneling electron. They proposed two possible mechanism for the origin of what they call “forbidden light”, i.e. light with $h\nu > eU$. In one process, called Auger-like, two electrons tunnel more or less simultaneously and exchange energy while they are within the vacuum-barrier region. This way one of the electrons gains energy and is consequentially able to cause the emission of a photon with an energy exceeding the bias-limit. In the other process a tunneling electron leaves behind a hole below the Fermi energy of the emitting electron. The decaying “hot hole” transfers its energy to another electron which may thereby be lifted above the Fermi energy and can subsequently cause a high-energy photon. They also found the intensity of the “forbidden light” to increase approximately as $I^{1.5}$, where I is the tunneling current, with the exponent decreasing at higher currents.

In 2009 Schull et al. [47] reported a similar behavior for light emission from a Au(111) sample. They found that in the tunneling regime the light intensity follows a power law $R \approx I^\beta$, with $\beta \approx 1.1$ (≈ 1.7) for photon energies below (above) the 1e threshold $h\nu = eU$. At high conductance the intensity was deviating from that power law and increasing less with the current.

In 2010 Schneider et al. [48] noticed the similarity of the photon yield, *i.e.* the photon rate per current, to the Fano factor, which is important in the description of shot noise in quantum conductors, over a wide conductance range for photon energies $h\nu < eU$. For higher photon energies, $h\nu > eU$, they found the yield to increase with conductance for small conductances and then drop

again to a local minimum near $G = G_0$, rising again, and so forth. $G_0 = 2e/h$ is the conductance quantum, with the electron charge e and Planck's constant h .

Chapter 3

Methods

The devices and techniques used throughout this work are described in the following.

3.1 Overall Setup

All experiments presented in this thesis were performed with a low temperature STM in ultra-high vacuum (UHV) conditions. The general design of the vacuum chambers and the STM head was done by Jörg Kliewer [49]. The optical setup was initially designed by Germar Hoffmann [50, 51]. I will provide a brief overview of the apparatus, but refer the reader to the respective publications for details.

The UHV chamber has three separate compartments: the STM chamber, the preparation chamber and the load-lock. The STM chamber houses a two-stage bath cryostat, the outer stage is cooled with liquid nitrogen to a temperature of 77.4 K, the inner stage is cooled with liquid helium. The STM head is mounted to the bottom of the helium tank. It is surrounded by radiation shields, that may be opened to access the STM, closed to minimize the radiative energy influx, or partially opened to allow the introduction of the lens assembly. With the shields in its optimal closed position the temperature of the STM is 5.2 K, with the lens assembly introduced to the inner stage the temperature is 5.7 - 6.0 K, depending on the exact alignment of the lens assembly, which in turn depends on the length of the STM tip.

The preparation chamber contains the station for tip and sample preparation. Electron beam heating and Ar ion bombardment (“sputtering”) can be performed here. It also contains a storage facility for samples and tips. The

preparation chamber is separated by a gate valve from the other chambers. These are only opened for tip and sample transfer and allow to keep a very good vacuum in the STM chamber during sample preparation. A transfer rod allows sample transfer in vacuum between the preparation chamber and STM chamber when the gate valve is open.

The load-lock is just a small chamber that, being separated from the preparation chamber by a gate valve, can be vented and evacuated separately, which is used to introduce new samples or tips. A second transfer rod allows the sample transfer from load-lock to preparation chamber.

3.2 STM and Optics

Scanning tunneling microscopy has become a well established technique and will not be explained in great detail here. For an introduction to this topic, the reader is referred to the many available textbooks, e.g. [52, 53].

The STM head of this machine consists of a stationary part, including the piezo scanner for the tip, and the so-called slider, a metal block that receives the sample and that rests on three additional piezo-mechanic actuators. Tip and sample can be exchanged independently without braking the vacuum using a dedicated tool mounted to a wobble stick. For sample handling the slider can be locked in place in a position several millimeters away from the tip. With the sample mounted to it, the slider is moved forward with the three piezo actuators, until it is within the reach of the STM tip. A exhaustive description of the design, along with detailed schematics and photographs can be found in Kliewer's thesis [49].

The optical setup can be divided in two parts. One part is permanently mounted to the STM chamber. This part consists of the in-vacuo lens, which is introduced into the inner cryostat stage, a steel tube holding the lens, a linear motion feedthrough to move the lens tube into and out of the helium stage, and a UHV viewport (a "window"). To reduce the thermal load on the helium stage while the lens is inserted to it, the tube holding the lens is connected to the nitrogen stage of the cryostat by a flexible copper braid. The other part of the optical setup is outside the vacuum chamber and can thus be modified more easily. The basic setup consist of a second lens just in front of the UHV viewport that focuses the light onto an optical fiber. The fiber is connected to an optical spectrometer or a photomultiplier tube (PMT) detector. Using

a long enough fiber the spectrometer may be in a separate room to reduce the influence of the noise of shutters or cooling fans of the detector on the STM itself.

To align lens and STM tip apex, the optical fiber may be exchanged with an eyepiece. With the radiation shields open to illuminate the STM, the position of the lens can be adjusted by a tilting mechanism until the tip apex is in the middle of the field of view. The distance between the lens and the junction is then adjusted with the linear feedthrough until the image of the tip apex is sharp, indicating that it is in the focal plane of the in-vacuo lens. When studying systems that emit light in the visible energy range, as it is the case throughout this work, the light emitted from the junction itself can be used to reach even better distance adjustment. With the radiation shields partially open (allowing the lens assembly to protrude into the inner stage but all other openings closed) and the STM in tunneling mode, the distance is adjusted until the image of the light is reduced to a narrow spot. The diameter of the spot against the completely dark background is far easier to judge than the sharpness of the image of the tip apex. The position of the spot may also be cross-checked in this situation and if necessary corrected. This way a reproducible adjustment of the optical setup and optimal light collection can be achieved.

3.3 Tip and Sample Preparation

In all experiments covered in this thesis single crystal samples were used. These were prepared by repeated cycles of Ar ion bombardment (“sputtering”) at room temperature and electron beam heating (“annealing”) in UHV conditions.

The STM tips were prepared by electrochemical etching outside the vacuum. The tips were then introduced to the preparation chamber and heated by electron beam to remove any volatile adsorbents. Tungsten tips were brought to a bright yellow glow, noble metal tips were heated only slightly to avoid melting the tip apex. After letting the tips cool down briefly they were transferred into the STM. To obtain a tip apex that is sufficiently stable to conduct experiments over extended periods of time (up to hours in some occasions) with very high currents (up to 100 μA) the tips were treated additionally in the STM. The basic procedure involved forming contacts of around $1 G_0$ conductance at a bias of 1 V, until a smooth and repeatable contact formation

was observed. The contact formation is indicated by a change of slope in the $I(z)$ -curve, i.e. the current I as a function of the distance the tip was moved forward z . If this change of slope occurred at conductances of $1 G_0$, this was interpreted as a single atom being at the very apex of the tip. Sometimes the tip was still unstable after several thousand contact formations or the change of the slope in the $I(z)$ -curve was not near a conductance of $1 G_0$. In this cases a procedure similar to that described by Castellanos-Gomez et al. [54] was applied, where again many thousand contacts were formed, starting with a $20 G_0$ contact, and the distance the tip was brought forward gradually reduced until only a $1 G_0$ contact was formed. During this procedure the bias usually was 0.5 eV in the beginning and 1.0 eV in the end, increasing the bias in arbitrary increments at arbitrary times. Finally the tip stability was checked again on a flat sample area and, if necessary, the process repeated until a stable, mono-atomic tip apex was obtained.

3.4 Visible light Spectrometer, CCD

Most spectrally resolved light measurements presented in this work were conducted with an 'ANDOR DU420A-BU' CCD detector in combination with an 'ANDOR SR-303i-A' Czerny-Turner type grating spectrometer. The spectrometer has a mechanical shutter behind the input and an adjustable width input slit. The grating can be turned to adjust the detection range. The width of the detection range for a single grating position is roughly 570 nm. A wavelength calibration against the spectrum of a Hg lamp was done after setting up the detector and repeated every time the spectrometer setup was moved or modified. Calibrating the wavelength dependent detection efficiency of the overall setup (including the permanently mounted parts) is difficult. For this it would be necessary to have a light source with a well known spectrum at the location of the STM. However, with the normalization method explained in section 4.3, it is not necessary to know the sensitivity of the detector, as it is removed by the normalization.

The low intensity of the light emission studied in this work has implications on how the measurements are conducted as well as on the data analysis. In the following I will describe the relevant detection artifacts and how they were handled in this work.

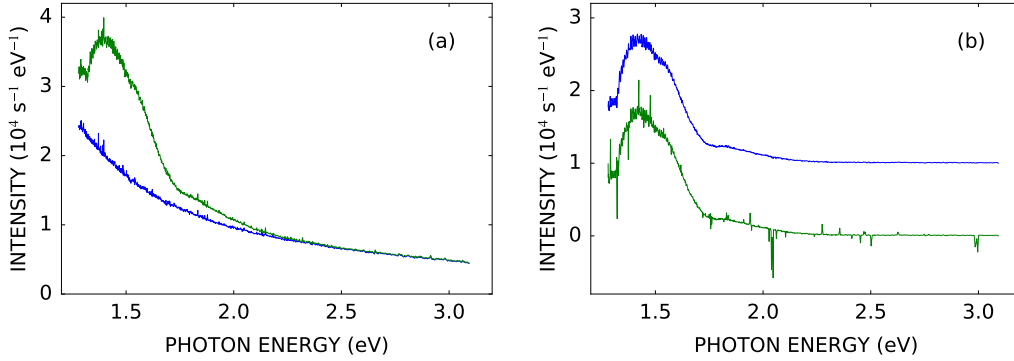


Figure 3.1: (a) Light spectrum recorded from a Ag-Ag(111) junction as green curve, tunneling parameters: $I=30 \mu\text{A}$, $U=0.9 \text{ V}$, along with a spectrum recorded just before with the mechanical shutter of the spectrometer closed (“dark spectrum”) as blue curve. The increase of the dark spectrum towards small photon energies is partially an artifact of the presentation as intensity vs. photon energy. The dark signal varies from pixel to pixel nevertheless. The shown data are an average over 14 frames, each integrating 60s, and 9 frames for the dark spectrum. The algorithm for removal of cosmic rays was applied in both cases (see text for details), the spiky features are hot pixels. (b) A demonstration of the cosmic ray removal procedure, using the same data as in (a). Both curves are the difference between illuminated spectrum and dark spectrum. The lower curve is the result of simply averaging all illuminated frames and all dark frames, respectively, and taking the difference. The upper curve is the result of averaging with removal of cosmic rays and taking the difference. Except for where cosmic rays occur the two curves would exactly overlap, so the corrected curve was shifted upwards for clarity. The apparently increased noise at low photon energies is the result of varying detection sensitivity of neighboring pixels and is correctly not removed by the algorithm.

A Dark Signal

Even when not exposed to any light, the detector will register a non-zero signal, the so called dark signal. The dark signal has two components, a time-independent and a time-dependent one. The time-independent dark signal is a consequence of imperfect read-out electronics of the detector. The time-dependent component is driven by thermal excitations of the detector and thus highly temperature dependent. It can be reduced by cooling the detector.

When measuring low intensity light spectra, it is necessary to subtract the dark signal. This is illustrated in Fig. 3.1a, which shows a low intensity spectrum (with the dark signal still included) and the corresponding dark spectrum. The dark signal is more than half of the recorded intensity at all

photon energies, at high energies it even constituting all the signal. It can also be seen in Fig. 3.1 that the dark signal is varying from pixel to pixel. Some pixels, so called hot pixels, exhibit a significantly higher dark signal than their neighbors. Beyond this the dark signal is also varying slowly over the detector area, being lowest near the middle of the detector and increasing towards the sides. This effect is not recognizable in Fig. 3.1a, due to the presentation of the data vs. a photon energy axis ($h\nu = hc/\lambda$) and the subsequent $1/\lambda$ scaling.

Instead of using one long exposure, the measurements are divided into several shorter ones (called frames), for reasons explained below. All light spectra shown in this work are corrected for the dark signal, by subtracting a dark spectrum of equal single frame integration time recorded before or after the spectrum itself. Spectrum and corresponding dark spectrum are not necessarily the result of averaging over the same number of frames.

An alternative method to this is a model based approach, where the integration time of the spectrum and the dark measurements can be different. In a first step the time-dependent component and the time-independent component of the dark signal are determined from two or more measurements with different integration time. The real measurements are then corrected for a scaled dark signal based on those parameters. This is never done in this work, especially to take care of the changing dark signal due to residual images (see below). Single frame integration times of measurement and dark measurement were always identical in all presented spectra.

B Cosmic Rays

A common type of artifacts found in long-exposure light spectra are saturated single pixels or small groups of pixels in random locations. They are the result of cosmic radiation, especially muons generated in the upper atmosphere, and radioactive decay of impurities in the housing of the detector and the spectrometer, as well as in the glass window of the detector. These high energy particles may hit the detector and generate enough charge to saturate a detector pixel [55]. Even though these artifacts are not entirely caused by cosmic radiation, I will refer to them summarily as cosmic rays. In situations where the integration time is short (on the order of seconds or maybe tens of seconds) the number of cosmic rays is usually small enough to ignore it or even zero. In situations where a long integration time is necessary to have an acceptable signal-to-noise ratio, the number of these events can have significant impact on

the spectrum. This can be seen in Fig. 3.1b, where a low intensity spectrum from a Ag-Ag(111) contact is shown, one time with cosmic ray rejection (the algorithm will be explained shortly) and one time without. The curve using cosmic ray rejection is shifted upwards for clarity. The lower curve exhibits many spiky features, which are said cosmic rays. The ones going up are in the illuminated spectrum, the ones going down are in the dark spectrum.

There are two general strategies to detect cosmic rays in light spectra. The first one relies on the fact that they are very sharp features, so their apparent intensity is much higher than in neighboring pixels. In the present case this is limited by the use of vertical binning. Binning is a common technique in CCD detector operation, where the charge of several pixels is combined (“binned”, hence the name) on the detector chip before reading it. This reduces the number of analog-to-digital conversions necessary to read out the whole chip. The number of pixels combined into one super-pixel is called binning factor. In this work full vertical binning is used, i.e. combining all pixels of a column, effectively turning the two-dimensional detector into a one-dimensional one. Since the detector and the spectrometer are aligned in a way that all pixels of a column are illuminated with light of the same wavelength range, no information is lost by this procedure. The contrast between a (binned) pixel containing a cosmic ray and its neighbor is reduced by the binning factor, as usually only one of the pixels of the column is saturated. Also hot pixels in dark spectra look very similar to cosmic rays. Detecting cosmic rays by their contrast with neighboring pixels is therefore not used in this work.

The second strategy, which is applied in this work, relies on the fact that cosmic rays are rare events in random locations. If a long exposition is divided into several shorter ones, one can check for each pixel if the intensity varies significantly between consecutive read-outs. Since the arrival and detection of photons is itself a random process, the intensity variation has to be considered in terms of the expected standard deviation of the process. Under the assumption that the photon detection is a Poisson process the expected standard deviation σ_N of the number of detected photons N is the square root of the number of detected photons, $\sigma_N = \sqrt{N}$. If the number of detected photons was more than $5\sigma_N$ higher in a single read-out than the average of all read-outs of that pixel, that read-out would be considered the result of a cosmic ray and rejected in a second, final averaging of all read-outs. This way there is still useful information for that pixel, since only a fraction of the integration time

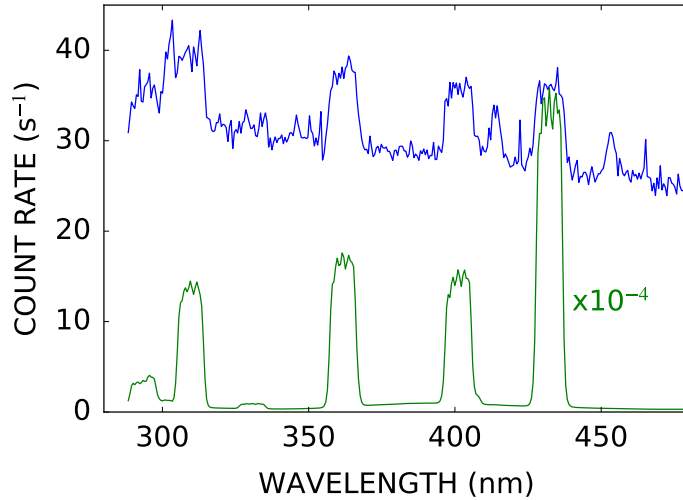


Figure 3.2: Two spectra recorded after each other. The green curve has been recorded first and is a spectrum of a Hg lamp. The spectral lines are clearly visible. To fit the scale with the other spectrum, the data were multiplied with a factor of 10^{-4} . The blue curve is a dark spectrum (recorded with closed shutter) right after the other spectrum. The dark signal is significantly increased in pixels that were exposed to light in the first measurement. Exposition times were 10×0.1 s for the illuminated spectrum and 5×60 s for the dark spectrum.

is contaminated by the cosmic ray and not all. The probability for a deviation by $5\sigma_N$ or more just by chance (without cosmic rays) is $5,7 \cdot 10^{-7}$.

C Residual Images / Ghosting

Photoelectrons generated during the illumination of the detector may be trapped at impurity sites in the detector material. These trapped charges are then released slowly by thermal excitation and add to the signal of subsequent measurements. They appear as residual images or “ghosts” of former images, hence the common name “ghosting” for this phenomenon. The intensity of the residual image decreases with time. The initial intensity and the decay rate depend on the detector temperature. A detailed description of the process can be found in Ref. [56].

Figure 3.2 shows an example of ghosting. The upper, blue line is a dark spectrum recorded just after the spectrum shown as the lower, green line has been recorded, which is the spectrum of a Hg lamp. Pixels illuminated with higher light intensity in the Hg spectrum have a higher dark signal than those illuminated less intensely. In the present case the dark signal is increased by

approximately $5 \cdot 10^{-5}$ times the intensity of the recorded spectrum. However, for the line at 435 nm the relative increase in the dark signal is lower. This might indicate saturation of the available trapping sites. At a detector temperature of -35°C , commonly used throughout this work, the dark spectrum did not change significantly after waiting 10 minutes. However, it should decay over time. Warming up the detector to 20°C for 45 minutes removed the effect completely. It was not tested if this is the shortest time necessary, which it is probably not.

Completely saturating all trapping sites on the detector before every measurement is a common mitigation strategy for this kind of problem [56]. While some devices incorporate an internal lamp to expose the detector to a well defined light intensity, this is not the case with the detectors used in this work and the method can therefore not be applied.

To make sure low intensity measurements are not contaminated by a change in the dark signal as it was just described, there are two alternative strategies. The first one is to simply record an individual dark spectrum before every measurement. For shorter measurements one could also record two dark spectra, one before and one after the measurement, and quantify any changes in the dark spectrum. The second strategy is to warm up the detector to remove any trapped charge, cool it down again and record spectra in the order of the expected intensity, starting with a dark spectrum and the lowest intensity spectra. This takes a longer preparation time than the first method, but it allows for a more compact overall measurement series and thus reduces the risk of any tip changes happening in the STM during the measurement series. The first method was applied in most measurements presented in this work. For the 3e-light spectra presented in section 5, where the integration time of three consecutive spectra summed up to one hour, the second method was applied.

D Energy resolution

In all spectral measurements shown in this work a wide entrance slit was used due to the low light intensities. As a consequence of this the resolution of the spectrometer setup is limited by the width of the entrance slit. This can be seen in Fig. 3.3a, which shows two spectral lines of a Hg lamp, recorded under otherwise equal conditions with different widths of the spectrometer entrance slit. For a slit wider than $100 \mu\text{m}$ but less than $1000 \mu\text{m}$ the line width increases with the slit width. Since the core of the optical fiber has a width of

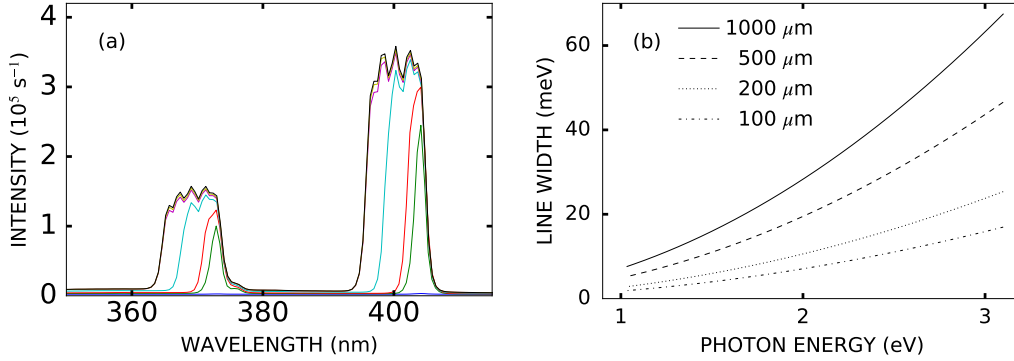


Figure 3.3: (a) Two spectral lines of a Hg-lamp for different slit widths (20, 100, 200, 500, 1000, 1500, 2000 μm). Opening the slit beyond 1000 μm has almost no effect, because in those cases the 1000 μm wide fiber core acts as the effective aperture. The spectral line width (as full-width at half-maximum, FWHM) is: 2.2 nm (slit width 20 μm and 100 μm); 3.3 (200 μm); 6.1 nm (500 μm); 8.9 nm (slit widths > 1000 μm). These values are accurate within 0.1 nm throughout the detectable range.

(b) Energy resolution (FWHM) for different slit widths.

1000 μm , opening the slit wider than that has no effect on the line width, as in those situations the optical fiber itself acts as the effective entrance aperture. Due to the design of the detector the spectral line width is identical within 0.1 nm throughout the detectable wavelength range. If spectra are shown on a photon energy axis, as it is done throughout this work, the line width is energy dependent. Figure 3.3b shows the spectral line width vs. the photon energy for different slit widths, based on the spectral line widths of Fig. 3.3a.

3.5 Alternative Detectors

Infrared spectrometer, InGaAs photodiode array To record light spectra at lower photon energies, an InGaAs photodiode array detector, HORIBA model SII-3LS-512-50-17 [57], in combination with an iHR320 grating spectrometer [58] was used. The specified sensitivity range of the detector is 800-1700 nm (0.73-1.55 eV) at room temperature and 800-1600 nm (0.77-1.55 eV) when cooled to -103°C . The detector itself is cooled with liquid nitrogen. The desired detector temperature is reached by electrically heating it.

The mechanical shutter of the spectrometer is loud enough to make the tip crash into the sample by acoustically exciting the cryostat. Also the integrated fans cooling the auxiliary electronics of the detector are loud enough to cause

significant vibrations of the STM. For these reasons the detector cannot be set up close to the STM, but was placed in the adjacent room, using a 10 m long optical fiber (LASER COMPONENTS JTFIH940100010351400). The absorption of the fiber is less than 5% for wavelengths between 500 and 2000 nm, and less than 2% between 700 and 1900 nm. [59]

Photomultiplier Tube (PMT) The spectrometer/detector setup could also be replaced by a photomultiplier Tube (PMT) to reduce the required integration time. A HAMAMATSU model 'H7422P-50 SEL' was used. To focus the light from the optical fiber onto the detection area, a fused silica lens was mounted in a THORLABS lens tube in front of the detector. This also allowed for optical filters to be mounted in front of the detector to limit the detection range.

Chapter 4

Light: Single Electron Processes

Photon emission from the STM is driven by inelastic transitions of electrons in the junction that couple to plasmons which finally decay into free-space photons. The overall most likely mechanism is the emission of one photon resulting from the inelastic transition of one electron. These one-electron (1e) processes are covered in this section.

4.1 Model

Assuming that all plasmons eventually decay into free-space photons, the photon emission rate¹ can be derived theoretically from perturbation theory, applying Fermi's golden rule [22, 60, 61], to be

$$R(h\nu) = \frac{2\pi}{\hbar} \sum_{i,f} \iint |\langle \psi_f | V | \psi_i \rangle|^2 \delta(\varepsilon_i - \varepsilon_f - h\nu) f_i(\varepsilon_i) [1 - f_f(\varepsilon_f)] d\varepsilon_i d\varepsilon_f \quad (4.1)$$

The sum runs over initial and final states from a complete set of single electron states of the unperturbed system. ψ_i (ψ_f) is the wave function of the initial (final) state. V is the Hamiltonian describing the coupling between electrons and plasmons (the perturbation). δ is the Dirac delta function. f_i (f_f) is the occupation number of the initial (final) state; a Fermi–Dirac distribution when considering systems that are in local equilibrium.

¹It is also common to express the power of the emitted light. In this work the photon rate is chosen instead, since this relates more closely to the quantity measured by the detectors used and, in the end, carries the same information.

This expression can be interpreted in the following way: the transition matrix element $|M_{fi}|^2 = |\langle\psi_f|V|\psi_i\rangle|^2$ means that we consider transitions between states of the system, that are induced by the coupling of the electrons to the plasmons. For the transition to take place, the initial state must be occupied ($f_i(\varepsilon_i)$) and the final state must be empty ($1-f_f(\varepsilon_f)$). The integration over initial energy ε_i and final energy ε_f with the Dirac delta function ensures that we only consider transitions between states with an energy difference matching the photon energy.

To derive the photon emission rate of any system from Eq. 4.1, one must know the eigenstates of the unperturbed system and the Hamiltonian describing the coupling. If we know enough about the configuration of the atoms near the junction this can be done², however, in the case of an STM junction the exact configuration of the tip atoms is usually not known to the degree necessary to quantitatively predict the spectrum. As is discussed later on, major features of the spectrum can be derived theoretically using certain assumptions about the symmetry of the tip. Nevertheless, this does not allow a detailed quantitative prediction of the photon spectrum. In this work a different approach is therefore applied. The first step is to simplify Eq. 4.1 by disentangling the different factors influencing $|M_{fi}|^2$. This is strongly driven by experimental observations, some of which were already mentioned in section 2.

Similar to the case of elastic tunneling, the inelastic processes studied here involve electrons tunneling from one electrode to the other.³ It may therefore be expected that these two processes share the exponential dependence on the distance between tip and sample. Indeed, there is experimental evidence that for large tip-sample distances the overall light emission is proportional to the current and thus the elastic tunneling probability T . However, at high current the factor $T(1 - T)$ describes the behavior much better [48]. The interpretation of this behavior will be discussed later (section 4.4). Based on these experimental observations I will use $|M_{fi}|^2 = Pl(\varepsilon_i - \varepsilon_f)T(\varepsilon_i, \varepsilon_f)[1 - T(\varepsilon_i, \varepsilon_f)]$. Pl is the relative strength of the plasmon modes, it only depends on the energy the electrons lose. T is the relative transition probability resulting from the tip-sample distance and the work functions of tip and sample. The

²For an introduction to the methods used to do this see *e.g.* [62, Chapter 8.4] and references therein.

³For a finite temperature transitions between states within one electrode are also possible. However, as we will see later (section 4.5), the contribution of inelastic transitions within a single electrode are expected to only contribute negligibly to the detected light intensity under the conditions used in the experiments covered in this work.

photon emission rate thus becomes

$$\begin{aligned}
R(h\nu) &= \frac{2\pi}{\hbar} \sum_{i,f} \iint |M_{fi}|^2 \delta(\varepsilon_i - \varepsilon_f - h\nu) f_i(\varepsilon_i) [1 - f_f(\varepsilon_f)] d\varepsilon_i d\varepsilon_f \quad (4.2) \\
&= \frac{2\pi}{\hbar} \iint Pl(\varepsilon_i - \varepsilon_f) T(\varepsilon_i, \varepsilon_f) [1 - T(\varepsilon_i, \varepsilon_f)] \rho_i(\varepsilon_i) \rho_f(\varepsilon_f) \\
&\quad \times \delta(\varepsilon_i - \varepsilon_f - h\nu) f_i(\varepsilon_i) [1 - f_f(\varepsilon_f)] d\varepsilon_i d\varepsilon_f. \quad (4.3)
\end{aligned}$$

Here also the sum over the initial and final states was replaced by the density of states ρ_i (ρ_f) in the initial (final) electrode. Using $h\nu = \varepsilon_i - \varepsilon_f$ this can be rewritten to

$$\begin{aligned}
R(h\nu) &= \frac{2\pi}{\hbar} Pl(h\nu) \int T(\varepsilon, h\nu) [1 - T(\varepsilon, h\nu)] \rho_i(\varepsilon) f_i(\varepsilon) \\
&\quad \times \rho_f(\varepsilon - h\nu) [1 - f_f(\varepsilon - h\nu)] d\varepsilon. \quad (4.4)
\end{aligned}$$

Based on this equation the individual factors influencing the light emission can now be studied separately: The role of the plasmon resonance function will be covered in the next section. The influence of the energy dependence of the transition probability T on the light emission is analyzed in section 4.6. The influence of a density of electron states varying strongly with energy is studied in Refs. [63, 64]. The effect of a spatially varying density of states due to a confined surface state in small islands on the light spectrum was also demonstrated [65]. In this work the density of states in both electrodes is considered to vary only weakly with the energy, since all experiments were conducted on atomically flat noble metal (111) terraces without any step-edges or other features nearby.

The structure of Eq. 4.4, with the plasmon function Pl separated from the integral containing only quantities concerning electron transitions, is tempting to be interpreted as two separate effects: a “current” of inelastically tunneling electrons described by the integral, and an amplification by the plasmon resonance described by Pl . However, even though Pl contains all information about the plasmons and is written outside the integral, this only highlights its independence from the initial electron energy ε . The presence of the plasmons increases the number of inelastically tunneling electrons. This is formally man-

ifested in the fact that Pl is actually part of the transition matrix element M_{fi} . The rate of inelastically tunneling electrons and emitted photons is strictly the same in this model. This is also necessary for conservation of energy, as the influx of electrons is the only source of energy for the process. With this caveat in mind, I will still refer to the integral in Eq. 4.4 as the excitation function. It might be interpreted as a relative measure of how strongly the plasmons are excited at each energy.

As a result of first order perturbation theory, Eq. 4.1 is itself an approximation. It covers only those transitions where exactly one electron loses energy and exactly one photon is emitted. Because of this, I will refer to it as the one-electron model (or just 1e-model). The more general cases of two- and three-electron transitions are covered in section 5.

4.2 Shape of Spectrum - Plasmon Resonance

Observed light spectra - silver

According to Eq. 4.4 it is possible to study the properties of the plasmons separately, when the rest of the expression is kept approximately constant. One way to do this is to compare spectra that were recorded with different tips, but at the same tunneling parameters on an atomically flat region of the sample. The tip preparation described in section 3.3 ensures that tips have a very similar $I(z)$ behavior and can thus be expected to also have a similar density of states ρ . This way the tunneling probability T , as well as the electron densities of states ρ_i and ρ_f , are approximately the same every time. In this situation differences in spectra recorded with different tips stem from different plasmon functions Pl .

The plasmon function depends on the type of material in either electrode, as well as their precise shape. In this section spectra recorded with a Ag tip on a Ag(111) sample will be shown. Ag was chosen because of its small imaginary part of the dielectric function and thus low internal damping. This leads to a high photon yield.[66] Also the maximum of emission is in the visible energy range for most tip shapes, allowing efficient detection.

Fig. 4.1 gives an example of Ag-Ag(111) light spectra. The four spectra shown were all recorded with bias $U=3V$ and current $I=5\mu A$, but each one

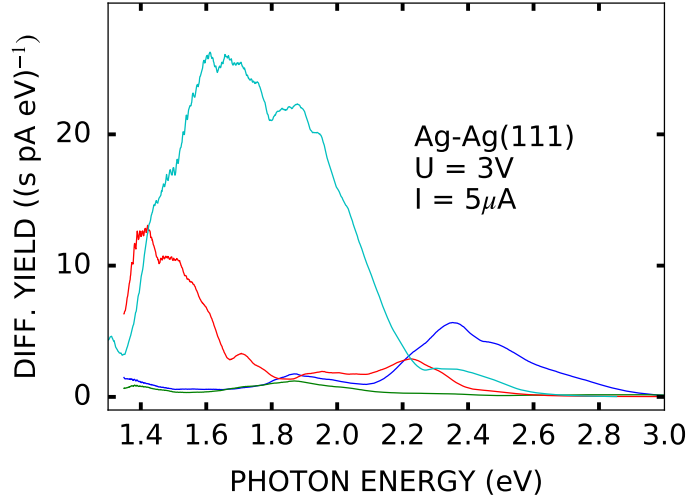


Figure 4.1: Light spectra with highest/lowest overall yield and with peak position at highest/lowest photon energy, respectively, as analyzed in Fig. 4.2. All recorded with the same Ag bulk tip, but the tip apex modified between measurements, on a Ag(111) sample, tunneling parameters were $U=3\text{V}$, $I=5\mu\text{A}$. Spectra were corrected for photon energy dependent relative detection efficiency, but not for absolute efficiency.

with a different tip. The spectra were corrected for the photon energy dependent relative sensitivity of the detection setup, but not for absolute detection efficiency. The data are shown as differential yield, which is the spectrally resolved photon count rate divided by the current. The apparently increased noise at low photon energies is an artifact due to the detector sensitivity dropping from its maximum value at around 2.2 eV towards zero at 1.2 eV. The wavelength resolution was 8.9 nm for the detector parameters used, this corresponds to an energy resolution of 13.9 meV (63.2 meV) at a photon energy of 1.4 eV (3.0 eV); all given as full width at half maximum (FWHM).

The spectra do not exhibit any sharp features, the major peaks are some 100 meV wide in all observed spectra. However, spectra recorded with different tips differ substantially. A wide range of maximum positions and yields is observed. To reduce the complexity of the spectra during comparison, I will first focus only on the most dominant feature, the photon energy with the highest photon rate.

Fig. 4.2a shows the height of the maximum of the differential yield vs. its position. It includes values extracted from 48 different spectra, all recorded under the same tunneling conditions (bias $U=3\text{ V}$, current $I=5\text{ }\mu\text{A}$) with the

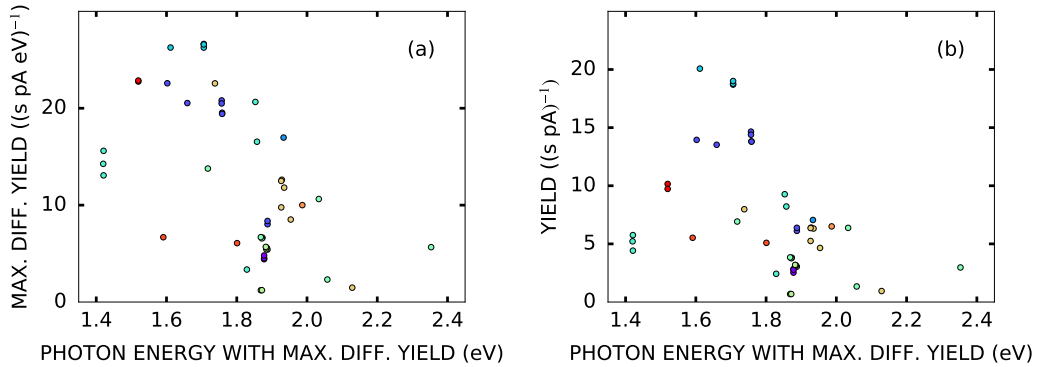


Figure 4.2: (a) The height of the maximum in the yield spectrum vs. the position of the maximum, evaluated for 48 different spectra. All spectra were recorded with the same bulk Ag tip and Ag(111) sample, but the tip apex modified by contacting tip and sample surface at $U=3\text{V}$ and respectively high currents, thus dropping or picking up material or reshaping the tip. All spectra were recorded on a flat terrace. All spectra were recorded at $U=3\text{ V}$, $I=5\text{ }\mu\text{A}$, using the grating with a blaze wavelength of 500 nm . Spectra were corrected for relative efficiency of the detection setup, but not for absolute efficiency due to the limited solid angle covered by the optics. Colors indicate spectra recorded at the same day.

(b) Yield vs. position of the maximum in the spectrum for same spectra as used in (a). The yield was determined by summing up the counts with photon energies of $1.35 - 2.85\text{ eV}$ ($435 - 918\text{ nm}$) and dividing by the current.

same Ag bulk tip and Ag(111) sample. Each spectrum was recorded on a flat (111)-terrace, several 10 nm away from the next step edge. Between measurements the tip apex was modified by forming a contact with a conductance of many G_0 at elevated bias (up to 5 V). Because such treatment most often yields a very unstable tip, it was afterwards stabilized by gently touching the surface with the tip, as it is described in section 3.3. Because the topography of the sample is usually changed in this process by either picking up sample material or dropping tip material, the tip modifications were done in a different location than the light measurements. Finally the tip stability was tested on the flat surface. If the tip was found to be stable, measurements continued, otherwise contact formation was continued until the tip was stable.

The spectra used in Fig. 4.2 were recorded over the course of several days, each measurement day indicated by a different color. The light collecting optics had to be retracted once a day for helium refilling and were thus readjusted every day before the measurements. Since there is no way to quantitatively verify the repeat accuracy of the adjustment, even though carefully conducted,

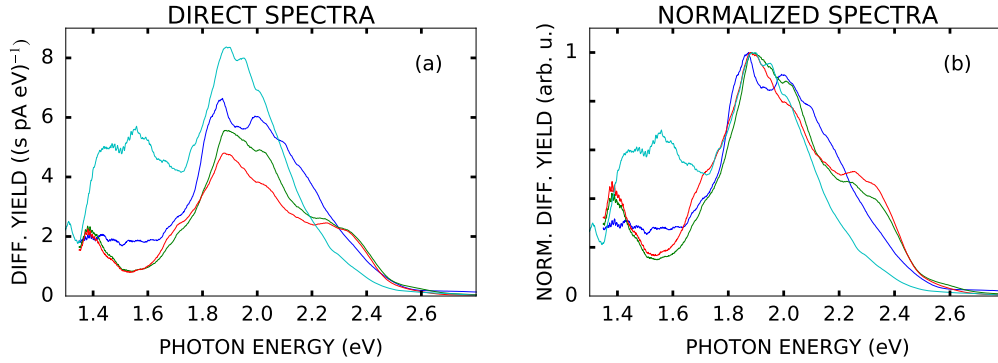


Figure 4.3: (a) Four spectra with similar position of the maximum. All recorded with the same Ag tip, but the tip apex modified between measurements, on a Ag(111) sample, tunneling parameters were $U=3$ V, $I=5$ μ A. Spectra were corrected for relative efficiency of the detection setup, but not for absolute efficiency due to the limited solid angle covered by the optics. (b) The same spectra, normalized to equal maximum value.

this procedure might lead to a different absolute sensitivity of the measurement between different days. However, the differences in the detected yields within one day are stronger than between days and there is no single day with significantly different results. This indicates sufficient accuracy of the adjustment of the optics.

As can be seen, the position of the maximum varied between 1.53 eV and 2.35 eV. The height of the maximum also varied by a factor of 29. There is a weak negative correlation between maximum position and maximum height; the height is more likely to be small when the maximum is at higher photon energies.

Fig. 4.2b shows the yield vs. the position of the maximum for the same spectra as in Fig. 4.2a. In this case the yield is the total photon count rate in the energy range of 1.35 – 2.85 eV divided by the current. In this approach there is a maximum at 1.61 eV. However, the values for spectra with low maximum position might be falsely small, because the spectra are cut off by the vanishing detector efficiency and the intensity at smaller photon energies is not detected.

Spectra with similar position of the maximum can still be quite different. This can be seen in Fig. 4.3, which shows four of the spectra analyzed in Fig. 4.2 that have a maximum at 1.88 eV. All spectra exhibit lots of structure with several secondary peaks or shoulders, but except for the maximum none

of these match well between spectra.

Theoretical description of the plasmon modes

Several models have been developed to predict the light spectrum from STM contacts. While the models differ in complexity, they all assume rather symmetric tips.

An early model that was applied to light emission from the STM is the model of Rendell and Scalapino (RS-model) [37, 38]. This model considers a tunnel junction between a flat surface and a spherical nano-particle⁴ made of free-electron-like metal. For particles with a diameter much larger than the particle-surface distance, a situation typical for the metal-insulator-metal system studied at that time, but also for STM, the plasmon is predicted to be confined beneath the particle, i.e. in the tunneling gap, and to not significantly extend to the other side of the particle. The model should thus also work for an STM junction, if the tip apex can be approximated by a sphere reasonably well. In the RS-model “surface plasmons localized by spherical particles are represented by an infinite set of discrete levels lying below the planar surface-plasmon frequency of the particle material. The imaginary parts of the dielectric functions cause these levels to broaden and possibly overlap. The positions of the levels are determined by the ratio of oxide spacing to particle radius” [38]. So, the RS-model has a single degree of freedom. In an STM context this would be the ratio of tip-sample distance and tip apex curvature. The model predicts the photon energies of the local maxima, but all spectra with the same global maximum should be exactly the same. In this model the variations found for spectra with the same maximum position (Fig. 4.3) cannot be explained.

Using similar geometries Johansson et al. [45, 67], Madrazo et al. [68] and Johansson [66] all found similar results for the plasmon resonance. The quantitative difference in their results stemmed from different consideration of the coupling between plasmons and current.

Aizpurua et al. [46] departed from the plane-sphere system and instead used “a hyperbolic tip geometry where the aperture of the tip and its apex curvature can be changed independently”, thereby introducing an additional degree of freedom. They find the tip aperture has “large impact on the po-

⁴Other particle geometries are also considered. However, in the context of STM light emission the result for spherical particles is usually used.

sitions of the peaks”, with peak positions resembling those found in the RS-model, while the very apex is more important for the overall intensity. Within this model the properties of the maximum in the spectra (as shown in Fig. 4.2) can be understood: two tips with similar aperture will have spectra with maxima at similar energies, but if the tip apexes differ, they can have maxima with different intensity. Aizpurua et al. [69] used the model to quantitatively explain the observed shift of the maximum in the spectrum when changing the tip-sample distance. However, for Ag-Ag(111) contacts the model predicts spectra consisting of neatly separated Lorentzian-like peaks, unlike most of the observed spectra (comp. Figs. 4.1, 4.3).

Meguro et al. [70] recorded scanning electron microscopy (SEM) images of Au STM tips they used to measure light emission from Au(111) surfaces with. One important aspect of their findings is, that the tips do not exhibit rotational symmetry and the shape of the tip apex is better described by an ellipsoid. They explain the observed spectra as the result of the short and the long axis of the ellipsoid resonating independently, thus yielding a spectrum that is similar to the sum of two spectra from spherical apexes with different diameter. A similar analysis, using the RS-model, while allowing two radii of curvature, with similar results was conducted by Boyle et al. [71].

Meguro et al. [70] also point out that the distance relevant for tunneling, which is basically the distance between the front-most atom of the tip and the sample surface, and the distance relevant for the plasmon resonance, which has to be considered as the average over a much larger area, are not necessarily then same. The tip might have small protrusions that carry the current and set the tunneling distance, while the rest of the tip apex is rather flat and thus makes for a different distance concerning the plasmons. This is backed by the shown SEM images, especially for a very blunt tip where several nano-tips are visible. While not explicitly mentioned in their article, this has further consequences than just the necessity to consider two different distances. All of the aforementioned theories on STM light emission consider the current to be coaxial with the symmetry axis of the tip. If the current is off-center with respect to the cavity, this changes the coupling between plasmons and electrons, which poses an additional degree of freedom. Wu and Mills [72] studied the consequences of the lateral displacement on the coupling between the dipole moment of a molecule and the plasmons, which is very similar to the coupling between current and plasmons. Not only do they find the

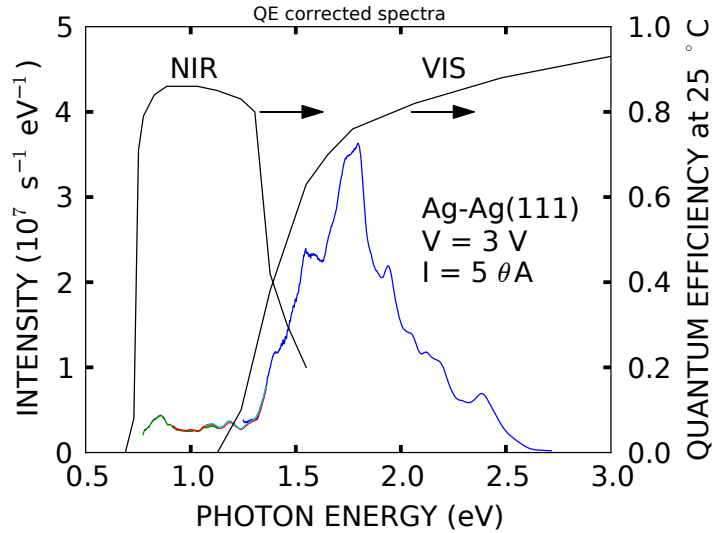


Figure 4.4: Light spectra from a Ag-Ag(111) junction at $V=3$ V and $I=5$ μ A, along with the quantum efficiencies (QE) as provided by the manufacturers. The spectra are corrected for the respective QE. The data recorded with the infrared detector (NIR) have been magnified by a factor of 25, to match the visible spectrum (VIS) in the overlapping range (see text). To extend the detection range, three measurements with different grating positions recorded with the NIR detector are shown and indicated by different colors.

displacement to influence the overall coupling but also the energy dependence of the coupling.

Observed light spectra - extended range

Fig. 4.4 shows spectra from the same junction recorded with two different detectors, along with the quantum efficiencies of the detectors as provided by the manufacturers, in direct comparison. All spectra are corrected for the quantum efficiency as provided by the manufacturers. The IR detector was used at -90°C and the VIS detector at -40°C to limit their otherwise high dark current, which may reduce the quantum efficiencies of the detectors. However, the quantum efficiency is only specified at 25°C for both detectors and additionally at -100°C for the VIS detector. On the right-hand side of Fig. 4.4, energies of 1.25 eV and more, is a spectrum recorded with a standard Si CCD array. On the left-hand side are 3 spectra recorded with a InGaAs photodiode array, indicated by different colors. To cover a range wider than possible with a single measurement the grating of the spectrometer has been turned between measurements. To account for the different collection efficiencies of

the two spectrometers used, the different detector sizes, and the different detector temperatures, the low-energy spectra were multiplied by a factor of 25, so the spectra match in the overlapping energy range. The change in detection efficiency caused by this is small, as can be seen by the rather good match of the overlapping spectra in the photon energy range of 0.7-1.4 eV.

The result of this procedure is a spectrum covering the photon energy range of 0.7-2.7 eV, that is corrected for the major variations of the detection efficiency. It has a pronounced peak at 1.75 eV and many minor features at different energies. In the detection range of the IR detector the light spectrum does not show significant peaks. At 1.0 eV the corrected light intensity is 14 times less than the maximum.

The low energy range of the spectrum is particularly interesting, as most publications so far focus only on the experimentally more easily accessible visible range. From all the models assuming smooth and rotation symmetric tips [37, 38, 45, 46, 66, 67] the intensity is expected to drop towards smaller photon energies in a smooth manner, similar to the tail of a Lorentzian peak. However, in the present case the intensity is significant throughout the detectable infrared range and exhibits a complicated structure at all detected photon energies.

In the high energy range the intensity drops to almost zero already significantly below the expected threshold of $h\nu = eU$. Plasmon modes are, however, expected to be found at energies up to $h\nu_p$, where ν_p is the plasma frequency of the sample material. The plasma frequencies are $h\nu_p = 9.04$ eV (Ag), 8.84 eV (Au), 8.76 eV (Cu) [73]. While the sensitivity of the complete detection setup drops slightly between 2 and 3 eV⁵, this is not a measurement artifact. As pointed out by Johansson [66] this is caused by absorption due to interband transitions in the sample. These transitions present an alternative de-excitation path for the plasmons and thus reduce the light emission.

Conclusion

While the plasmon modes immanent to the tip-sample-junction of the STM can in principle be theoretically predicted, one usually does not have enough information about the precise shape of the tip apex to get useful results. Even small tip changes, as they are very often observed during high bias, high current

⁵This is mostly an effect of the grating, which has a blaze energy of 2.48 eV. In Fig. 4.4 only the detector sensitivity is used, which is the dominating contribution for low photon energies.

situations, may change the spectrum significantly. Also the plasmon modes change with the tip-sample distance, which has to be considered, when comparing spectra acquired at different tunneling conditions. For situations where the distance dependence is not expected to be important, it is still necessary to check whether the tip shape is unchanged or not. The best way to do this is to record a light spectrum under the same conditions before and after any other measurements, if these match, the tip is most likely unchanged.

4.3 Normalization

A quantitative analysis of STM light spectra is difficult, because they are influenced by the strongly varying plasmon function, which is different from tip to tip. In this section I will describe a normalization procedure that removes the influence of the plasmon function. Conveniently, it also removes the influence of the photon energy dependent detection efficiency of the setup. The normalized intensity will later be used to determine the local temperature, which is not possible from the raw spectrum directly (see section 4.5). The normalized intensity is also important for the analysis of multi-electron processes (see section 5).

According to Eq. 4.4 one can isolate the influence of the plasmon function on the photon emission rate from all other parameters: If one records spectra at different bias, while leaving the tip-sample distance constant, the plasmon resonance function Pl will be unchanged in all these spectra and changes in the observed light intensity are only due to the integral. With the abbreviation

$$g(h\nu) = \int T(\varepsilon) [1 - T(\varepsilon)] \rho_i(\varepsilon) f_i(\varepsilon) \rho_f(\varepsilon - h\nu) [1 - f_f(\varepsilon - h\nu)] d\varepsilon \quad (4.5)$$

this can be written as

$$R(h\nu) = \frac{2\pi}{\hbar} Pl(h\nu) g(h\nu) \quad (4.6)$$

The ratio of two spectra, recorded at different bias and constant tip-sample distance becomes

$$\frac{R_{V_1}(h\nu)}{R_{V_2}(h\nu)} = \frac{\frac{2\pi}{\hbar} Pl(h\nu)g_{V_1}(h\nu)}{\frac{2\pi}{\hbar} Pl(h\nu)g_{V_2}(h\nu)} \quad (4.7)$$

$$= \frac{g_{V_1}(h\nu)}{g_{V_2}(h\nu)} \quad (4.8)$$

where R_{V_i} is the spectrum recorded at bias V_i . A similar normalization was used by Schneider et al. [61]. While this expression is independent of the plasmon resonance function it is still complicated. However, if we choose the parameters in a way that we are able to predict g_{V_2} reasonably well, this is a way to measure g_{V_1} as the normalized photon rate

$$R_{norm}(h\nu) = \frac{R_V(h\nu)}{R_{V_{ref}}(h\nu)} \tilde{g}_{V_{ref}}(h\nu) \quad (4.9)$$

$$= \frac{g_V(h\nu)}{g_{V_{ref}}(h\nu)} \tilde{g}_{V_{ref}}(h\nu) \quad (4.10)$$

$$\approx g_V(h\nu) \quad (4.11)$$

where $\tilde{g}_{V_{ref}}$ is the prediction of $g_{V_{ref}}$, and R_V and $R_{V_{ref}}$ are measured spectra. I will call the denominator of the fraction, $R_{V_{ref}}$, the reference spectrum or simply reference. Under ideal conditions, none of its features show up in the normalized intensity R_{norm} . It might seem like this normalization does not gain much, since we have to know the excitation function of the reference spectrum to calculate the normalized intensity, which is approximately the excitation function of the other spectrum. As we will see shortly, this is still useful, because the normalization function can be predicted very well for some photon energies, while it is strongly influenced by one or more parameters at other photon energies.

Concerning the prediction \tilde{g} it is helpful to further simplify the model, to isolate its major features. Assuming all of the input parameters (T , ρ_i , ρ_f) to be constants works surprisingly well. Ignoring the energy dependence of the transmission probability should work best in high conductance situations, where the energy dependence of the elastic transmission is weak and the energy dependence of the inelastic transmission can therefore be expected to be weak as well. High conductance is usually used when measuring light spectra from the STM, to achieve sufficiently high light intensity. Also the effect of the

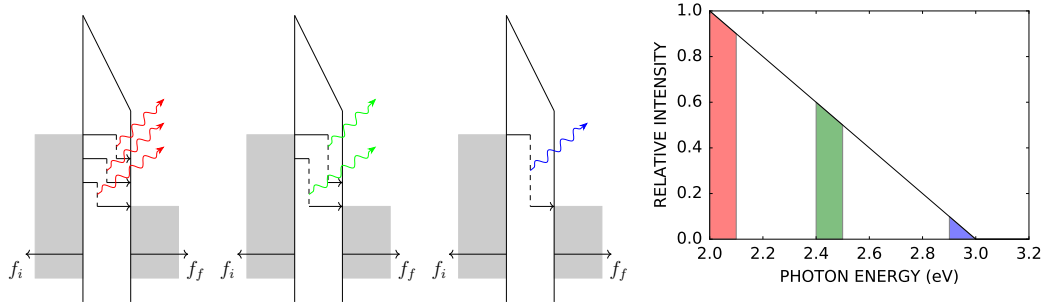


Figure 4.5: (left) Schematic representation of inelastic tunneling for three different photon energies. The higher the photon energy, the smaller the number of combinations of initial and final energies with matching energy difference. (right) The resulting relative intensity from single electron processes, if all densities of states and the transmission probability are constant. In this case the photon emission rate is equal to $\tilde{g}_V(h\nu)$. It drops linearly towards $h\nu = eU$, $U=3V$ in the present case, and is zero for higher photon energies.

density of states is only important if it has sharp features. The consequences of non-constant transmission is considered later (see section 4.6). One can thus approximate g as

$$\tilde{g}_V(h\nu) = c \int f_i(\varepsilon) [1 - f_f(\varepsilon - h\nu)] d\varepsilon. \quad (4.12)$$

In the limit of temperature $\theta = 0$ the Fermi functions are step function and this becomes

$$\tilde{g}_V(h\nu) = c \int_{h\nu}^{eV} \Theta(eV - h\nu) d\varepsilon \quad (4.13)$$

$$= c[eV - h\nu]\Theta(eV - h\nu) \quad (4.14)$$

where c is a constant and Θ is the Heaviside step function. So, g drops linearly towards the threshold energy $h\nu = eV$ and is 0 for higher photon energies. The process is schematically shown in Fig. 4.5. The lower the photon energy, the more possible combinations of initial and final electron states with matching energy difference contribute to the emission. This kind of linear cut-off was already used by Lambe and McCarthy [15] to describe the spectra from metal-insulator-metal structures and is consequentially also found in many STM related publications.

Figure 4.6 shows spectra recorded at different bias in the infrared as well

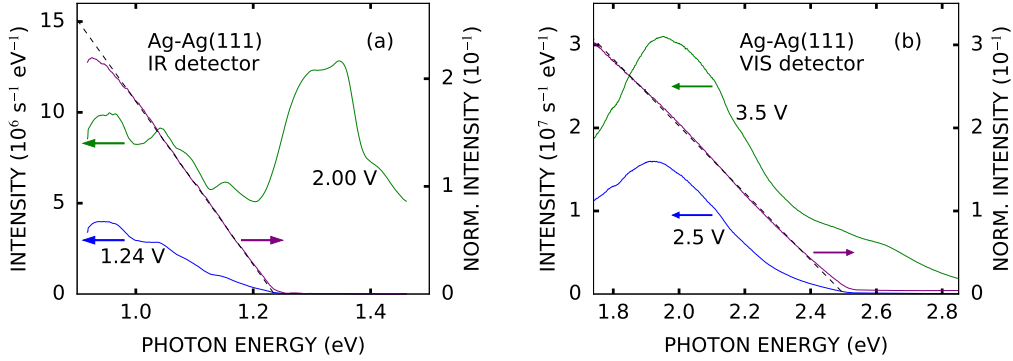


Figure 4.6: (a) Infrared and (b) visible range light spectra of a Ag-Ag(111) junction at different bias (left-hand side scale), along with the normalized intensity (right-hand side scale) as defined by Eq. 4.9. The spectra in (a) were recorded at constant current $I=5 \mu\text{A}$ with one tip, the spectra in (b) were recorded with another tip at constant conductance $G = 0.1 G_0$ and accordingly currents of $27.1 \mu\text{A}$ and $19.5 \mu\text{A}$, respectively. The dashed straight lines are least-square fits to the normalized intensities.

as in the visible range. Also shown is the normalized intensity as defined by Eq. 4.9, using the spectrum recorded at higher bias as reference. Dashed straight lines are least square fits to the normalized intensities. Because the normalized intensity is approximately the excitation function of the spectrum in the numerator in Eq. 4.9, we expect it to also decrease linearly with the photon energy. This predicted linear behavior is found over a wide energy range in both cases. The deviation for energies $h\nu < 1 \text{ eV}$ can be understood as a detector artifact: In grating spectrometers, like the one used here, the second diffraction order is detected at one-half of the real photon energy. Since the detection efficiency is small but non-zero for energies up to 2 eV , this contributes to the intensity in the 2 V spectrum and thus falsely lowers the normalized intensity. Around $h\nu = 1 \text{ eV}$ the normalized intensity deviates from the linear behavior due to non-zero temperature (see next section). At photon energies $h\nu > 1 \text{ eV}$ the intensity does not drop to zero in the detected range. This is due to two-electron processes (see section 5).

So, the normalization according to Eqs. 4.9 and 4.14 is self-consistent in the one-electron energy range $h\nu < 1 \text{ eV}$. In the case of Fig. 4.6a it works well, even though the two spectra were not recorded at constant height, but at constant current. In this situation the plasmon function may or may not change noticeably in the relevant energy range and care must be taken, when using the method. Fig. 4.7 illustrates this with an example. It shows two

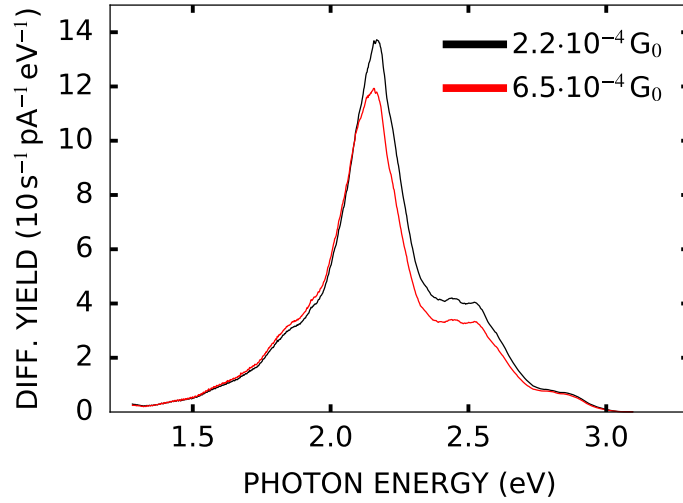


Figure 4.7: Spectrally resolved yield, defined as spectrum divided by the current, for constant bias $V = 3$ V and currents of 50 and 150 nA. The change in tip-sample distance that leads to the different current also changes the plasmon resonance.

spectra recorded with the same tip and the same bias but different current and thus different tip-sample distance. The spectrally resolved yield is clearly changed, but only in the photon energy range of 2.1 – 2.8 eV. For smaller and bigger photon energies the spectrum is nearly unchanged and the normalization procedure described above would still work.

4.4 Conduction Channels, Fano Factor

The emission of light and the current noise are closely related phenomena [22–24]. While the details of that relation are still subject of an ongoing discussion, it is commonly accepted that they have the same dependence on the conductance, when systems like a tunneling junction are studied. In the Landauer-Büttiker model [74–78] the conductance of a narrow conductor is the sum of the conductances of one or more independent conduction channels:

$$G = G_0 \sum_i \tau_i \quad (4.15)$$

where τ_i is the transmission coefficient of channel i , ranging from 0 to 1. A completely open channel has a conductance of $G_0 = \frac{2e^2}{h}$. The model is used extensively for explaining the behavior of current fluctuations (or current noise) in narrow conductors. For low temperature situations the expected value for the power spectral density of the current noise is $P_S = 2eI$, as found by Shottky [79]. However, for narrow conductors it was observed that the actual noise P is reduced by the Fano factor

$$F = \frac{P}{P_S} \quad (4.16)$$

$$= \frac{\sum_i \tau_i (1 - \tau_i)}{\sum_i \tau_i}. \quad (4.17)$$

For a single contributing conductance channel, this simplifies to $F = 1 - \tau$. The lowest possible Fano factor at a given conductance occurs, if only one channel at a time is partially open and all others either fully closed or fully open. Higher Fano factor values are always possible, if more than one channel is partially open. Figure 4.8a shows possible single channel transmissions vs. the total conductance of the junction. The solid lines represent the most extreme case, where the channels open one after the other and at any given total conductance only a single channel is partially open, while all others are either completely closed or completely open. The dashed lines represent an arbitrarily generated case, where more than one channel is partially open most of the time. Figure 4.8b shows the resulting Fano factor vs. the total conductance. At integer multiples of G_0 the Fano factor drops to zero, if the channels open one after the other, since at those values all channels are either fully open or fully closed. In the case of more than one partially open channels, the suppression

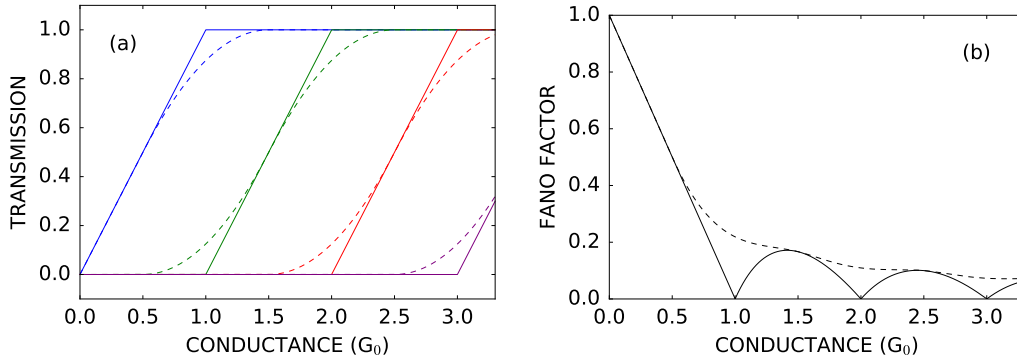


Figure 4.8: (a) The transmission of 4 consecutively opening conduction channels vs. the total conductance. The solid lines represent the most extreme case, where only a single channel is partially open and all others either completely closed or completely open. The dashed lines represent a possible, but otherwise arbitrarily generated, case, where more than one channel is partially open for conductances $G > 0.5 G_0$. (b) The Fano factor resulting from the transmission values shown in a).

is not complete and the Fano factor is finite for all conductances values.

Noise reduction as described by the Fano factor was experimentally observed in break junction [25, 80] and STM experiments [48, 81].

Schneider et al. [48] were the first to link the non-linear current dependence of STM light emission to the suppression of shot noise in quantum point contacts. They found that the photon yield, defined as the photon count rate divided by the current, drops almost linearly for conductances of 0–1 G_0 . The suppression is incomplete, though: even at $G = 1 G_0$ light emission is observed. This is exactly what is expected for the current noise, if there is only a single, partially transparent channel available in the tunneling range and an additional channel starting to contribute when tip and sample almost touch. From the similar behavior of the shot noise and the light emission Schneider et al. reason “that the current shot noise of a quantum point contact leads to the emission of sub-PHz radiation”.

The important result is, for the moment, that the light emission is not simply proportional to the current. This observation is the reason Eq. 4.4 does not simply include the tunneling probability T , but a factor $T(1 - T)$.

Calculating the photon yield from Eq. 4.4, by integrating the photon emission rate over a wider energy range, dividing it by the current and approximating $T(\varepsilon)$ by the effective tunneling probability $\tau = G/G_0$, we get

$$Y(G) = \frac{\int_{E_0}^{E_1} R(h\nu, G) d h\nu}{I(G)} \quad (4.18)$$

$$\approx \frac{\frac{2\pi}{\hbar} Pl_{eff} \tau(G) [1 - \tau(G)]}{\tau(G)} \quad (4.19)$$

$$\propto \frac{\frac{G}{G_0} (1 - \frac{G}{G_0})}{\frac{G}{G_0}} \quad (4.20)$$

$$= 1 - \frac{G}{G_0}. \quad (4.21)$$

So, if there is only a single relevant conduction channel, modeling the photon emission rate as Eq. 4.4 leads to a linear conductance dependence of the yield, as it is experimentally observed over a wide range for silver contacts. If the photon emission rate was proportional to the current, the yield would be constant.

When studying the light intensity as a function of the conductance, the intensity is usually integrated over a wider photon energy range. This may have the effect that changes in the plasmon resonance function, especially a shift of the resonance positions with a change of the tip-sample distance as it is clearly observed, do not strongly influence the yield, as long as they happen within the integration range and not near the integration limits. The detailed energy dependence of the plasmon resonance function is therefore replaced by an effective plasmon factor Pl_{eff} .

At zero temperature the light emission from a contact with a conductance of $1G_0$ should be strictly zero, if Eq. 4.4 would be a complete model. This is, however, not observed (see e.g. Ref. [48]). This could be caused by the contribution of more than one conduction channels to the overall conductance or, as it was also stated occasionally, by a finite temperature. Both effects could be superimposed.

As we will see in the next section, the temperature is clearly influencing the spectra, but it does not explain the observed light intensities coming from $1G_0$ contacts. Under the circumstances of any experiments covered in this text, at least one partially open conductance channel is necessary to have a significant light intensity. In such a situation the overall light intensity is expected to be the incoherent sum of the respective single channel intensities, similar to the shot noise result, and the yield does not simply depend on the conductance linearly but is proportional to the Fano factor (Eq. 4.17).

4.5 Effect of finite temperature - Spectral Thermometry

In attempts to measure the local temperature of structures of nanometer size, many different techniques have been utilized. Two level conductance fluctuations (TLF) have been used as tool for temperature measurements of narrow metal contacts[82–84]. “The TLF’s are believed to be related to switching of a defect in the constriction region between two stable positions.”[84] The defects were found to couple to the current and thus to be heated above lattice temperature and electron temperature.

Henny et al. [85] measured the current noise of 140 nm wide and 20 nm thick Au wires. For wires significantly shorter than the electron-phonon mean free path l_{e-ph} , they found the electron temperature to be proportional the applied bias U , for wires significantly longer than l_{e-ph} they found the electron temperature to be proportional to $U^{2/5}$. Unlike in the previous cases there is no tunneling involved, which might alter the heating process.

Finally, light emission was used to extract temperature information. Schneider et al. [48] compared the conductance dependence of the overall light intensity with the zero-frequency result for shot noise of a single conductance channel. They found that at a conductance of $G = 0.93 G_0$ and a bias of $U = 1.6 V$ a temperature of 2000 K would be necessary to explain the observed behavior. At the same time they note that increased temperature is not the only involved effect. So, while being related, this method is not adequate to serve as temperature probe directly.

In a more recent publication Schneider et al. [61] attributed the presence of light at photon energies above the threshold of $h\nu = eU$ to a non-equilibrium electron distribution, where the majority of the electrons is cold and a small fraction ($\lesssim 10^{-3}$) of the electrons is very hot: 2200, 2500, 2700 K for $I=10 \mu A$ and $U=1.2, 1.4, 1.6 V$, respectively.

Buret et al. [86] studied Au junctions prepared by electromigration. In an approach very similar to that of Downes et al. [30], they interpreted the light spectra as the result of a black body radiator with the emission efficiency modified by the plasmon resonance and extracted electron temperatures as high as 2000 K at 1.7 V bias and 100 μA current. Downes et al. [30] studied light from W-Au STM junctions and extracted even higher temperatures up to 9000 K.

Using the result of this thesis so far, a better temperature analysis can be done. As will be shown shortly, the light intensity at photon energies $h\nu > eU$ is to some extent the result of an increased local temperature. This can be used as an effective temperature probe.

Assuming constant density of states and transmission probability the normalized intensity was approximated as Eq. 4.12. In the zero temperature case the integrand simplifies to be either unity or zero, for finite temperature this is not the case. The smooth changing of the Fermi function at the Fermi energy allows inelastic electron transitions with an energy difference higher than $h\nu = eU$. Furthermore it also softens the cutoff of the normalized intensity in the range of some $k_B\theta$ around that energy.

At finite temperature it is also possible for inelastic transitions to happen within one electrode, in addition to the inelastic tunneling from one electrode to the other also possible at zero temperature. Inferring from results of noise measurements (see Appendix A for details) the complete expression for the one-electron photon emission rate from a single conduction channel is

$$R(h\nu, \theta) = \frac{2\pi}{\hbar} Pl(h\nu) \int_0^\infty d\varepsilon \left[\tau(1 - \tau) \sum_{\alpha \neq \beta} f_\alpha(\varepsilon, \theta) (1 - f_\beta(\varepsilon - h\nu, \theta)) + \tau^2 \sum_\alpha f_\alpha(\varepsilon, \theta) (1 - f_\alpha(\varepsilon - h\nu, \theta)) \right] \quad (4.22)$$

with the plasmon resonance Pl and the temperature dependent electron distribution $f_x(\varepsilon, \theta)$ in electrode x . The integration variable ε is the initial energy of the electrons undergoing inelastic transition with energy difference $h\nu$. The first part of the sum considers inelastic transitions from occupied states in one electrode to unoccupied state in the other electron (inter-electrode transitions), while the second part considers inelastic transitions within the electrodes (intra-electrode transitions).

Figure 4.9 visualizes the complete excitation function, including inter-electrode and intra-electrode transitions, for different temperatures. The plot is normalized, so that the excitation function is 1 for zero photon energy and zero temperature. Along with the direct value shown as solid lines, differences between the finite temperature excitation function and its $\theta = 0$ value, magnified by a factor of 100, are shown as dashed lines. The contribution of intra-electrode

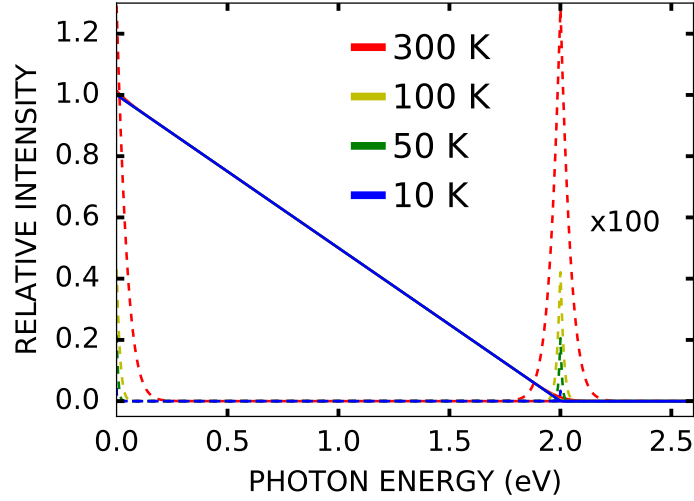


Figure 4.9: The photon rate, calculated from Eq. 4.22, vs. the photon energy for different temperatures as solid lines. A constant plasmon function $Pl(h\nu) = 1$ was used, so this represents the extended excitation function (the integral in Eq. 4.22), which includes inelastic inter-electrode transitions, as well as inelastic intra-electrode transitions. The plot is normalized, so that the excitation function is 1 for zero photon energy and zero temperature. The differences between the finite temperature excitation function and its $\theta = 0$ value, magnified by a factor of 100, are shown as dashed lines.

transitions, corresponding to the right-hand sum term in Eq. 4.22 is concentrated at small photon energies and rolls off exponentially. Up to room temperature it is completely negligible in the visible and near-infrared range that is experimentally accessible. The contribution from the inter-electrode transitions also rolls off exponentially, but is centered at the cut off energy $h\nu = eU$, because the electrodes are biased. For photon energies between these two regions, the excitation function is essentially temperature independent. The linear drop of the relative intensity vs. the photon energy is still observed for photon energies higher than a few times $k_B\theta$ up to energies a few times $k_B\theta$ below the threshold $h\nu = eU$. This is the reason we can use the zero temperature approximation for the reference spectrum in the normalization. One only has to make sure the bias for the reference measurement is high enough, so that the temperature effects are unimportant in the photon energy range of interest.

Focusing on the photon energy range around the threshold $h\nu = eU$, one can extract the temperature at the tip-sample junction from the normalized intensity by fitting the excitation function to it. Figure 4.10a visualizes this

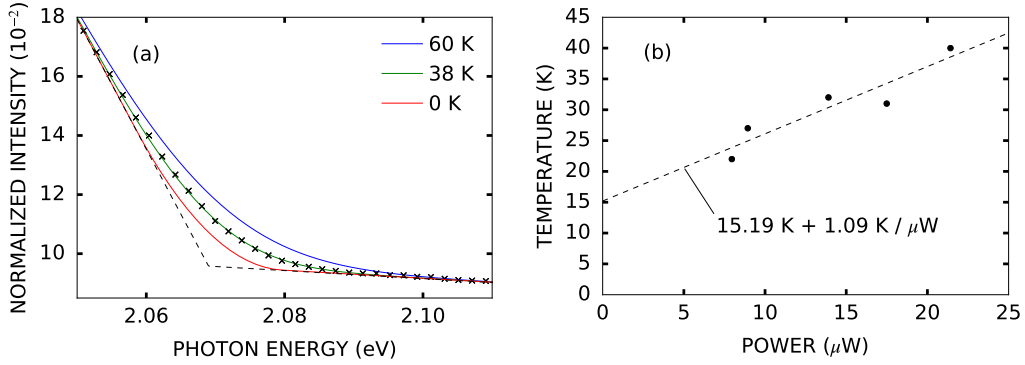


Figure 4.10: (a) Light spectrum, recorded from a Ag-Ag(111) junction at $U=2.066$ V, $I=20$ μ A, as normalized intensity over photon energy. The reference spectrum used for normalization was recorded at $U=3$ V, $I=20$ μ A. The solid lines are spectra calculated from Eq. 4.12 for 3 different temperatures, taking the finite energy resolution into account by convoluting the model result with a boxcar function. The intensity from higher order processes is temperature independent in this energy range and was used as a background (see section 5 for details). For comparison, the dashed line is a spectrum calculated from Eq. 4.12 for a temperature of 0K and infinite energy resolution. (b) Temperatures over electrical power from 5 different spectra, recorded at constant height. The temperatures were extracted from best fits to the spectra as shown in (a). Before opening the feedback loop tunneling parameters were $U=3$ V, $I=15$ μ A. The dashed straight line is a least-square fit to the data, the fit parameters are shown in the figure. The limited resolution of the detection setup has been considered.

procedure. It shows, as crosses, the normalized intensity of a Ag-Ag(111) contact at bias $U=2.066$ V and current $I=20$ μ A. The dashed line is the excitation function for zero temperature. It includes the intensity from two-electron processes, which is temperature independent in the covered photon energy range (see section 5 for details) and is only considered as a background. The solid lines are the excitation function evaluated for different temperatures while considering the finite resolution of the detection setup, which also leads to a smoothing of the cutoff, by convoluting the model result with a boxcar function corresponding to the apparent line width (compare section 3.4 D). By fitting the excitation function to the normalized intensity this way, the temperature can be extracted. Figure 4.10b shows the resulting temperatures from 5 spectra recorded at constant height. The tunneling parameters were $U=3$ V, $I=15$ μ A before opening the feedback loop. The dashed straight line is a least square fit to the data.

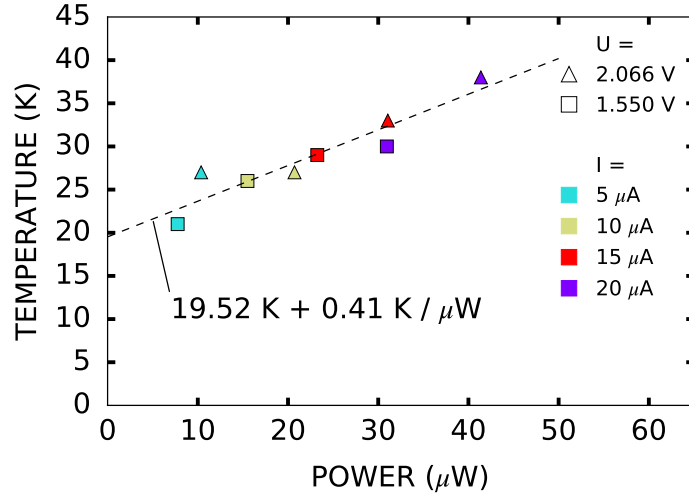


Figure 4.11: Temperatures over electrical power from 8 different spectra, recorded at different tunneling parameters. The symbol shape indicates the applied bias, the color indicates the current. The temperatures were extracted from best fits to the spectra as shown in Fig. 4.10a. The limited resolution of the detection setup has been considered.

Figure 4.11 shows the results of a measurement series analyzed in the same manner, but this time not at constant height, but changing bias and current independently. The shape of the symbol indicates the bias, the color indicates the current. The measurements were done with a tip different from that used in Fig. 4.10. Again the dashed straight line is a least-square fit to the data. There is no obvious difference in the effects of increased bias or increased current, the important quantity is the dissipated power.

There is usually a very good quantitative fit between the model prediction of the spectrum and measured values (see e.g. Fig. 4.10). In this sense the method just described offers a better explanation for the observed spectra than the interpretations mentioned in the beginning of this section. As is described in appendix B, the model of Schneider et al. [61] fails to explain the smooth transition of the spectrum at $h\nu = eU$, but predicts a sharp kink instead. While the data shown here (e.g. Fig. 4.10) cannot rule out the presence of a tiny non-equilibrium component of the steady state electron distribution, it is difficult to reconcile with a scenario where the majority of the electrons remains completely cold. The spectral shape around $h\nu = eU$ changes upon changing the current through the junction. This indicates that at least partial thermalization does occur.

Unlike in the case of Schneider et al. [61], the temperatures of up to 2000 K extracted by Buret et al. [86] are meant as (local) equilibrium temperature. While the junction geometry used by Buret et al. [86] is different than in a STM (two opposing pointed electrodes rather than one pointed and one flat), the model derived in section 4.1 should still hold. However, their findings are incompatible with the results shown in this thesis, especially the linear photon energy dependence of the normalized intensity (see e.g. Fig. 4.6). Also, as we will see in section 5, their interpretation fails to explain the conductance dependence of the above threshold light, further reducing the plausibility of their results.

Interpretation

As Berndt et al. [14] proved, STM light emission shares the high resolution of the STM itself and can thus be done with atomic resolution. The temperature measurement just described is therefore local to the tip-sample junction.

For the fit it is assumed that the electrons in both electrodes obey a Fermi-Dirac distribution with the same temperature. This is not obviously the case. The different geometry of tip and sample might lead to different heat conduction away from the junction. Considering only the electrons a higher thermal conductivity of the sample is expected compared to the narrow cone of the tip. However, this may be compensated by the increased cooling of the electron gas due to higher electron-surface and electron-defect scattering, as the crystal lattice within the tip apex is most likely distorted as a result of the tip preparation [87]. In addition to these effects one should expect more power to dissipate in the electrode at the more positive potential as a result of the energy dependent tunneling probability. Electrons have a higher probability to leave the negative electrode near the Fermi energy and thus being injected high above the Fermi energy of the positive electrode. This effect is less pronounced when the tip-sample distance is small. Finally, the assumption of a Fermi-Dirac distribution is not obvious. The high current density and electric field in the junction pose a severe non-equilibrium situation and a local equilibrium in either electrode might not be present. This argument was used by Schneider et al. [61] to explain the light emission at photon energies $h\nu > eU$. However, as it is shown in appendix B, at least a partial thermalization of the electron at the junction is necessary to explain the smooth transition of the spectrum at $h\nu = eU$.

With these limitations in mind the temperature can still be interpreted as the effective temperature of the electron gas in the immediate vicinity of the junction. It is the temperature that leads to the same light emission, if both electrodes were at the same temperature and local equilibrium were assured. The very good fit between normalized intensity and finite temperature excitation function (see Fig. 4.10a) suggests that this is at least a very good approximation.

The temperature of the STM body was approximately 6 K during the measurements. The y-intercept of the least-square fitted straight line does not match this value, but gives temperatures of 15-20 K. Also, the temperature at zero power differs from tip to tip. This is, however, no contradiction and can be understood from the design of the STM surroundings. The temperature measurement at the STM body was designed for a situation where there is no significant heat introduction to the STM and everything within the innermost stage is considered to be in thermal equilibrium. The temperature measurement is therefore done at the side of the stationary part of the STM, a few centimeters away from the tip, so it does not interfere with tip and sample handling. With the radiation shields of the innermost stage in optimal position the temperature is usually measured 5.0 – 5.2 K. For the light collection it is necessary to open a window in the radiation shield and to introduce the lens assembly, which is coupled to the liquid nitrogen stage by a small copper braid. This usually leads to an increase of the temperature to around 5.8 K, depending on the orientation of the lens assembly, which in turn depends on the length and orientation of the tip. This increase in temperature is expected to be stronger in tip and sample than in the stationary STM body, because the sample is mounted on the slider, which has to be able to move and is consequentially without good thermal contact to the rest of the STM. The lens is close to tip and sample and the radiative heating is thus acting directly onto them. So the increased temperature for zero dissipated power in Figs. 4.10 and 4.11 could be explained by radiative heating of tip and sample in combination with the weak thermal coupling between the sample and the STM body. This would also explain the difference between the Fig. 4.10 and Fig. 4.11, as the orientation of the lens assembly varies from tip to tip.

4.6 Energy dependent transmission probability

The model described so far reproduces important features of experimental results: for most measurements the conductance dependence is reproduced well, except for conductances near the quantum conductance $G = G_0$. It also describes the dependence of the spectrum on the applied bias with good agreement to experimental results, except for a background that can be attributed to multi-electron processes (see section 5 for details). However, there are also observations that cannot be explained by this model.

Figure 4.12 shows conductance dependent yield measurements, recorded with a Ag-coated W-tip over a flat terrace of a Ag(111) sample. The symbol shape indicates independent measurement series, the symbol color indicates the used bias. The data were normalized for every measurement series independently, so that the linear extrapolation is 1 for zero conductance. A straight line fit to the normalized data at small conductances ($G < 0.4 G_0$) intersects the x-axis at $0.8 G_0$. This means that the yield drops faster than one would expect it for a single conductance channel with energy independent transmission, where the intersection would be at $1 G_0$. For noise measurements similar behavior was observed only if a single atom of a material that is ferromagnetic in bulk form (like Fe or Co) was at the tip apex [27]. It was interpreted as a result of the spin of the single atom carrying the current which selectively allows only the transmission of electrons with one spin direction at a time, so that a single conduction channel has a maximum conductance of $0.5 G_0$. This effect is not expected for a pure Ag tip. For noise measurements on Ag the lowest observed Fano factor is given by $F = (1 - G/G_0)$, a single, spin-independent conduction channel has a maximum conductance of $1 G_0$.

One of the simplifications used so far was the assumption of an energy dependent transmission probability $\tau = G/G_0$. This is also commonly used in the analysis of current noise, where the measurements are done under small bias, usually a few mV [27, 80]. For experiments on light emission, like they are covered in this work, a bias of a few V might be used, so the approximation of constant transmission might not be a good one. In the following the effects of this approximation on the photon emission rate and the conductance dependent yield will be scrutinized.

Equation 4.4 gives the photon emission rate as a function of the photon energy. Assuming a constant density of (electron) states and energy independent transmission $\tau = G/G_0$, corresponding to a single conduction channel in

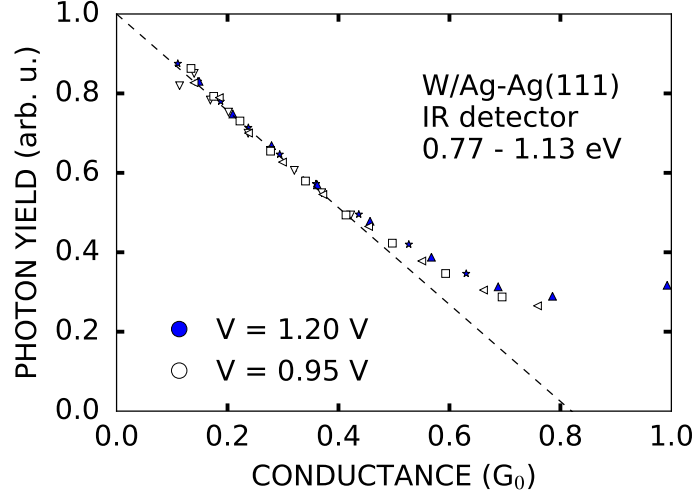


Figure 4.12: Yield, defined as photon count rate divided by the current, vs. conductance, recorded with a Ag-coated W-tip over a Ag(111) sample. The photon energy range of 0.77 – 1.13 eV was considered. The symbol shape indicates independent measurement series, the symbol color indicates the used bias. The data were normalized for every measurement series independently, so that the linear extrapolation is 1 for zero conductance. The dashed straight line is a least-square fit to the normalized data at $G < 0.4 G_0$.

the Landauer model, this becomes

$$R(h\nu) = \frac{2\pi}{\hbar} Pl(h\nu) \int_{-\infty}^{\infty} d\varepsilon \tau(1 - \tau) \sum_{\alpha \neq \beta} f_{\alpha}(\varepsilon) [1 - f_{\beta}(\varepsilon - h\nu)]. \quad (4.23)$$

At zero temperature, $\theta = 0$, this simplifies to

$$R(h\nu) = \frac{2\pi}{\hbar} P(h\nu) \tau(1 - \tau) [|eU| - h\nu] \Theta(|eU| - h\nu) \quad (4.24)$$

with the Heaviside step function Θ . For photon energies well below $h\nu = eU$, this is still a good description of the observed behavior even if the system is actually at a temperature $\theta > 0$.

Considering only elastic tunneling, the tunneling current can be derived in a one-dimensional model using the WKB approximation to be

$$I(U, z) \propto \int_{-\infty}^{\infty} \rho_t(\varepsilon) f_t(\varepsilon) \rho_s(\varepsilon) [1 - f_s(\varepsilon)] T(\varepsilon, U, z) d\varepsilon \quad (4.25)$$

$$T(\varepsilon, U, z) = \exp\left(-z \frac{\sqrt{8m}}{\hbar} \sqrt{\frac{\phi_s + \phi_t}{2} + \frac{U}{2} - \varepsilon}\right) \quad (4.26)$$

with the reduced Planck's constant \hbar , density of states ρ_t (ρ_s) and Fermi-function f_t (f_s) in the tip (sample), bias U , and tip-sample distance⁶ z [88–90].

T is the probability for an electron occupying a state at energy ε , relative to the Fermi energy, in one electrode to go into an empty state in the other electrode. It is a consequence of the non-vanishing value, and therefore overlap, of tip and sample wavefunctions within the potential barrier. The lower the electron energy the higher the effective barrier height and thus the tunneling probability. At contact ($z = 0$) the transmission probability is 1 for all energies⁷. When increasing the distance between tip and sample the transmission probability drops exponentially, the lower the electron energy (and thus higher the effective barrier) the faster.

There are more sophisticated models of the tunneling current. Based on the work of Bardeen [91], Tersoff and Hamann derived a now common approximation for the tunneling probability⁸ T for an s-type wave function at the tip apex [92, 93]. This model was later extended to generalized wave functions by Chen [94, 95]. However, Eq. 4.26 gives a qualitatively correct result for the distance and energy dependence of the current and is thus chosen for its simplicity.

It may seem natural to use this transmission probability T to consider the influence of the distance on the photon rate. However, it is not obvious at which energy to evaluate T , since in the inelastic case two different energies (before and after the transition) might be considered. As is shown in appendix D, qualitatively similar results occur for all possible combinations of transmissions at initial and final energy. The following discussion is therefore done with an arbitrarily chosen case. Taking T at the energy of the initial state the transition rate at energy $h\nu$ becomes

⁶To enhance the readability of the text and because there is little chance of confusion, I will refer to the tip-sample distance simply as distance in this section

⁷Note that Eqs. 4.25 and 4.26 were derived in a situation where the potential barrier is significant, so it does not correctly describe the current at small distance / high conductance or even at contact.

⁸In the cited articles the tunneling matrix element $M_{\mu\nu}$, between states ψ_μ and ψ_ν , is studied. For a clear distinction from the transition matrix element for the inelastic processes, this notation is not used here.

$$R(h\nu) = \frac{2\pi}{\hbar} Pl(h\nu) \int_0^{eV} d\varepsilon T(\varepsilon, U, z) [1 - T(\varepsilon, U, z)] \rho_t(\varepsilon) \rho_s(\varepsilon). \quad (4.27)$$

Figure 4.13a shows two spectra for different bias calculated this way as solid lines, assuming Pl , ρ_t , and ρ_s to be constant⁹, and using a distance for each spectrum that leads to a conductance of $G = 0.1 G_0$. For comparison it also shows two spectra calculated with constant transmission $\tau = 0.1$ as dashed lines. While in the constant transmission case the spectra drop linearly towards $h\nu = eU$, the spectrum calculated after Eq. 4.27 exhibits a non-linear shape. In Fig. 4.13a the light intensity from Eq. 4.27 is higher for all photon energies than in the constant transmission case. This is not a general feature, though. Close to $G = G_0$ (not shown here) the light intensity calculated after Eq. 4.27 is lower than for Eq. 4.23. All spectra studied in this work involve at least one unknown constant factor, so it is not possible to compare absolute intensities. To take this into account the constant transmission spectra are also shown multiplied with an adjustable factor, determined by least square fitting, as dotted lines.

Even though there is a qualitative difference between the spectra from Eqs. 4.23 and 4.27 it is difficult to compare the model predictions to experimental data directly, as the shape of real spectra is always strongly influenced by the plasmon resonance $Pl(h\nu)$. Spectra can be compared though, when normalized as described in section 4.3.

Fig. 4.13b shows the 2.5 V spectrum from Fig. 4.13a, normalized according to Eq. 4.9, using the 3.5 V spectrum as reference. It also shows the difference of the normalized spectrum from a straight line, multiplied with a factor of 100. The difference is so small (less than $3 \cdot 10^{-3}$ for all photon energies) that the deviation from a straight line is hard to detect. So, for spectra recorded at constant height, the difference between a model spectrum calculated with constant transmission τ and one calculated with energy dependent transmission $T(\varepsilon)$ is almost completely suppressed by the normalization. This is the case even though the normalization uses the assumption of a linear cutoff of the reference spectrum.

While an energy dependent transmission probability at constant distance

⁹ ρ_t and ρ_s were chosen so that the conductance of the junction $G = I/U$ would be G_0 for $z = 0$, calculating I from Eq. 4.25 with a temperature of 0 K.

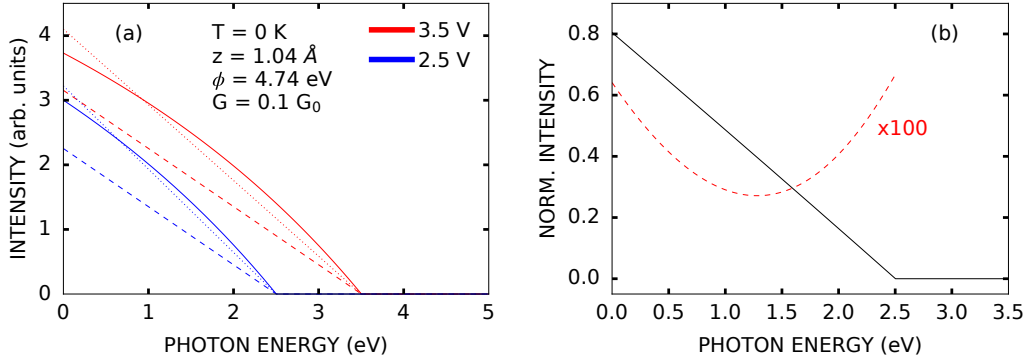


Figure 4.13: (a) Spectrum calculated with Eq. 4.27 (energy dependent transmission), assuming $Pl, \rho_t, \rho_s = const.$, as solid lines. For comparison spectra calculated with Eq. 4.23 (energy independent transmission), using $\tau = 0.1$, are shown directly as dashed lines and multiplied with an arbitrary factor as dotted lines.

(b) The 2.5 V spectrum from (a) normalized after Eq. 4.9, using the 3.5 V spectrum as reference, as solid line. The difference of the normalized intensity from a straight line, multiplied by 100 and shifted upwards by 0.4, is shown as dashed line.

has no significant impact on the normalized intensity, this is not expected when comparing different distances. Most notably, reducing the distance increases the current, which also influences the photon emission rate. A common way to take this into account is to divide the spectra by the current and compare the spectrally resolved (or differential) yield instead of comparing intensity spectra directly. Furthermore, the distance has influence on the relative tunneling probability. The current changes differently at different electron energies, so the differential yield will still be influenced by a distance change. Finally, the distance influences the light emission also via the plasmon function Pl . Reducing the distance shifts the maximum of the plasmon function towards smaller photon energies and enhances overall emission, increasing the yield [66].

Figure 4.14 shows spectrally resolved yield curves for constant bias and different distances calculated with Eq. 4.27 and assuming $Pl, \rho_t, \rho_s = const.$ Overall the yield is smaller for smaller distances, which is also the case for energy independent transmission τ . For small distances the spectrally resolved yield curve is indistinguishable from a straight line, similar to the result for energy independent transmission probability. The bigger the distance, the more the yield curve deviates from a straight line, with the yield growing

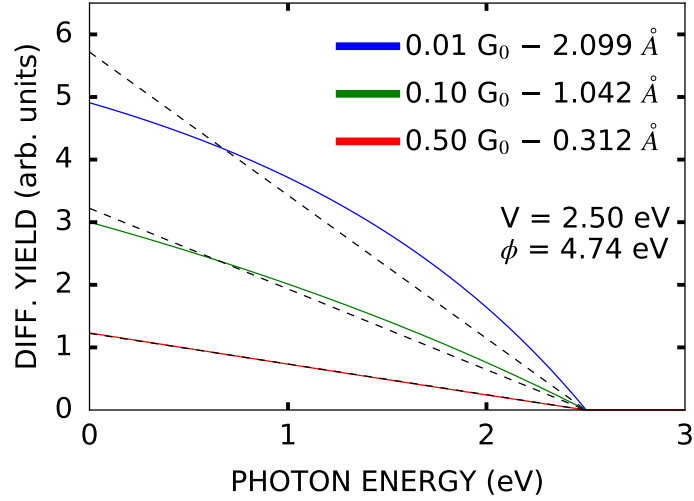


Figure 4.14: Spectrally resolved yield, defined as spectrum divided by current, for different tip-sample distances and constant bias, calculated with Eq. 4.27, assuming $Pl, \rho_t, \rho_s = const.$ Due to the constant plasmon function Pl this is identical to the excitation function. Dashed straight lines are least square fits under the conditions to vanish at $h\nu = eV$. For high conductances the yield drops almost linearly like it is the case for constant transmission probability, for small conductances the deviation is substantial.

faster for high photon energies than for low photon energies. Reducing the distance would therefore shift the maximum of the spectrum towards smaller photon energies, if we considered a non-constant plasmon resonance function $Pl(h\nu)$.

This is illustrated in Fig. 4.15. Figure 4.15a shows a spectrum calculated with Eq. 4.27 as solid line, using energy dependent transmission probability from Eq. 4.26, a Lorentzian function $Pl(h\nu) = \frac{\gamma}{(\gamma^2 + (h\nu - E_{res})^2)}$ as plasmon function, and assuming $\rho_s, \rho_t = const.$ The Lorentzian is located at $E_{res} = 2.1 eV$ and has a half-width of $\gamma = 0.2 eV$. The resulting spectrum is similar to one that might be observed from a Ag-Ag(111) junction, however, E_{res} and γ are chosen arbitrarily for this example. Also a real spectrum is more complicated than a Lorentzian, which does not matter for this example that only focuses on the maximum. In addition to the total spectrum the two constituents, the plasmon function Pl and the excitation function, are shown separately as dotted and dashed line, respectively. To highlight the position of the maxima, the spectrum and the plasmon function are scaled separately to have a maximum of 1. In addition the position of the respective maxima are indicated

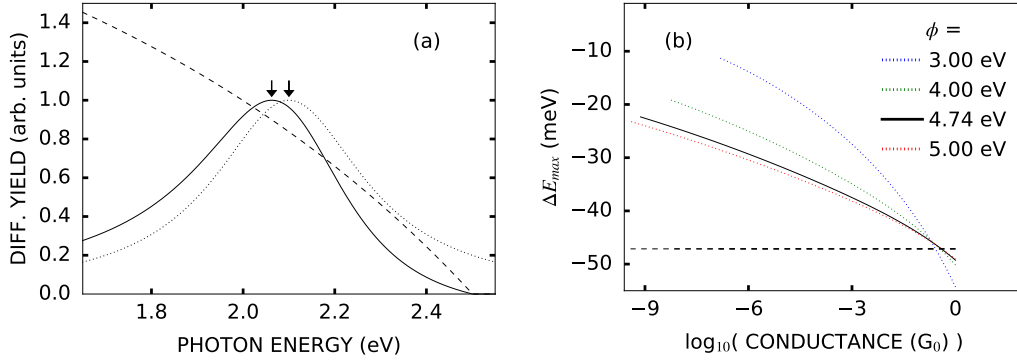


Figure 4.15: (a) Example spectrum calculated with Eq. 4.27, using energy dependent transmission from Eq. 4.26, as solid line, along with its components, the plasmon function as dotted line and the excitation function as dashed line. The plasmon function and the total spectrum were scaled to a maximum of 1.0 separately to simplify the comparison of the positions of the maxima. A Lorentzian function located at 2.1 eV and a half-width of 0.2 eV was used as plasmon function, chosen arbitrarily for this example (see text for details). The excitation function is the 0.01 G_0 case from Fig. 4.14. The bias is $U = 2.5$ V. The two arrows mark the maximum of the plasmon function and the total spectrum, respectively.

(b) (solid line, dotted lines) Difference between the photon energy of the maximum in the spectrum calculated from Eq. 4.27 and the photon energy of the maximum of the plasmon resonance $Pl(h\nu)$ (this is the distance between the arrows in (a)) vs. conductance on a logarithmic scale. The solid line was calculated with the the work function of Ag(111), the dotted lines correspond to different, arbitrary work functions as indicated. (dashed line) Same evaluation for spectra calculated from Eq. 4.24 (energy independent transmission) for comparison. All curves cover distances from 1 nm to contact.

by arrows. Since the excitation function is decreasing with photon energy, the maximum of the total spectrum is at a lower energy than the maximum of the plasmon function. The difference between these two maxima ΔE_{max} depends on the curvature of the excitation function. As it has just been shown (see Fig. 4.14) the curvature of the excitation function depends on the distance, if energy dependent transmission as in Eq. 4.26 is considered. This is evaluated quantitatively in Fig. 4.15b. It shows the difference between the photon energy of the maximum in the spectrum and the photon energy of the maximum in the plasmon resonance function $P(h\nu)$ (the distance between the arrows in Fig. 4.15a) as a function of the conductance. The solid line corresponds to the work function of Ag(111). Distances from 1 nm to contact are covered, resulting in conductances of approximately $10^{-9} - 1 G_0$. In this range the shift

of the maximum changes from -22.3 to -49.3 meV. For comparison the same evaluation is also shown for the case of energy independent transmission probability as dashed line, where the spectrum was calculated from Eq. 4.23. In this case the shift of the maximum is -47.1 meV, independent of the conductance as the curvature does not change with the distance. The transmission probability uses the average of the work function of the sample and that of the tip as the effective work function. Since the structure of the tip, and hence its work function, are unknown, the effective work function might differ from that of the plain surface. The dotted curves in Fig. 4.15 correspond to arbitrarily chosen work functions of 3-5 eV to illustrate the influence of the work function. The smaller the work function the more the shift of the maximum in the spectrum does vary with the conductance. The maximum shift, which is observed at contact, also increases with decreasing work function.

The above example assumes a plasmon resonance function independent of the distance to isolate the effect of the electron transmission. This might, however, not be a good approximation. For a Ag-Ag(111) contact, with tip shape that leads to maximum emission at around 2 eV, Johansson [66] predicts a shift of the maximum of the spectrum by -210 meV for a distance change from 1 to 0.5 Å as a result of changes in the resonance. This has the same sign and is an order of magnitude bigger than the effect of the energy dependent transmission, as it is considered here. In contrast, within their more complex model, Aizpurua et al. [46] find the energy of modes with full azimuthal symmetry, which are the only ones to be excited by the current at the symmetry axis, to increase with decreasing distance, so the shift has different sign. Aizpurua et al. [69] used this model to quantitatively explain the shift of the maximum position in measured spectra for a Au-Au(111) contact, with the maximum at around 1.83 eV. For a distance change from 1 to 0.5 Å a shift of -5.4 meV is observed. This result is compatible with the results shown above, as it includes the effect of the electron transmission as well as the change of the resonance function. The resonance shift partially compensates the effect of the distance dependent electron transmission.

To observe the aforementioned effects, a spectrally resolved measurement is necessary. Anyway, measurements that integrate over an extended photon energy range, e.g. with a PMT (see section 3.5), may also be influenced by an energy dependent transmission probability. Figure 4.16a shows the light intensity, integrated for photon energies of 1.5 - 2.0 eV, vs. the conductance. The

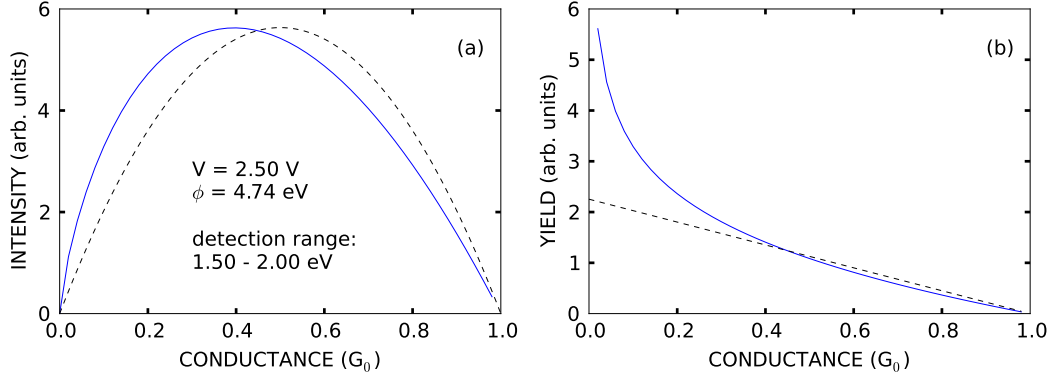


Figure 4.16: (a) Integral light intensity vs conductance, (solid line) calculated from Eq. 4.27, using energy dependent transmission and (dashed line) Eq. 4.23, using energy independent transmission. The detection range corresponds to wavelengths of 620 - 827 nm. The 1e-light cutoff is 496 nm. (b) The same data divided by the conductance, giving the photon yield.

solid curve results from Eq. 4.27, where energy dependent transmission from Eq. 4.26 is assumed. The dashed curve is the result for energy independent transmission. In the energy independent case the light intensity is proportional to $\tau(1 - \tau)$, with $\tau = G/G_0$, which has a maximum at $G = 0.5 G_0$. In the energy dependent case the curve is skewed towards smaller conductances, with the maximum at $0.4 G_0$ for the parameters used. Figure 4.16b shows the same data represented as photon yield, calculated by dividing the curves from Figure 4.16a by the conductance. The yield drops linearly to zero at $1 G_0$ in the energy independent case. For the case of energy dependent transmission the yield curve is non-linear, with a more negative slope at small conductance and a less negative slope at high conductance. The observed yield in Fig. 4.12 is qualitatively similar to that in Fig. 4.16b. So the yield dropping faster than expected for a single conduction channel might be the result of an increased yield at photon energies near the threshold $h\nu = eU$ for small conductance due to the distance dependent change of the transmission probability. However, this is not the only effect that might be involved:

The increasing emission enhancement of the plasmon function upon reducing the distance affects the intensity and yield the opposite way, skewing the intensity curve towards higher conductances and therefore reducing the yield curve slope at small conductance and enhancing it at high conductance. Without a quantitative model of the plasmon resonance function, which would depend critically on the shape of the tip in a region tens of nm wide, which

is usually completely unknown, it is not possible to predict *a priori* if these effects cancel out or if one dominates. Beyond that the shift of the resonance maximum could have a huge impact on the integral intensity or yield if the resonance maximum is near one of the edges of the detection range. If the resonance maximum is shifted into the detection range, this might cause an increase of the detected intensity, even if the general trend was decreasing intensity and vice versa if the maximum is shifted out of the detection range.

The elastic transmission of Eq. 4.26 was derived within a theory that assumes an opaque potential barrier. This has to be taken into account when interpreting the results shown in Figs. 4.14-4.16. From the incomplete yield reduction at $G = G_0$ one can also deduce that more than a single channel has to be involved.¹⁰ For conductances approaching the conductance quantum the reliability of the results presented here is thus further reduced. However, in the conductance range where the yield was dropping faster than expected ($G < 0.4 G_0$) in Fig. 4.12, this should not matter. The energy dependence of the inelastic transmission might be the cause of the behavior observed in Fig. 4.12, but since it is not the only effect influencing the yield curve, a definite attribution cannot be done for now.

Altogether, the energy dependence of the transmission has some effect on the spectrum as well as on the overall light intensity. As was shown in representative examples, the influence on the spectrally resolved normalized intensity is negligibly small. An influence on the distance dependence of the overall intensity exists but has to be analyzed in comparison to other effects.

¹⁰An analysis of the evolution of several conduction channels with the total conductance was done by Lü et al. [22], who calculated a Ag-Ag(111) junction within a density functional theory non-equilibrium Green's function (DFT-NEGF) approach.

Chapter 5

Light: Multi-Electron Processes

The model established in the former section describes the light emission from a STM junction very well for photon energies up to the threshold $h\nu = eU$. For higher photon energies it predicts no light emission at all for zero temperature. For finite temperatures it predicts an exponentially decaying normalized intensity with increasing photon energy. Because it only contains processes in which exactly one electron gives energy to create exactly one photon, it was referred to as the one-electron model (or just 1e-model). As I will show in this section, the 1e-model is insufficient to quantitatively describe the observed behavior of STM light emission at photon energies $h\nu > eU$. At those energies the observed normalized intensity and the dependence of the overall emission rate on the conductance differ from the model prediction. Finally, I will extend the 1e-model towards a general n-electron model, which is in good agreement with the observed behavior.

5.1 Experimental results

Figure 5.1 shows spectra from a Ag-Ag(111) junction, recorded at different bias. In Fig. 5.1a the light intensity is shown on a linear scale. For three of the curves (0.9 V, 1.0 V, and 1.1 V) bias and detection range were chosen, so that the threshold $h\nu = 2eU$ is visible, which is indicated by arrows for each bias value. These curves were recorded at constant current $I = 30 \mu\text{A}$. The 3 V curve was recorded at reduced current $I = 50 \mu\text{A}$, to reduce the risk of damaging the tip. The intensity of the three low-bias curves drops towards the indicated thresholds, but it does not drop to zero. There is notable intensity at higher photon energies. Figure 5.1b shows the data of the low-

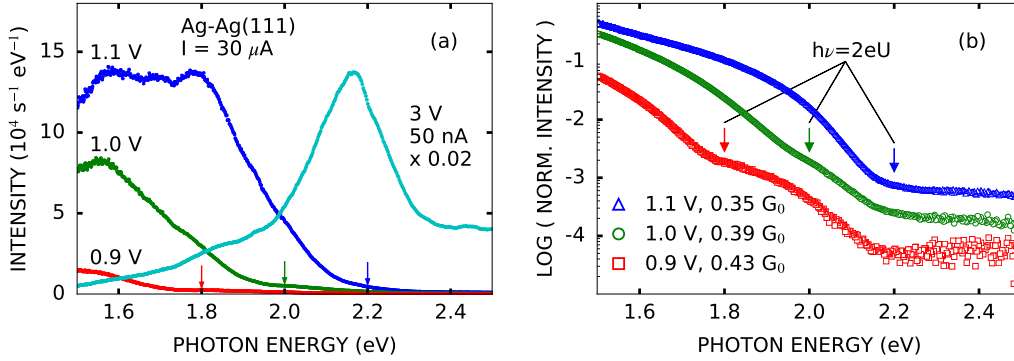


Figure 5.1: (a) Light spectra from a Ag-Ag(111) junction recorded at 3 voltages and constant current $I=30 \mu\text{A}$, along with a spectrum recorded at $U=3 \text{ V}$ and reduced current $I=50 \text{ nA}$. The spectra are corrected for the dark count rate, but not for the spectral sensitivity of the detection setup. The 3V spectra has been scaled down by a factor of 50. The thresholds $h\nu = 2eU$ are marked by arrows.

(b) Light spectra from (a) as normalized intensity on a logarithmic scale. The 3V spectrum was used as reference. (Figure adapted from Ref. [32].)

bias measurements as normalized intensity on a logarithmic scale. The 3 V curve was used as reference in the normalization. At the indicated thresholds there is a change of the slope in each of the curves. While the 1e-model predicts decreasing normalized intensity at increased photon energies, these kinks cannot be explained in that model.

Also at the threshold $h\nu = eU$ the behavior is different than predicted by the pure 1e-model.¹ Figure 5.2 compares the prediction of the 1e-model for different temperatures to the normalized intensity measured from a Ag-Ag(111) junction at photon energies around the threshold $h\nu = eU$. The mismatch is profound. Even at temperatures of 500 K the predicted intensity drops faster than the measured normalized intensity. At the same time the predicted intensity near the threshold is already too high. Increased temperature in the 1e-model is not enough to quantitatively explain the observed spectra, another mechanism must be involved.

Beyond the shortcomings of the 1e-model in the photon energy domain, it also fails to explain the variation of the light intensity with the conductance G at photon energies $h\nu > eU$. For all photon energies it predicts that the photon rate is proportional to a factor $\tau[1 - \tau]$ with $\tau = G/G_0$, as long as a single

¹In section 4.5 this deviation was already taken into account as a “background”. The nature of this background is analyzed in the following.

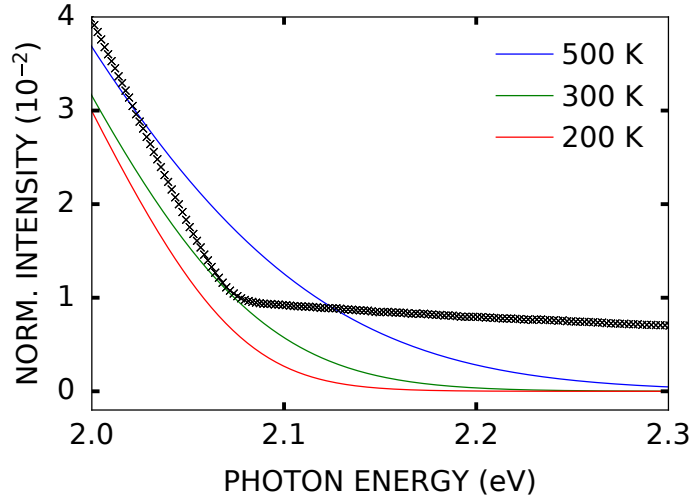


Figure 5.2: Normalized light intensity of a Ag-Ag(111) contact at $U=2.066$ V and $I=20$ μ A. Solid lines are the expected intensity for different temperatures as indicated, calculated from Eq. 4.12, which only considers single-electron processes.

conduction channel can be assumed.² While this is generally in good agreement with the observed behavior for photon energies $h\nu < eU$, for energies $h\nu > eU$ a different behavior is observed. For the energy range $h\nu < eU < 2eU$ this has already been covered in the literature:

In 2003 Hoffmann et al. [31] reported on light emission from a thin Na layer on Cu(111). They found that the light intensity in the photon energy range $h\nu > eU$ increased with the current I approximately as $I^{1.5}$ for small currents, with the exponent decreasing to 1.2 for the highest current they used. They consider two mechanisms as plausible explanations for this “two-electron photon emission”: (i) a coherent Auger-like process in which energy is transferred from one tunneling electron to another and (ii) decay of the hot holes that are injected into the tip. The Auger-like process is deemed the dominating one due to higher calculated intensities. They further note that the quantum well structure is essential in achieving significant signal levels. However, in principle a quantum well structure is not necessary for either of the considered processes.

In 2009 Schull et al. [47] reported a similar behavior for light emission from a Au(111) sample. They found that in the tunneling regime the light intensity follows a power law $R \approx I^\beta$, with $\beta \approx 1.1$ (≈ 1.7) for photon energies below

²See 4.4 for details

(above) the 1e threshold $h\nu = eU$. At high conductance the intensity was deviating from that power law and increasing less with the current.

Schneider et al. [48] noticed the similarity of the photon yield, *i.e.* the photon rate per current, to the Fano factor over a wide conductance range for photon energies $h\nu < eU$. For higher photon energies, $h\nu > eU$, they found the yield to increase with conductance for small conductances and then drop again to a local minimum near $G = G_0$, rising again, and so forth.

For photon energies $h\nu > 2eU$ there are no reports of STM light emission prior to this work. Buret et al. [86] reported on light emission from junctions prepared by electro-migration, also at photon energies $h\nu > 2eU$. However, that system lacks the possibility to alter the conductance of the junction (without destroying it), which is essential to the following analysis.

Conductance dependent yield measurements can be seen in Fig. 5.3. It shows data from two different Ag-Ag(111) contacts, indicated by color and symbol shape. The measurements were conducted with the PMT setup (see section 3.5 for details), using optical filters to limit the detection to the photon energy range $h\nu = 1.77 - 3.10 eV$, therefore only light with $h\nu > 2eU$ contributes to the signal. Since there is no spectral resolution with the PMT setup, to make sure there is no change of the tip shape during the experiment, it was performed in the following manner: roughly the first half of measurement points were recorded with increasing conductance, the remaining points with decreasing conductance, either filling in the gaps or recording at a given conductance value more than once. For the shown measurements, the curves of forward and backward run coincide within the scattering of the individual measurements. In both cases the yield increases for small conductances and goes through a maximum at $0.4 - 0.5 G_0$. In one case the yield only dropped, for conductances of up to $0.8 G_0$, the highest value recorded in that measurement. In the other case the yield exhibits a local minimum at $0.55 G_0$ and increases after that.

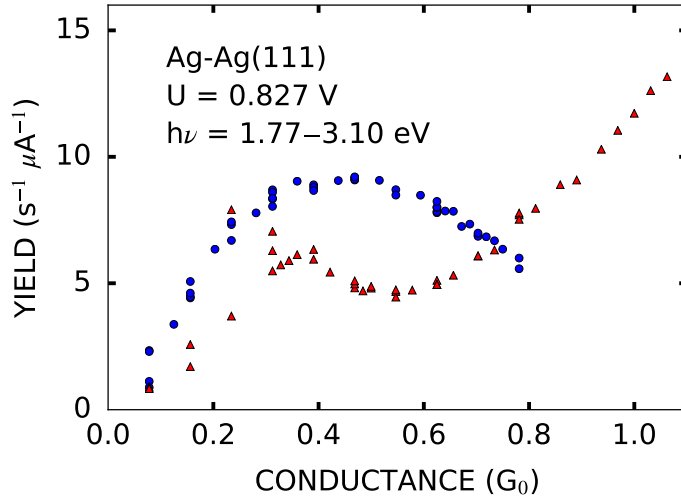


Figure 5.3: Photon yield, defined as count rate divided by the current, vs. conductance from two different Ag-Ag(111) contacts (blue and red symbols). The photon rate was measured with the PMT setup (see section 3.5 for details). Optical filters limited the detection to the photon energy range $h\nu = 1.77 - 3.10$ eV, therefore only light with $h\nu > 2eU$ contributes to the signal. [32]

5.2 Available theoretical approaches

With an analysis similar to that of Tobiska et al. [96], Xu et al. [97] proposed a model in analogy to the dynamical Coulomb blockade. The electromagnetic environment of the tip-sample junction is modeled by a dampened LC circuit. Overbias light, i.e. photons with $h\nu > eU$, is explained as a consequence of “the non-Gaussian statistics of the tunneling dynamics of the electrons”. Their first key result is that the model predicts the spectrum in the photon energy range $eU < h\nu < 2eU$ to have features (like the position of the maxima and minima etc.) very similar to the 1e spectrum at higher bias U . The second key result is that in the photon energy range $h\nu < eU$ the light intensity is proportional to $\tau = G/G_0$, while in the range $eU < h\nu < 2eU$ the intensity is proportional to τ^2 , similar to what is observed experimentally for vanishing conductances G . It is explicitly mentioned that the model is an approximation in the limit of small conductances. The model was recently extended to finite temperatures [98].

Kaasbjerg and Nitzan [99] calculated the current noise to higher order in the electron-plasmon interaction. They find that a plasmon-mediated electron-electron interaction is the source of experimentally observed above-threshold

light emission. Also, they find that the light intensity is proportional to $\tau[1-\tau]$ in the photon energy range $h\nu < eU$ and proportional to $\tau^2[1-\tau]^2$ in the range $eU < h\nu < 2eU$. However, results for spectrally resolved intensities in the $2e$ range are not given explicitly. Effects of finite temperature are not considered.

For completeness two additional explanation have to be mentioned. In an approach very similar to that of Downes et al. [30], Buret et al. [86] explained the occurrence of light emission in the photon energy range of $h\nu > 2eU$ by considering a blackbody-like emitter whose photon energy dependent emission efficiency is modified by the plasmon modes near the junction. This model is incompatible with the spectral thresholds at $h\nu = eU$ and $h\nu = 2eU$ clearly observable in the normalized intensity. Also it fails to explain the different conductance dependence in the photon energy ranges $h\nu < eU$, $h\nu < eU < 2eU$, and $h\nu > 2eU$. A different explanation was provided by Schneider et al. [61]. They suggest a non-equilibrium electron distribution as the cause of photon emission at energies $h\nu > eU$. This electron distribution is a consequence of the high current density and was derived “within a simple model of hot-hole–hot-electron cascades”. The major feature of such distributions is that the vast majority of the electrons remains completely cold, while a small fraction is at high temperature. As it is detailed in appendix B, this model predicts a sharp kink in the spectrum at $h\nu = eU$ and an exponential roll-off at higher energies. In the experimental data shown in this thesis the kink at $h\nu = eU$ is smoothed out increasingly with increased current³ and there is a kink in the spectrum also at $h\nu = 2eU$. Consequentially, a non-equilibrium electron distribution like it was described by Schneider et al. [61] cannot be the only cause of photon emission at energies $h\nu > eU$, even though it might contribute.

5.3 An empirical model

So there is no adequate quantitative model which describes the spectral features as well as the conductance dependence of the photon emission from a STM junction, except for very special circumstances. A multi-electron model must be based on the following observations:

- If the conductance dependence of the 1e-light is $R_{1e} \propto \xi(G)$, the conductance dependence of the light intensity in the photon range $eU < h\nu < 2eU$, is $R_{2e} \propto [\xi(G)]^2$. As we will see soon, the conductance dependence

³This was used to extract the temperature in section 4.5.

of the light intensity in the 3e range $2eU < h\nu < 3eU$ is $R_{3e} \propto [\xi(G)]^3$. In a situation where only a single conduction channel is necessary to describe the behavior, $\xi(G) = G/G_0[1 - G/G_0]$, with the total conductance G and the conductance quantum $G_0 = 2e^2/h$.

- The normalization procedure described by Eqs. 4.9 and 4.14 was used self-consistently in the 1e-model. This procedure removes spectral features, also in the photon energy range $h\nu > eU$. Except for a change of slope at the thresholds $h\nu = eU$ and $h\nu = 2eU$, the normalized intensity drops smoothly and monotonically with the photon energy.
- For photon energies $h\nu > eU$ the energy dependence of the normalized intensity is non-linear.

Considering these observations and the 1e-model of Eqs. 4.5 and 4.6, I propose the following generalized model:

$$R(h\nu) = R_{1e}(h\nu) + R_{2e}(h\nu) + R_{3e}(h\nu) + \dots \quad (5.1)$$

$$R_{1e}(h\nu) = \frac{2\pi}{\hbar} Pl(h\nu) g(h\nu) \quad (5.2)$$

$$R_{2e}(h\nu) = \frac{2\pi}{\hbar} Pl(h\nu) a \int_0^{h\nu} d\varepsilon g(\varepsilon) g(h\nu - \varepsilon) \quad (5.3)$$

$$R_{3e}(h\nu) = \frac{2\pi}{\hbar} Pl(h\nu) b \int_0^{h\nu} d\varepsilon \int_0^{h\nu-\varepsilon} d\varepsilon' g(\varepsilon) g(\varepsilon') g(h\nu - \varepsilon - \varepsilon') \quad (5.4)$$

where R , the total photon rate, is the sum of all distinct processes and $R_{ne}(h\nu)$ is the photon emission rate at photon energy $h\nu$ due to processes involving n electrons at once. Just like in the 1e-model g is given by Eq. 4.5. In all R_{ne} the plasmon function Pl is evaluated at the energy of the photon emission. This is a consequence of the observation that the normalization removes almost all spectral features also at photon energy $h\nu > eU$. The multi-electron excitation function is a generalization of the 1e excitation function that recreates all of the above-mentioned features. In the 2e case the 1e excitation function is considered twice, in the 3e case three times, and so on. This is inspired by the idea that the chance for an inelastic tunneling event where an electron loses energy ε is given by $g(\varepsilon)$ and that, while most of these processes lead to the emission of a photon directly, it is possible for two (or more)

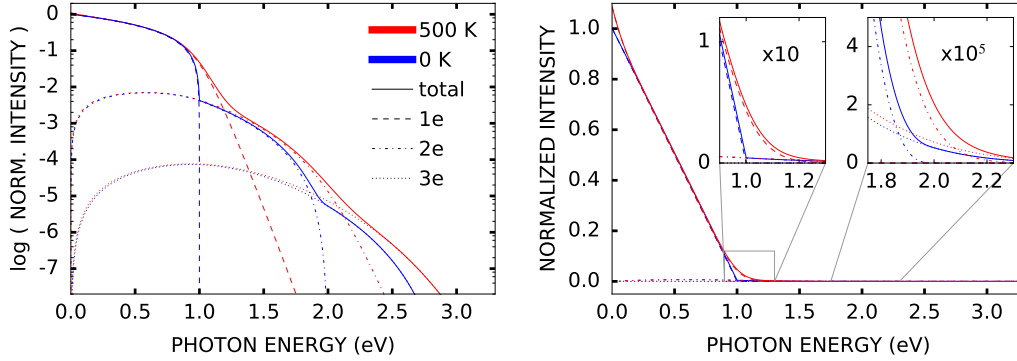


Figure 5.4: Normalized intensity vs. photon energy in a (left) semilogarithmic and (right) linear plot, calculated from Eqs. 5.1-5.4, for two different temperatures, indicated by the color. The solid lines are the total intensities, the dashed, dash-dotted, and dashed lines are the contributions of 1e, 2e, and 3e processes, respectively. A magnified view of the thresholds at $h\nu = eU$ and $h\nu = 2eU$ is shown in the insets of the right panel. Model parameters were $U = 1\text{ V}$, $G = 0.5 G_0$, $a = 10^{-3}$, $b = 10^{-6}$. Transmission was considered energy independent $T(\varepsilon) = G/G_0$. (Figure adapted from Ref. [32])

electrons to excite a single plasmon mode together. For the 1e excitation function it is unimportant if these cooperative excitation processes take place instead of two or more distinct 1e processes or in addition, since higher order processes are orders of magnitude less likely than 1e processes. If one 2e process takes place instead of two 1e processes the correction of the 1e excitation function is still negligible. In the 2e case the integral runs over all possible energy contributions ε from the first electron, while the second electron always contributes the missing energy to create a photon with energy $h\nu$. Similarly in the 3e case, where the first two electrons contribute energies ε , ε' and the third one the missing energy $h\nu - \varepsilon - \varepsilon'$. a and b are constants expressing the relative likelihood of multi-electron processes. Processes involving more electrons would be treated accordingly, but are not considered here due to their low intensity.

Figure 5.4 shows an example result of this model as the normalized intensity vs. the photon energy on a semilogarithmic scale in the left panel and on a linear scale in the right panel. The color indicates the temperature, the solid lines are the total intensities (Eq. 5.1) and the dashed, dash-dotted, and dotted lines are the contributions from 1e (Eq. 5.2), 2e (Eq. 5.3), and 3e processes (Eq. 5.4), respectively. A magnified view of the thresholds at $h\nu = eU$ and $h\nu = 2eU$ is shown in the insets of the right panel.

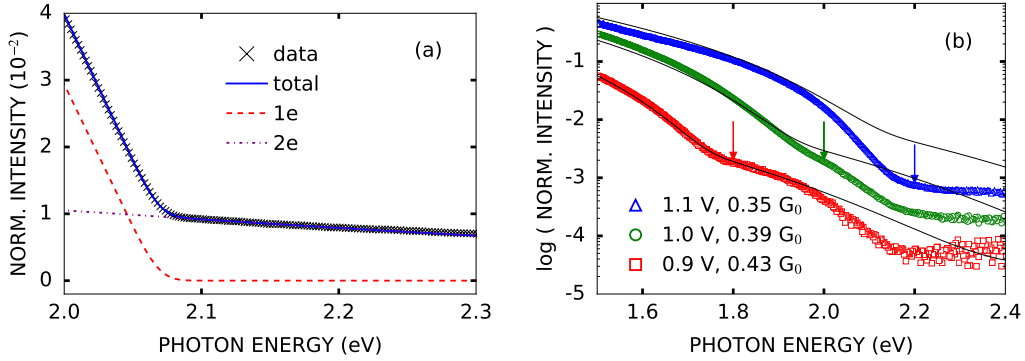


Figure 5.5: (a) Normalized light intensity (Eqs. 4.9,4.14) of a Ag-Ag(111) contact vs. the photon energy. Tunneling parameters were $U=2.066$ V and $I=20$ μ A (this is the same data as shown in Fig. 5.2). The dashed line is the contribution from 1e processes (Eq. 5.2), for a temperature of 38 K; the dash-dotted line is the 2e contribution (Eq. 5.3). The sum of 1e- and 2e-contributions is shown as solid line. The reference spectrum used for the normalization was recorded at $U=3$ V, $I=20$ μ A. The constant a in Eq. 5.3 was $1.396 \cdot 10^{-3}$. The 3e intensity was not considered.

(b) Normalized light intensity of another Ag-Ag(111) contact on a logarithmic scale vs. the photon energy. The spectra were recorded at 3 different bias values U and constant current $I=30$ μ A. The thresholds $h\nu = 2eU$ are indicated by arrows. The solid lines are the total intensity calculated from Eqs. 5.1–5.4. Parameters were $a = 1.8 \cdot 10^{-2}$, $b = 2.52 \cdot 10^{-5}$. The reference spectrum was recorded at $U=3$ V, $I=50$ nA.

In the whole figure the spectral resolution of the detection setup has been taken into account. Densities of (electron) states were considered constant. (Figure (b) adapted from Ref. [32].)

At zero temperature photons from a process involving n electrons are limited to energies $h\nu \leq neU$. For $n = 1$ this creates a sharp kink in the total intensity. For $n = 2$ the kink is less obvious on a linear scale, but the semilogarithmic plot reveals a clear change of the slope near the threshold. At an increased temperature the limit $h\nu \leq neU$ does no longer apply strictly, but the n -electron intensity decreases exponentially with the photon energy beyond the threshold. Due to this the kinks in the total intensity curve are to some extent smoothed out and the position of the kink is shifted to higher photon energies. At $h\nu = eU$ only the 1e intensity changes notably with temperature, the 2e intensity is effectively temperature independent. This is the reason the local temperature could be extracted in section 4.5 with the 1e model and a temperature independent background.

Figure 5.5a shows normalized intensity data from a Ag-Ag(111) contact

for photon energies around the 1e-2e threshold $h\nu = eU$ along with the model results from Eqs. 5.1–5.3. The total intensity is shown as solid line, the 1e and 2e contribution as dashed and dash-dotted line, respectively. Taking the spectral broadening of the detection setup into account the model is in excellent agreement with the measured data for a temperature of 38 K. Figure 5.5b shows normalized intensity data for 3 different bias values recorded with the same tip (but a different one than in Figure 5.5a), at constant current. The solid line is model result from Eqs. 5.1–5.4. The 1e contribution is negligible in this photon energy range, only 2e and 3e processes contribute significantly. For photon energies $h\nu < 2.0 \text{ eV}$ there is good agreement between the model result and the measured data in all three spectra. For higher photon energies there is a notable deviation. A likely explanation for this is the imperfect normalization due to the different tip-sample distances during measurement of the spectra and the reference. As is detailed in section 3.4 the CCD detector suffers from ghosting artifacts, when conducting low intensity measurements after high intensity measurements. To limit this effect and to reduce the risk of modifying the tip, the current was reduced during the reference measurement. Under these circumstances the plasmon function in the spectrum and the reference is not identical and the normalization does not work perfectly, even though it often still works very good in a wide photon energy range (see section 4.3, especially Fig. 4.7). Fig. 4.7 shows two spectra recorded with the same tip as the spectra in Fig. 5.5b, but at different (lower) currents. For photon energies up to 2.1 eV the spectrum is nearly unchanged, for higher photon energies the intensity is reduced in the spectrum with higher conductance (and thus smaller distance). The maximum in the spectrum is also slightly shifted to smaller energies. It is therefore plausible, that the deviation between the model and the spectra in Fig. 5.5b for photon energies beyond 2.0 eV is a consequence of this intensity reduction as a consequence of a different plasmon function in spectrum and reference due to the different distances.

Figure 5.6 shows light spectra from a W/Ag-Ag(100) junction, recorded at different tunneling parameters. Figure 5.6a shows direct spectra, the 1V spectrum was multiplied with a factor of 1000 to match the scale of the other spectra. Figure 5.6b shows the spectra as normalized intensity, using the 3V spectrum as reference to normalize the other two. Along with the data the model results from Eqs. 5.1–5.3 are shown as solid lines. In the case of the 2V spectrum there is excellent agreement between model and data. In the case of

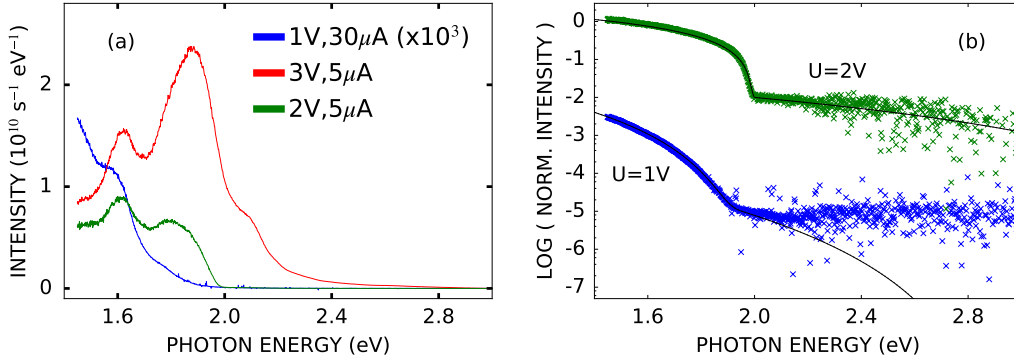


Figure 5.6: (a) Light spectra from a W/Ag-Ag(100) junction recorded at different tunneling conditions as indicated. The 1V spectra was multiplied by a factor of 1000 to enhance visibility.

(b) Same data as in (a) as normalized intensity (Eqs. 4.9,4.14), using the 3V spectrum as reference, as crosses. Along with it the model prediction from Eqs. 5.1–5.4 is shown as solid lines. Model parameters were $a = 2.8 \cdot 10^{-2}$, $b = 1.23 \cdot 10^{-3}$ for the 1V spectrum and $a = 1.9 \cdot 10^{-1}$ for the 2V spectrum.

the 1V spectrum the measured normalized intensity is higher than predicted by the model at photon energies exceed 2 eV. The 1V spectrum was recorded after the 3V spectrum, so this might be a case of ghosting (see section C). In that case a constant normalized intensity is expected, since the ghosting part of the spectrum is proportional to the reference, unless saturation of the trapping sites occurs. The data of Fig. 5.6 were recorded with a different detector than the data analyzed in section 3.4, so the intensity of the ghosting might differ.⁴

The next thing to look at is the conductance dependence of the overall light intensity. Based on the discussion in section 4.6, an energy independent transmission probability $\tau = G/G_0$ is considered.⁵ This approximation holds well as long as only a single conduction channel is involved. The 1e contribution to the photon emission rate R_{1e} is proportional to $\tau[1 - \tau]$. This is part of the excitation function g in Eqs. 5.1–5.4. From that it follows that the 3e contribution R_{3e} is proportional to $(\tau[1 - \tau])^3$. So the quantity $\sqrt[3]{R_{3e}}/G$ should decline linearly with the conductance, $\sqrt[3]{R}/G \propto 1 - \tau$.

Figure 5.7 shows photon emission rates R , scaled as $\sqrt[3]{R}/G$, vs. the conductance G . The data were recorded with the PMT setup and the detection

⁴Unfortunately that device broke down shortly after the recording of the data of Fig. 5.6, so no additional information on the detector could be obtained.

⁵A detailed discussion of the effects of an energy dependent transmission is done in section 4.6. All relevant features are already reproduced by the energy independent approximation, which is therefore used here for simplicity.

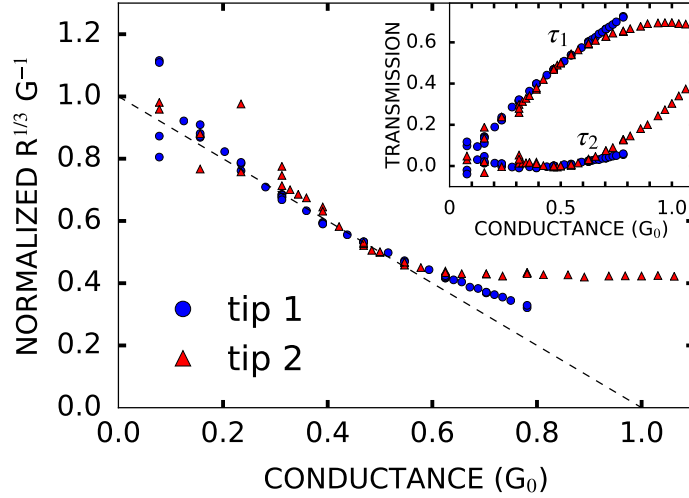


Figure 5.7: Photon emission rates R , scaled as $\sqrt[3]{R}/G$, vs. the conductance G . The measurements were done with the PMT setup and the detection range limited to photon energies of 1.77 - 3.10 eV using an optical filter. The bias was $U = 0.827$ V, so only 3e photons were detected. Two different tips were used, as indicated by the different symbols. The curves were individually normalized, i.e. multiplied with a constant factor, so they tend to 1 for vanishing conductance. The dashed straight line in is the expected behavior, if only a single conduction channel contributes. The inset shows extracted transmission values, assuming no more than two channels contribute. [32]

range limited to photon energies of 1.77 - 3.10 eV using an optical filter.⁶ The bias was $U = 0.827$ V, so only 3e photons were detected. Two different tips were used, as indicated by the different symbols. The curves were individually normalized, i.e. multiplied with a constant factor, so they tend to 1 for vanishing conductance. Note that this is not the normalization described in section 4.3, which is able to remove the influence of the plasmon function and the energy dependent sensitivity of the detection setup. That is not possible here, since only the total count rate in the sensitive range (1.77-3.10 eV) is known. Spectrally resolved information, as it is necessary for the normalization described in section 4.3, is not available with the PMT setup. The dashed straight line in Fig. 5.7 is the expected behavior, if only a single conduction channel contributes, $\sqrt[3]{R}/G \propto 1 - \tau$. For conductances up to $G = 0.5 G_0$ this is in good agreement with the data. This range and the linear fit were used for determining the normalization constant mentioned earlier. For higher conductances the photon emission rate is higher than expected for a single

⁶See section 3.5 for details.

channel. Assuming that two channels contribute significantly instead of just one and that the effect of the distance dependence of the plasmon function can be neglected, the transmission of the individual channels can be extracted directly, as it is

$$G = G_0[\tau_1 + \tau_2] \quad (5.5)$$

$$\sqrt[3]{R_{3e}}/G \propto 1 - \frac{\tau_1^2 + \tau_2^2}{\tau_1 + \tau_2}. \quad (5.6)$$

Apart from the normalization of the photon emission rate, the extraction of the transmission values has no free fit parameters. The resulting transmission values are shown in the inset of Fig. 5.7. For both tips only the first conduction channel contributes for conductances up to $0.5 G_0$. At higher conductances the second channel contributes and both channels are partially open. This is very similar to the observed behavior in the 1e energy range, where the behavior for conductances approaching G_0 cannot be explained by a single conduction channel and at least two partially open channels are necessary.⁷ The onset of the contribution of a second conduction channel at conductance far below $G = 1 G_0$ was also observed in noise measurements on Ag and Au break junctions [80].

5.4 Discussion

The multi-electron model (Eqs. 5.1-5.4) is an intentionally simple set of equations reproducing the outlined observations. It is broadly accepted that, apart from effects of non-zero temperature, interaction of at least n electrons is necessary to yield a photon with energy $h\nu = neU$ [97–99]. So the just presented results are indeed direct observations of electron-electron interaction. The presence of tip-induced plasmons plays a crucial role in the interaction. How the interaction takes place in detail is still subject of an ongoing discussion. Kaasbjerg and Nitzan [99] describe the relevant mechanism for 2e emission as a “scattering process, where an initial emission process exciting the plasmon [...] is followed by an absorption process generating a ‘hot electron’ which can emit at above-threshold energies $eV < \omega < 2eV$ ”⁸. Xu et al. [97, 98] state that “it is

⁷See section 4.4 for details.

⁸The cited source uses the symbol V for the bias, usually indicated as U in this work.

essential that the coupled electron-SPP system is treated as a quantum coherent entity since intermediate virtual states are involved". Their description of the process suggests that no re-absorption occurs between the two tunneling events and only the plasmon states matter in the intermediate steps. In both cases intermediate states are involved that should have a density of states that occurs in the complete expression for the multi-electron photon rate. In the results shown in this work, good quantitative agreement was achieved without considering any density of states, be it electronic or plasmonic, at the intermediate energies. Xu et al. [97, 98] provide an algebraic expression, so a direct comparison is possible. Eq. 8 of Ref. [97], describes the non-Gaussian rate and thus the emission at photon energies $h\nu > eU$. Its first term is equivalent to the 2e rate of Eq. 5.3, if the plasmon function can be approximated to be constant for the intermediate energies (see appendix C for details). As is shown in section 4.2, this might indeed be a good approximation for observed plasmon functions at energies far below the resonance, i.e. the maximum of the resonance function. At the experimental conditions found throughout this work only those intermediate energies play a significant role. This can be seen as consistence between the results of Xu et al. [97, 98] and the model proposed in this work, if the additional terms in Eq. 8 of Ref. [97] only represent a negligible correction to the overall expression and the first term describes the major behavior. Kaasbjerg and Nitzan [99] focus mainly on the dependence of the overall light intensity on the conductance and do not provide an algebraic expression for the spectrum. A quantitative comparison is thus impossible. The first step of the process they describe is a plasmon excitation to an intermediate energy. So the plasmon function at this intermediate energy should have to be evaluated. Since they clearly state that hot electrons play an important role in their model, the density of states of the electrons should also contribute. If this is the case, it offers a way to determine whether hot electrons are involved in intermediate steps of the multi-electron processes or not by analyzing photon emission of a system with a strongly varying electron density of states. In the results shown in this work the electron density of states could always be considered approximately constant, so no clear decision between the different processes can be made at the present time.

Concerning the conductance dependence of the light intensity, the model of Kaasbjerg and Nitzan [99] and the one presented in this work are in complete agreement: $\propto \tau[1 - \tau]$ for the 1e intensity, $\propto \tau^2[1 - \tau]^2$ for 2e processes, with

$\tau = G/G_0$, as long as a single conduction channel is sufficient to describe the contact. In the conductance range Xu et al. [97, 98] limit their model to ($G \ll G_0 \implies \tau \ll 1$), their result is also equivalent: $\propto \tau$ for the 1e intensity, $\propto \tau^2$ for the 2e intensity.

Chapter 6

Conclusion and Outlook

Light emission from the scanning tunneling microscope, resulting from single-electron as well as from multi-electron processes, was studied. The main results of this thesis are the introduction of a normalization procedure, allowing interpretation of light spectra independently of the plasmon function; extraction of temperature information from light spectra; spectrally resolved and conductance dependent measurements of light from three-electron processes; and the derivation of a semi-empirical model which quantitatively describes the light intensity of single- and multi-electron processes.

The 1e model described in section 4.1 was derived from first-order perturbation theory by applying Fermi's Golden Rule to the electron states near the tunneling junction. Even with all the simplifications that were then applied to the model to focus on the most important aspects of it, its results can still be interpreted as the inelastic one-electron transitions that are induced by the interaction of the electrons with the electromagnetic environment, namely the plasmons in the tip-sample system. The model was derived from a widely accepted theoretical concept (first-order perturbation theory) and then simplified to improve its applicability.

The multi-electron model in chapter 5 is not the result of higher-order perturbation theory, but an educated guess of how such a result might look like. Nevertheless it is in very good quantitative agreement with experimental observation and yet, given the complexity of the involved interaction, a relatively simple set of equations. As such it is useful right away, as it allows to compare otherwise very complex results (eg. light spectra rich in structure) in terms of a few very simple numerical values (eg. the constants expressing the efficiency of 2e and 3e processes a , b in Eqs. 5.1-5.4). Another application was to provide

a quantitative description of the “background” in the temperature extraction procedure of section 4.5. Beyond all this the just presented multi-electron model gives a clear preview of the results of any theoretically strict approach to the problem and can thus serve as a signpost to point in the right direction. While it most certainly misses some terms that occur in a strict analysis, it clearly covers the essential ones, which is indicated by the good agreement with observed behavior and the overall compatibility with existing theoretical works.

One important difference between the multi-electron model of this thesis and the variants of Kaasbjerg and Nitzan [99], as well as Xu et al. [97, 98], is the (non-)consideration of intermediate states. The Ag-Ag(111) junctions studied here do not allow a clear conclusion about this, since the electron density of states and the plasmon functions of these junctions do not show significant features in the energy range of the intermediate state. To decide whether plasmon modes matter for intermediate states, it would be necessary to record multi-electron light emission at photon energies far beyond the maximum of the plasmon function. With Ag this is difficult, because of the strong absorption at high photon energies due to interband transitions. It might be possible, though, using tips intentionally prepared to have a suitable plasmon resonance or by using other metallic systems. The relevance of electron states as intermediate states might be tested by analyzing light emission from structures with a strongly peaked density of states, like atomic chains or islands.

The temperature determination of section 4.5 is the latest contribution to a debate going on for a long time, which could now, hopefully, be brought to an end. Using the normalization procedure and the multi-electron model derived in this thesis, it was shown that the light intensity at photon energies exceeding the threshold $h\nu = eU$ is not exclusively due to the elevated temperature of the electron gas. This was the basic assumption in the publications that claimed electron temperatures of thousands of K. Instead, the temperature of the electrons is raised only slightly under the influence of the tunneling current and the light intensity at elevated photon energies can be understood as the result of multi-electron processes.

Appendix A

General Noise Power of Current Fluctuations

According to Blanter and Büttiker, Eq. 61 on page 26 of [100], the “general result for the noise power of the current fluctuations in a two-terminal conductor” considering Fermions is

$$S = \frac{e^2}{\pi\hbar} \sum_n \int dE \{T_n(E) [f_L(1 - f_L) + f_R(1 - f_R)] + T_n(E) [1 - T_n(E)] (f_L - f_R)^2\} \quad (\text{A.1})$$

with the transmission of the n-th conduction channel T_n and the Fermi function of the left (right) electrode f_L (f_R). A detailed interpretation of this result is done by Gavish [24]. Equation A.1 can be rearranged to match the shape of Eq. 4.22:

$$T [f_L[1 - f_L] + f_R[1 - f_R]] + T [1 - T] [f_L - f_R]^2 \quad (\text{A.2})$$

$$= T f_L - T f_L^2 + T f_R - T f_R^2 + (T - T^2)(f_L^2 - 2f_L f_R + f_R^2) \quad (\text{A.3})$$

$$= T f_L - T f_L^2 + T f_R - T f_R^2 + T f_L^2 - 2T f_L f_R + T f_R^2 - T^2 f_L^2 + 2T^2 f_L f_R - T^2 f_R^2 \quad (\text{A.4})$$

$$= T f_L + T f_R - 2T f_L f_R - T^2 f_L^2 + 2T^2 f_L f_R - T^2 f_R^2 \quad (\text{A.5})$$

$$= T f_L + T f_R - 2T f_L f_R - T^2 f_L^2 + 2T^2 f_L f_R - T^2 f_R^2 + T^2 f_L - T^2 f_L + T^2 f_R - T^2 f_R \quad (\text{A.6})$$

$$\begin{aligned}
&= T f_L + T f_R - 2T f_L f_R - T^2 f_L - T^2 f_R + 2T^2 f_L f_R \\
&\quad + T^2 f_L + T^2 f_R - T^2 f_L^2 - T^2 f_R^2 \tag{A.7}
\end{aligned}$$

$$= [T - T^2][f_L - f_L f_R + f_R + f_L f_R] + T^2[f_L - f_L^2 + f_R - f_R^2] \tag{A.8}$$

$$= T[1 - T][f_L[1 - f_R] + f_R[1 - f_L]] + T^2[f_L[1 - f_L] + f_R[1 - f_R]] \tag{A.9}$$

Note that the temperature is not stated explicitly here, but it enters the expression through the finite temperature Fermi function f . T is the channel transmission.

Equation 4.12 gives the excitation function at zero temperature. Considering the channel transmission τ explicitly, instead of implicitly as part of the constant, this can be rewritten as

$$\tilde{g}_V(h\nu) = d \int \tau(1 - \tau) f_i(\varepsilon) [1 - f_f(\varepsilon - h\nu)] d\varepsilon. \tag{A.10}$$

f_i (f_f) is the Fermi function in the initial (final) electrode of the transition. The electrodes are biased by V . In the zero temperature case only one direction is possible, there is a well defined initial and final side of the transitions.

In analogy to the general result for the current noise, I assume that the general excitation function for single electron processes and a single conduction channels is

$$\begin{aligned}
\tilde{g}(h\nu) = d \int_0^\infty d\varepsilon \left[\tau(1 - \tau) \sum_{\alpha \neq \beta} f_\alpha(\varepsilon) (1 - f_\beta(\varepsilon - h\nu)) \right. \\
\left. + \tau^2 \sum_\alpha f_\alpha(\varepsilon) (1 - f_\alpha(\varepsilon - h\nu)) \right] \tag{A.11}
\end{aligned}$$

which reduces to Eq. A.10 if the temperature is zero.

Appendix B

Non-Equilibrium Hot Carriers

Schneider et al. [61] explain the emission of photon with energies $h\nu > eU$ by a non-equilibrium electron distribution. They derive this distribution from a model of hot-hole-hot-electron cascades with the rate of the energy transfer processes from hot carriers to electrons in the Fermi sea set by phase-space consideration and at the same time all of the hot holes and electrons allowed to diffuse in the electrodes. The resulting situation is shown schematically in the left panel of Fig. B.1. The majority of the electrons is following a cold Fermi distribution, while a small fraction ($< 10^{-3}$ near the Fermi energy) of the electrons and hole is significantly hot. The occupation number of the hot electrons is well approximated to roll-off exponentially like $\exp((E - E_F)/k_B\theta)$, where an equivalent temperature θ describes the slope. In this situation one can identify 3 different types of inelastic transitions: 1.) cold electron to cold hole; 2.) hot electron to cold hole or cold electron to hot hole; 3.) hot electron to hot hole. The right panel of Fig. B.1 shows the resulting light spectrum of such a non-equilibrium distribution, calculated from Eq. 4.4, assuming constant $T(\varepsilon) = \rho_i(\varepsilon) = \rho_f(\varepsilon) = Pl(\varepsilon) = 1$, bias $U = 1 V$, temperature $\theta = 2500 K$, and normalizing the resulting spectrum so that the intensity is unity for vanishing photon energy. The respective components are indicated by colors. Type 1 transitions are responsible for the light emission at energies $h\nu \leq eU$, which is the expected result for a cold Fermi distribution. Type 2 transitions only add a negligible contribution at energies $h\nu < eU$, but lead to emission at higher energies. The intensity of type 3 transitions is negligible at all photon energies. Consequentially, the spectrum changes significantly only for photon energies $h\nu > eU$, when changing the temperature of the small fraction of hot carriers. This is illustrated in Fig. B.2, which shows (in the left panel) the resulting light

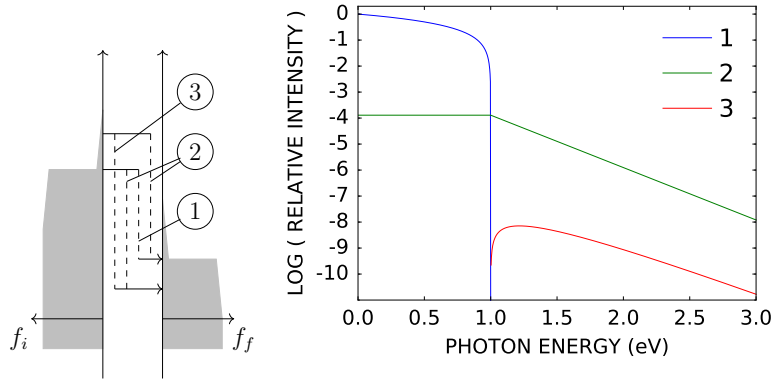


Figure B.1: (left panel) Schematic representation of the non-equilibrium occupation numbers and the different types of transition from Ref. [61]. f_i (f_f) is the occupation number in the initial (final) electrode. The number of hot electrons and holes is vastly exaggerated to enhance visibility. The possible transition types are: 1.) cold electron to cold hole; 2.) hot electron to cold hole or cold electron to hot hole; 3.) hot electron to hot hole. (right panel) The corresponding components of the light spectrum, calculated from Eq. 4.4, assuming constant $T(\varepsilon) = \rho_i(\varepsilon) = \rho_f(\varepsilon) = Pl(\varepsilon) = 1$, bias $U = 1 V$, temperature $\theta = 2500 K$, and normalizing the resulting spectrum so that the intensity is unity for vanishing photon energy.

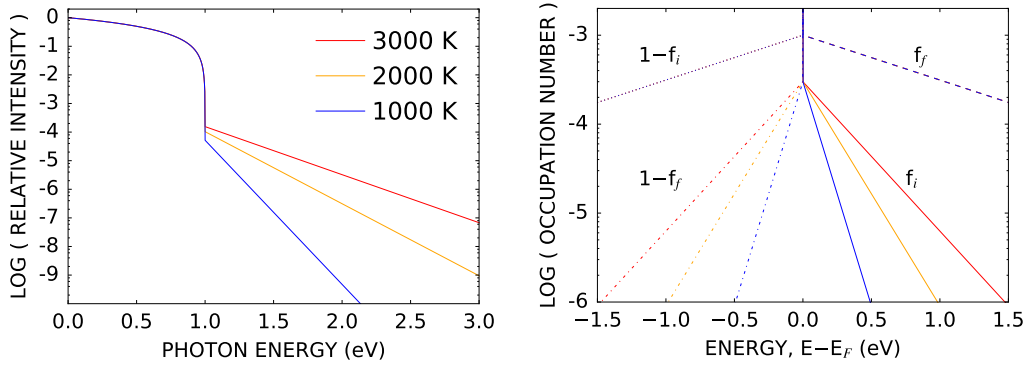


Figure B.2: (left panel) Resulting light spectra for non-equilibrium occupation numbers as described in Ref. [61], calculated from Eq. 4.4, assuming constant $T(\varepsilon) = \rho_i(\varepsilon) = \rho_f(\varepsilon) = Pl(\varepsilon) = 1$, and bias $U = 1 V$. The indicated temperatures θ describe the exponential roll-off of the hot fractions, as $\exp((E - E_F)/k_B\theta)$. All spectra were divided by a constant, so that the 3000 K spectra is unity for vanishing photon energy. (right panel) The occupation numbers used in the calculation of the spectra shown in the left panel.

spectra, calculated from Eq. 4.4, assuming constant $T(\varepsilon) = \rho_i(\varepsilon) = \rho_f(\varepsilon) = Pl(\varepsilon) = 1$, bias $U = 1V$, and 3 different temperatures θ . All three spectra were divided by the same constant, chosen so that the 3000 K spectrum is unity for vanishing photon energies. The right panel of Fig. B.2 shows the occupation numbers used to calculate the spectra. The temperatures for this example were chosen arbitrarily. The relative number of hot carrier is the same as in Ref. [61]. The light spectra calculated in this manner always exhibit a sharp kink at photon energy $h\nu = eU$, independent of the temperature chosen or the exact fraction of hot carriers. This is a direct consequence of the fact that the vast majority of the carriers is cold and the dominating process for photon emission thus linearly drops to zero at that photon energy. Measured spectra exhibit a smooth transition at photon energy $h\nu = eU$ instead of a sharp kink, as is analyzed in detail in section 4.5. This observation does not rule out the presence of a tiny fraction of very hot carriers in the actual electron distribution. A partial thermalization would be enough to explain the observed temperature effect analyzed in section 4.5.

Appendix C

Comparison with Xu et al.

Xu et al. [97] proposed a model of the overbias light emission in analogy of the dynamical Coulomb blockade. Their result has similarities with the model shown in this work (Eqs. 5.1-5.4). This will be briefly shown in the following. For simplicity only the zero temperature results of Ref. [97] will be covered here. A finite temperature expansion of the model has also been published [98].

Equation 5 of Ref. [97] reads¹

$$\Gamma_G(\epsilon) = \tilde{\alpha}^2 \frac{|\tilde{z}_\epsilon|^2}{\epsilon^2} \left[g_c Y(|\epsilon| - eU) + \text{Re}\left(\frac{2}{\tilde{z}_\epsilon}\right) Y(-\epsilon) \right] \quad (\text{C.1})$$

with $Y(x) = -x\theta(-x)$ with the Heaviside θ function. g_c is the conductance G of the junction in units of the conductance quantum $G_0 = 2e/h$: $g_c = G/G_0$. \tilde{z}_ω is the effective impedance of the RLC circuit they use to model the electromagnetic environment of the tip-sample junction. $\frac{|\tilde{z}_\epsilon|^2}{\epsilon^2}$ is the resonance function of this circuit. $\tilde{\alpha}$ expresses the coupling strength between the current and the electromagnetic environment. Equation C.1 describes photon emission and absorption, where $\epsilon < 0$ corresponds to emission. The model is limited to small conductances $G \ll G_0$.

The zero temperature result of the 1e-model for constant electron density of states is

$$R_{1e}(h\nu) = \frac{2\pi}{\hbar} Pl(h\nu)\tau[1 - \tau][eU - h\nu]\theta(eU - h\nu) \quad (\text{C.2})$$

with $\tau = G/G_0$. Except for constant factors this is identical to the first terms

¹To avoid confusion the bias is indicated as U here, even though the original source used V .

of Eq. C.1 in the limit $G \ll G_0$ and thus $\tau[1 - \tau] \approx \tau$, if one identifies the RLC resonance function as the plasmon function: $\frac{|\tilde{z}_\epsilon|^2}{\epsilon^2} = Pl(\epsilon)$.

The 2e part of the multi-electron model of this work for zero temperature is

$$R_{2e}(h\nu) = \frac{2\pi}{\hbar} Pl(h\nu) a \tau^2 [1 - \tau]^2 \int_0^{h\nu} d\varepsilon [eU - \varepsilon] \theta(eU - \varepsilon) [eU - h\nu + \varepsilon] \theta(eU - h\nu + \varepsilon). \quad (\text{C.3})$$

The integral is over all possible intermediate energies ε .

Equation 8 of Ref. [97], describing the emission due to non-Gaussian noise and thus overbias emission, is

$$\Gamma_{nG}(\epsilon < 0) = \frac{\tilde{\alpha}^2}{8} g_c^2 \frac{|\tilde{z}_\epsilon|^2}{\epsilon^2} \left\{ \int_0^{eV} d\omega \frac{|\tilde{z}_\omega|^2}{\omega^2} (eU - \omega) \times [\xi(\omega + \epsilon) + \xi(\omega - \epsilon) + 2\epsilon - \xi(\epsilon)] + \dots \right\} \quad (\text{C.4})$$

with $\xi(\omega) = |\omega + eU| + |\omega - eU|$, also integrating over all possible intermediate energies ω . For $h\nu = -\epsilon > eU$ it is

$$\xi(\omega + \epsilon) + \xi(\omega - \epsilon) + 2\epsilon - \xi(\epsilon) \quad (\text{C.5})$$

$$= |\omega + \epsilon + eU| + |\omega + \epsilon - eU| + |\omega - \epsilon + eU| + |\omega - \epsilon - eU| + 2\epsilon - |\epsilon + eU| - |\epsilon - eU| \quad (\text{C.6})$$

$$= \omega + \epsilon + eU - \omega - \epsilon + eU + \omega - \epsilon + eU + \omega - \epsilon - eU + 2\epsilon + \epsilon - eU + \epsilon + eU \quad (\text{C.7})$$

$$= 2[eU + \omega + \epsilon]. \quad (\text{C.8})$$

Equation C.3 and the first term of Eq. C.4 are similar, but there seem to be differences: Equation C.3 does not include the plasmon function at intermediate energies and the integration limits are different. However, the resonance function used by Xu et al. is approximately constant at energies far below the resonance, which are the energies most important for the intermediate steps. The integration limits of Eq. C.3 arise from the fact that there is no consideration of absorption in the model, so if the resulting photon is at energy $h\nu$ the intermediate energy must be less than that. At the same time the first Heaviside θ function assures the intermediate energy is less than eU . For the photon energy range where the 2e process is the dominating one, $eU < h\nu < 2eU$, the

effective upper limit for the integral is thus eU . This limit, which is directly used in the integral in Eq. C.4, is a consequence of the zero temperature. A single electron cannot provide more than the energy eU and thus the intermediate energy is limited.

Appendix D

Energy Dependent Transmission

In section 4.6 the effects of the energy dependence of the transmission T on the normalized spectral intensity as well as on the conductance dependent total intensity and total yield were analyzed. Unlike in the elastic case, where only a single electron energy is considered, there are two involved electron energies in the inelastic case: before and after the transition. In the analysis of shot noise this problem is usually circumvented by taking into account the fact that measurements are done under very small bias. Initial and final energy differ thus only very little and the transmission can be assumed to be energy independent. The bias used for light emission experiments is not small, so this argument does not hold. It is therefore not obvious at which energy T has to be evaluated or even if the two occurrences have to be evaluated at the same energy. Fortunately, the result of the analysis of section 4.6 is qualitatively the same for all four possible combinations: the influence on the normalized spectral intensity is negligibly small, the intensity as a function of conductance is skewed towards small conductance values. This is shown in Figs. D.1-D.4, where the left panel is calculated identical to Fig. 4.13b and the right panel identical to Fig. 4.16a, but each one with the indicated evaluation of T .

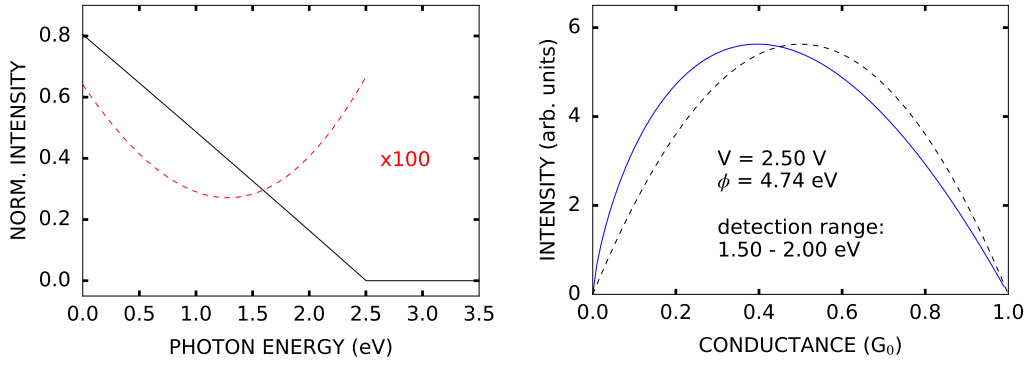


Figure D.1: Results of $R(h\nu) \propto \int_0^{eV} d\varepsilon T(\varepsilon) [1 - T(\varepsilon)]$.

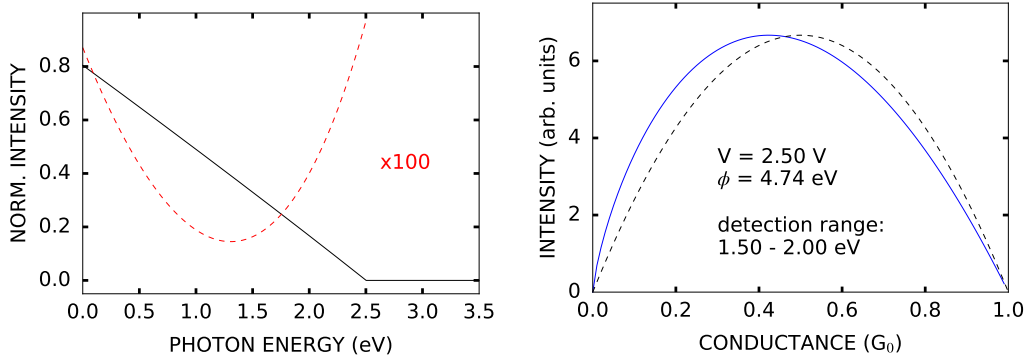


Figure D.2: Results of $R(h\nu) \propto \int_0^{eV} d\varepsilon T(\varepsilon) [1 - T(\varepsilon - h\nu)]$.

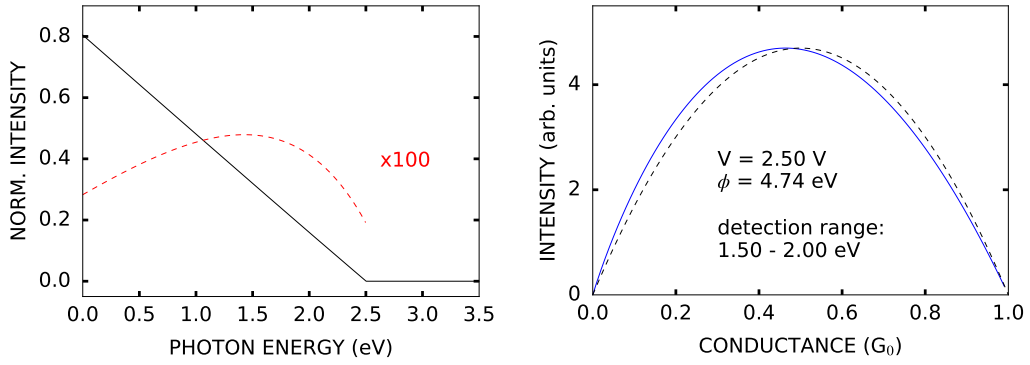


Figure D.3: Results of $R(h\nu) \propto \int_0^{eV} d\varepsilon T(\varepsilon - h\nu) [1 - T(\varepsilon)]$.

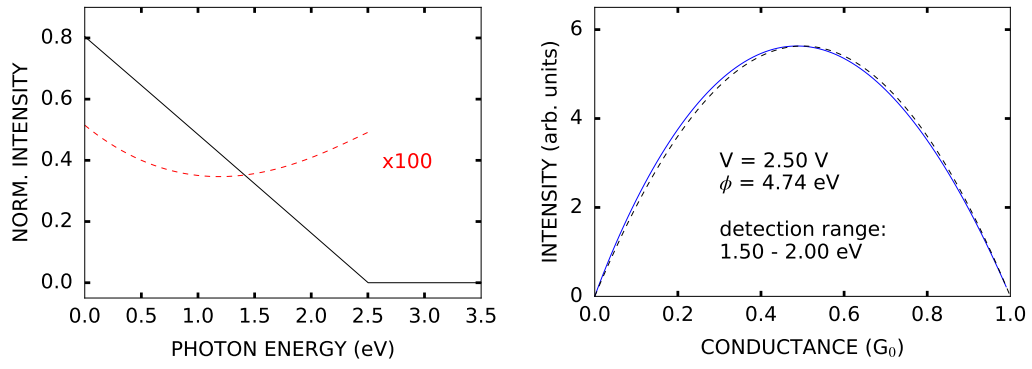


Figure D.4: Results of $R(h\nu) \propto \int_0^{eV} d\varepsilon T(\varepsilon - h\nu) [1 - T(\varepsilon - h\nu)]$.

Appendix E

Acknowledgements

The present thesis is my own work, but would have never been possible without the help of many others to whom I would like to express my gratitude:

The work that led to this thesis was conducted under the supervision of Richard Berndt, who in spite of many responsibilities always found the time for discussion and always had an open door. While granting me a lot of freedom to pursue my own ideas, he always assured I don't wander off too much. Leading by example and through constructive criticism of my work he taught me a great deal on scientific work, scientific writing and giving talks, which I deeply appreciate.

I am indebted to Manuel Gruber, who not only read the manuscript of this thesis and pointed out many possibilities for improvement, but also offered support and good advice in many situations. More than once, his positive and constructive attitude provided the necessary nudge for me to carry on.

Svenja Mühlenberend and Natalia Schneider introduced me to the 5K-lab and the measurement techniques established at the time I joined the team. I hope I could honor Svenja's commitment to the lab by the improvements I came up with.

Exceptionally good technical support was assured by Rene Woltmann, Jörg Neubauer and Joost Jakobs. Especially Rene, who many times fixed hardware problems and fabricated complicated but necessary spare parts in an instant, contributed critically to the smooth operation of the lab.

I also thank Alexander Weismann and Jan-Dirk Matthießen for reading and commenting on parts of the manuscript.

I would further like to thank all members of the workgroup, who were part of a great and supportive working environment. Innumerable discussions in the coffee room had their share in the creation of this thesis.

Many discussions with Kristen Kaasbjerg and Wolfgang Belzig, with additional input from Fei Xu and Gianluca Rastelli, helped to advance my understanding of multi-electron processes. Our long lasting dissent on the details of a quantitative description of those processes strongly influenced the final results presented in chapter 5 and finally lead to a successfully published article [32]. Thanks to all of them for the at times exhausting, but in the end valuable, collaboration.

I also thank Mads Brandbyge for kindly answering my questions on quantum noise. I enjoyed many discussion with Andreas Burtzloff on that topic as well.

Finally, I thank my girlfriend Silvia for her continuous support through all the years.

Appendix F

Data Used

Figure	Used Data Sets	Integration Time
3.1	16F01_128	10x60s
	16F01_130	15x60s
3.2	16E29_015	10x0.1s
	16E29_016	5x60s
	16E29_003	15x60s
3.3	16E29_008	10x0.1s
	16E29_009	10x0.1s
	16E29_010	10x0.1s
	16E29_012	10x0.1s
	...	10x0.1s
	16E29_015	10x0.1s
4.1	15D11_041	10x0.1s
	15D11_042	10x0.1s
	15D12_021	10x0.1s
	15D12_028	10x0.1s
	15D15_001	10x0.1s
	15D15_007	10x0.1s
	15F16_020	600x0.2s
	15F16_021	600x0.2s
4.2	15D11_003	5x0.1s
	15D11_004	5x0.1s
	15D11_007	10x0.1s
	15D11_008	10x0.1s
	15D11_011	10x0.1s

Figure	Used Data Sets	Integration Time
4.2 (cont.)	15D11_017	10x0.1s
	15D11_027	10x0.1s
	15D11_037	10x0.1s
	15D11_039	10x0.1s
	...	10x0.1s
	15D11_042	10x0.1s
	15D12_001	10x0.1s
	15D12_002	10x0.1s
	15D12_008	10x0.1s
	15D12_010	10x0.1s
	15D12_014	10x0.1s
	15D12_020	10x0.1s
	15D12_021	10x0.1s
	15D12_028	10x0.1s
	15D12_036	10x0.1s
	15D12_037	10x0.1s
	15D13_001	10x0.1s
	15D13_002	10x0.1s
	15D13_012	10x0.1s
	15D13_013	10x0.1s
	15D14_001	10x0.1s
	15D14_002	10x0.1s
	15D14_041	10x0.1s
	15D15_001	10x0.1s
	15D15_003	10x0.1s
	15D15_007	10x0.1s
	15D15_024	10x0.1s
	15D15_025	10x0.1s
	15D15_043	10x0.1s
	15D15_051	10x0.1s
	15F13_001	10x1s
	15F13_004	10x1s
	15F13_006	30x0.2s
	15F13_009	30x0.2s
	15F13_011	30x0.2s

Figure	Used Data Sets	Integration Time
4.2 (cont.)	15F13_012	30x0.2s
	15F13_014	10x1s
	15F13_020	30x0.2s
	15F13_025	30x0.2s
	15F13_028	30x0.2s
	15F14_001	300x0.2s
	15F14_006	10x0.2s
	15F15_003	1200x0.2s
	15F15_004	1200x0.2s
	15F15_009	50x0.2s
	15F15_012	50x0.2s
	15F16_016	50x0.2s
	15F16_017	50x0.2s
	15F16_018	50x0.2s
	15F16_019	50x0.2s
	15F16_020	600x0.2s
	15F16_021	600x0.2s
	15F16_024	50x0.2s
	15F16_025	50x0.2s
	15F17_004	600x0.2s
	15F17_005	600x0.2s
	15F17_016	50x0.2s
	15F17_017	50x0.2s
	15F17_026	600x0.2s
	15F17_050	50x0.2s
	...	50x0.2s
	15F17_053	50x0.2s
	15F17_054	50x0.1s
	15F17_055	50x0.1s
	15F17_080	50x0.2s
	15F17_081	50x0.2s
	15F17_093	50x0.5s
	15F17_094	50x0.5s
	15F20_005	60x0.5s
	15F20_006	60x0.5s

Figure	Used Data Sets	Integration Time
4.2 (cont.)	15F20_017	20x0.5s
	15F20_018	20x0.5s
4.3	15D11_027	10x0.1s
	15D11_037	10x0.1s
	15D12_001	10x0.1s
	15D12_002	10x0.1s
	15D13_001	10x0.1s
	15D13_002	10x0.1s
	15F17_080	50x0.2s
	15F17_081	50x0.2s
4.4	15F20_018	20x0.5s
	15F20_019	20x0.5s
	15F20_001 (IR)	4x15s
	15F20_002 (IR)	4x15s
	15F20_003 (IR)	4x15s
	15F20_004 (IR)	4x15s
4.5	none	
4.6a	15F12_001 (IR)	(10+2)x20s
	15F12_002 (IR)	(10+2)x20s
4.6b	16G31_047	50x0.2s
	16G31_048	50x0.2s
	16G31_055	50x0.2s
	...	50x0.2s
	16G31_063	50x0.2s
4.7	16F01_132	120x1s
	16F01_137	20x1s
4.8,4.9	none	
4.10a	15F17_072	100x0.1s
	15F17_073	100x0.1s
	15F17_074	50x0.2s
	15F17_075	50x0.2s
4.10b	16F01_135	120x1s
	16F01_137	20x1s
	...	20x1s
	16F01_142	20x1s

Figure	Used Data Sets	Integration Time
4.11	15F17_004	600x0,2s
	15F17_005	600x0,2s
	15F17_006	24x5s
	15F17_007	24x5s
	15F17_008	50x0.2s
	15F17_009	50x0.2s
	15F17_010	600x0.2s
	15F17_011	600x0.2s
	15F17_026	600x0.2s
	15F17_027	600x0.2s
	15F17_028	24x5s
	15F17_029	24x5s
	15F17_030	50x0.2s
	...	50x0.2s
	15F17_033	50x0.2s
	15F17_054	50x0.1s
	15F17_055	50x0.1s
	15F17_056	12x5s
	15F17_057	12x5s
	15F17_058	100x0.1s
	15F17_059	100x0.1s
	15F17_060	50x0.2s
	15F17_061	50x0.2s
	15F17_068	100x0.1s
	15F17_069	100x0.1s
	15F17_070	12x5s
	15F17_071	12x5s
	15F17_072	100x0.1s
15F17_073	100x0.1s	
15F17_074	50x0.2s	
15F17_075	50x0.2s	
4.12	14C20_004 (IR)	10x1x1s
	...	10x1x1s
	14C20_008 (IR)	10x1x1s
4.13-4.16	none	

Figure	Used Data Sets	Integration Time
5.1	16F01_128 16F01_129 16F01_130 16F01_131 16F01_132 16F01_135	10x60s 30x60s 15x60s 15x60s 120x1s 120x1s
5.2	15F17_072 15F17_073 15F17_074 15F17_075	100x0.1s 100x0.1s 50x0.2s 50x0.2s
5.3	counts_15D11_1 counts_15D11_3 counts_15D14_041_2 counts_15D15_2	10s per point 10s per point 10s - 60s per point 15s - 60s per point
5.4	none	
5.5a	15F17_072 15F17_073 15F17_074 15F17_075	100x0.1s 100x0.1s 50x0.2s 50x0.2s
5.5b	16F01_128 16F01_129 16F01_130 16F01_131 16F01_132 16F01_135	10x60s 30x60s 15x60s 15x60s 120x1s 120x1s
5.6	4J13_2 4J13_dark_shutter_open_2 4J13_3 4J13_dark_shutter_open_3 4J13_4	240x0.1s 240x0.1s 240x60s 10x60s 10x0.1s
5.7	counts_15D11_1 counts_15D11_3 counts_15D14_041_2 counts_15D15_2	10s per point 10s per point 10s - 60s per point 15s - 60s per point
B.1,B.2	none	

Bibliography

- [1] S. Wedge, J. a. E. Wasey, W. L. Barnes, and I. Sage, *Applied Physics Letters* **85**, 182 (2004).
- [2] C. Liu, V. Kamaev, and Z. V. Vardeny, *Applied Physics Letters* **86**, 143501 (2005).
- [3] E. Ozbay, *Science* **311**, 189 (2006).
- [4] S. Pillai, K. R. Catchpole, T. Trupke, G. Zhang, J. Zhao, and M. A. Green, *Applied Physics Letters* **88**, 161102 (2006).
- [5] S. Pillai, K. R. Catchpole, T. Trupke, and M. A. Green, *Journal of Applied Physics* **101**, 093105 (2007).
- [6] M. Kirkengen, J. Bergli, and Y. M. Galperin, *Journal of Applied Physics* **102**, 093713 (2007).
- [7] D. Derkacs, W. V. Chen, P. M. Matheu, S. H. Lim, P. K. L. Yu, and E. T. Yu, *Applied Physics Letters* **93**, 091107 (2008).
- [8] A. J. Morfa, K. L. Rowlen, T. H. Reilly, M. J. Romero, and J. van de Lagemaat, *Applied Physics Letters* **92**, 013504 (2008).
- [9] C. Hägglund, *Nanoparticle plasmon influence on the charge carrier generation in solar cells* (Institutionen för teknisk fysik, Kemisk fysik, Chalmers tekniska högskola,, 2008).
- [10] D. J. Bergman and M. I. Stockman, *Physical Review Letters* **90**, 027402 (2003).
- [11] M. A. Noginov, G. Zhu, A. M. Belgrave, R. Bakker, V. M. Shalaev, E. E. Narimanov, S. Stout, E. Herz, T. Suteewong, and U. Wiesner, *Nature* **460**, 1110 (2009).

- [12] R. F. Oulton, V. J. Sorger, T. Zentgraf, R.-M. Ma, C. Gladden, L. Dai, G. Bartal, and X. Zhang, *Nature* **461**, 629 (2009).
- [13] R.-M. Ma, R. F. Oulton, V. J. Sorger, G. Bartal, and X. Zhang, *Nature Materials* **10**, 110 (2011).
- [14] R. Berndt, R. Gaisch, W. D. Schneider, J. K. Gimzewski, B. Reihl, R. R. Schlittler, and M. Tschudy, *Physical Review Letters* **74**, 102 (1995).
- [15] J. Lambe and S. L. McCarthy, *Physical Review Letters* **37**, 923 (1976).
- [16] R. Berndt, J. K. Gimzewski, and P. Johansson, *Physical Review Letters* **71**, 3493 (1993).
- [17] T. Atay, J.-H. Song, and A. V. Nurmikko, *Nano Letters* **4**, 1627 (2004).
- [18] K. J. Savage, M. M. Hawkeye, R. Esteban, A. G. Borisov, J. Aizpurua, and J. J. Baumberg, *Nature* **491**, 574 (2012).
- [19] D. C. Marinica, M. Zapata, P. Nordlander, A. K. Kazansky, P. M. Echenique, J. Aizpurua, and A. G. Borisov, *Science Advances* **1**, e1501095 (2015).
- [20] Y. Vardi, E. Cohen-Hoshen, G. Shalem, and I. Bar-Joseph, *Nano Letters* **16**, 748 (2016).
- [21] G. Hoffmann, J. Aizpurua, P. Apell, and R. Berndt, *Surface Science* **482–485, Part 2**, 1159 (2001).
- [22] J.-T. Lü, R. B. Christensen, and M. Brandbyge, *Physical Review B* **88**, 045413 (2013).
- [23] U. Gavish, Y. Imry, Y. Levinson, and B. Yurke, arXiv:cond-mat/0211646 (2002).
- [24] U. Gavish, *Quantum Current Noise in Mesoscopic Systems*, Ph.D. thesis (2003).
- [25] H. E. van den Brom and J. M. van Ruitenbeek, *Physical Review Letters* **82**, 1526 (1999).
- [26] M. Kumar, R. Avriller, A. L. Yeyati, and J. M. van Ruitenbeek, *Physical Review Letters* **108**, 146602 (2012).

- [27] A. Burtzloff, A. Weismann, M. Brandbyge, and R. Berndt, *Physical Review Letters* **114**, 016602 (2015).
- [28] R. J. Schoelkopf, P. J. Burke, A. A. Kozhevnikov, D. E. Prober, and M. J. Rooks, *Physical Review Letters* **78**, 3370 (1997).
- [29] R. Pechou, R. Coratger, F. Ajustron, and J. Beauvillain, *Applied Physics Letters* **72**, 671 (1998).
- [30] A. Downes, P. Dumas, and M. E. Welland, *Applied Physics Letters* **81**, 1252 (2002).
- [31] G. Hoffmann, R. Berndt, and P. Johansson, *Physical Review Letters* **90**, 046803 (2003).
- [32] P.-J. Peters, F. Xu, K. Kaasbjerg, G. Rastelli, W. Belzig, and R. Berndt, *Phys. Rev. Lett.* **119**, 066803 (2017).
- [33] G. Binnig, H. Rohrer, C. Gerber, and E. Weibel, *Applied Physics Letters* **40**, 178 (1982).
- [34] G. Binnig and H. Rohrer, *Helvetica Physica Acta* **55**, 726 (1982).
- [35] R. D. Young, *Physics Today* **24**, 42 (1971).
- [36] P. K. Hansma and H. P. Broida, *Applied Physics Letters* **32**, 545 (1978).
- [37] R. W. Rendell, D. J. Scalapino, and B. Mühlischlegel, *Physical Review Letters* **41**, 1746 (1978).
- [38] R. W. Rendell and D. J. Scalapino, *Physical Review B* **24**, 3276 (1981).
- [39] J. K. Gimzewski, B. Reihl, J. H. Coombs, and R. R. Schlittler, *Zeitschrift für Physik B Condensed Matter* **72**, 497 (1988).
- [40] J. K. Gimzewski, J. K. Sass, R. R. Schlitter, and J. Schott, *EPL (Europhysics Letters)* **8**, 435 (1989).
- [41] R. Ritchie, *Surface Science* **34**, 1 (1973).
- [42] W. L. Barnes, A. Dereux, and T. W. Ebbesen, *Nature* **424**, 824 (2003).
- [43] J. R. Sambles, G. W. Bradbery, and F. Yang, *Contemporary Physics* **32**, 173 (1991).

- [44] F. Rossel, M. Pivetta, and W.-D. Schneider, *Surface Science Reports* **65**, 129 (2010).
- [45] P. Johansson, R. Monreal, and P. Apell, *Physical Review B* **42**, 9210 (1990).
- [46] J. Aizpurua, S. P. Apell, and R. Berndt, *Physical Review B* **62**, 2065 (2000).
- [47] G. Schull, N. Néel, P. Johansson, and R. Berndt, *Physical Review Letters* **102**, 057401 (2009).
- [48] N. L. Schneider, G. Schull, and R. Berndt, *Physical Review Letters* **105**, 026601 (2010).
- [49] J. U. Kliewer, *Dynamics and Manipulation of Surface States*, Ph.D. thesis, Rheinisch–Westfälische Technische Hochschule Aachen (2000).
- [50] G. Hoffmann, J. Kröger, and R. Berndt, *Review of Scientific Instruments* **73**, 305 (2002).
- [51] G. Hoffmann, *Light Emission from Metals and Adsorbates in the Scanning Tunneling Microscope*, Ph.D. thesis, Christian-Albrechts-Universität zu Kiel (2001).
- [52] D. Bonnell, ed., *Scanning Probe Microscopy and Spectroscopy: Theory, Techniques, and Applications, 2nd Edition* (Wiley-VCH, 2001).
- [53] C. J. Chen, *Introduction to Scanning Tunneling Microscopy: Second Edition* (Oxford University Press, 2008).
- [54] A. Castellanos-Gomez, G. Rubio-Bollinger, M. Garnica, S. Barja, A. L. Vázquez de Parga, R. Miranda, and N. Agraït, *Ultramicroscopy* **122**, 1 (2012).
- [55] D. Groom, *Experimental Astronomy* **14**, 45 (2002).
- [56] A. Rest, L. Mündermann, R. Widenhorn, E. Bodegom, and T. C. McGlinn, *Review of Scientific Instruments* **73**, 2028 (2002).
- [57] HORIBA, “Symphony II Linear InGaAs Arrays,” (accessed 04-2017), http://www.horiba.com/fileadmin/uploads/Scientific/Documents/OSD/Symphony_II_IGA_512_x_1__25_x_500_-_1700_rev_C.pdf.

- [58] HORIBA, “iHR Series Spectrometers,” (2013, accessed 04-2017), http://www.horiba.com/fileadmin/uploads/Scientific/Documents/Mono/iHR_Brochure-2013.pdf.
- [59] LASERCOMPONENTS, “Fiber material factsheet,” (accessed 05-2017), http://www.lasercomponents.com/fileadmin/user_upload/home/Datasheets/polymicro/jtfih-ultra-low-oh.pdf.
- [60] B. N. J. Persson and A. Baratoff, *Physical Review Letters* **68**, 3224 (1992).
- [61] N. L. Schneider, P. Johansson, and R. Berndt, *Physical Review B* **87**, 045409 (2013).
- [62] L. Novotny and B. Hecht, *Principles of Nano-Optics* (Cambridge University Press, 2006).
- [63] C. Chen, C. A. Bobisch, and W. Ho, *Science* **325**, 981 (2009).
- [64] P. Chen, W. Wang, N. Lin, and S. Du, *Optics Express* **22**, 8234 (2014).
- [65] G. Schull, M. Becker, and R. Berndt, *Physical Review Letters* **101**, 136801 (2008).
- [66] P. Johansson, *Physical Review B* **58**, 10823 (1998).
- [67] P. Johansson and R. Monreal, *Zeitschrift für Physik B Condensed Matter* **84**, 269 (1991).
- [68] A. Madrazo, M. Nieto-Vesperinas, and N. García, *Physical Review B* **53**, 3654 (1996).
- [69] J. Aizpurua, G. Hoffmann, S. P. Apell, and R. Berndt, *Physical Review Letters* **89**, 156803 (2002).
- [70] K. Meguro, K. Sakamoto, R. Arafune, M. Satoh, and S. Ushioda, *Physical Review B* **65**, 165405 (2002).
- [71] M. G. Boyle, J. Mitra, and P. Dawson, *Applied Physics Letters* **94**, 233118 (2009).
- [72] S. Wu and D. L. Mills, *Physical Review B* **65**, 205420 (2002).

- [73] E. J. Zeman and G. C. Schatz, *The Journal of Physical Chemistry* **91**, 634 (1987).
- [74] R. Landauer, *IBM Journal of Research and Development* **1**, 223 (1957).
- [75] D. S. Fisher and P. A. Lee, *Physical Review B* **23**, 6851 (1981).
- [76] M. Büttiker, *Physical Review Letters* **57**, 1761 (1986).
- [77] R. Landauer, *IBM Journal of Research and Development* **32**, 306 (1988).
- [78] M. Büttiker, *IBM Journal of Research and Development* **32**, 317 (1988).
- [79] W. Schottky, *Annalen der Physik* **362**, 541 (1918).
- [80] R. Vardimon, M. Klionsky, and O. Tal, *Physical Review B* **88**, 161404 (2013).
- [81] H. Birk, M. J. M. de Jong, and C. Schönenberger, *Physical Review Letters* **75**, 1610 (1995).
- [82] K. S. Ralls, D. C. Ralph, and R. A. Buhrman, *Physical Review B* **40**, 11561 (1989).
- [83] P. A. M. Holweg, J. Caro, A. H. Verbruggen, and S. Radelaar, *Ballistic electron transport and two-level resistance fluctuations in noble-metal nanobridges*, Vol. 45 (1992) pp. 9311–9319.
- [84] C. J. Muller, J. M. van Ruitenbeek, and L. J. de Jongh, *Physical Review Letters* **69**, 140 (1992).
- [85] M. Henny, H. Birk, R. Huber, C. Strunk, A. Bachtold, M. Krüger, and C. Schönenberger, *Applied Physics Letters* **71**, 773 (1998).
- [86] M. Buret, A. V. Uskov, J. Dellinger, N. Cazier, M.-M. Mennemanteuil, J. Berthelot, I. V. Smetanin, I. E. Protsenko, G. Colas-des Francs, and A. Bouhelier, *Nano Letters* **15**, 5811 (2015).
- [87] A. M. Bratkovsky, A. P. Sutton, and T. N. Todorov, *Physical Review B* **52**, 5036 (1995).
- [88] J. G. Simmons, *Journal of Applied Physics* **34**, 2581 (1963).
- [89] J. G. Simmons, *Journal of Applied Physics* **34**, 1793 (1963).

- [90] R. J. Hamers and D. F. Padowitz, in *Scanning Probe Microscopy and Spectroscopy*, edited by D. Bonnell (Wiley-VCH, 2001) 2nd ed., Chap. 4, pp. 59–110.
- [91] J. Bardeen, *Physical Review Letters* **6**, 57 (1961).
- [92] J. Tersoff and D. R. Hamann, *Physical Review Letters* **50**, 1998 (1983).
- [93] J. Tersoff and D. R. Hamann, *Physical Review B* **31**, 805 (1985).
- [94] C. J. Chen, *Physical Review B* **42**, 8841 (1990).
- [95] C. J. Chen, *Physical Review Letters* **65**, 448 (1990).
- [96] J. Tobiska, J. Danon, I. Snyman, and Y. V. Nazarov, *Physical Review Letters* **96**, 096801 (2006).
- [97] F. Xu, C. Holmqvist, and W. Belzig, *Physical Review Letters* **113**, 066801 (2014).
- [98] F. Xu, C. Holmqvist, G. Rastelli, and W. Belzig, *Physical Review B* **94**, 245111 (2016).
- [99] K. Kaasbjerg and A. Nitzan, *Physical Review Letters* **114**, 126803 (2015).
- [100] Y. M. Blanter and M. Büttiker, *Physics Reports* **336**, 1 (2000), arXiv: cond-mat/9910158.